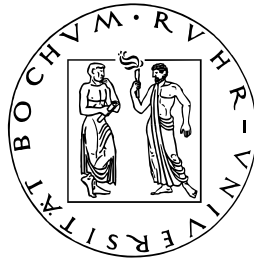


Ruhr-Universität Bochum

Institut für Geologie, Mineralogie und Geophysik



Mechanical behavior of synthetic omphacite aggregates
at high temperature and high pressure

Dissertation von

Rasoul Hamidzadeh Moghadam

vorgelegt zur Erlangung des Grades eines Doktors der Naturwissenschaften

Juli 2009

Contents

1. Introduction and scope	1
1.1. Introduction	1
1.2. Scope and approach of this study	3
2. Background	5
2.1. Eclogite classification	5
2.2. Structure and phase stability of omphacite	6
2.3. Partial melting of eclogite and omphacite	9
2.4. Crystal-plastic deformation	10
2.5. Activation energies of kinetic processes in pyroxenes	11
3. Materials and methods	14
3.1. Analytical methods	14
3.2. Starting material	15
3.2.1. Synthetic omphacite aggregates	15
3.2.1.1. Synthesis	15
3.2.1.2. Microstructure and composition of synthetic samples	17
3.2.2. Natural samples	23
3.2.3. Hydrogen content	24
3.3. Deformation experiments	26
3.3.1. Experimental procedure	26
3.3.2. Derivation of stress-strain curves	29
4. Results of deformation experiments	32
4.1. Synthetic aggregates	32
4.1.1. Mechanical data	32
4.1.2. Microstructures	37
4.2. Natural clinopyroxene samples	41
4.2.1. Mechanical data	41
4.2.2. Microstructures	43
4.3. Hydrogen content of deformed samples	45
4.4. Effect of pressure on strength	48
5. Discussion	50
5.1. Comparison to previous work	50
5.2. Mechanisms controlling deformation of omphacite	53
5.2.1. Modeling the deformation of jd-aggregates by climb-controlled creep	56
5.2.2. Glide-controlled deformation of diopside aggregates	58
5.3. Rheological scaling relations	62
5.3.1. The effect of composition on strength	62
5.3.2. The effect of hydrogen content and pressure on strength	63
5.4. Geological implications	68
6. Summary	71
References	73
Appendix A: The axial load-displacement curves for synthetic omphacite aggregates	
Appendix B: The axial load-displacement curves for natural clinopyroxenite samples	
Zusammenfassung (summary in german)	

1. Introduction and scope

1.1. Introduction

Eclogites are found as xenoliths in kimberlites and basalts, as layers and lenses in alpine-type peridotite bodies, as blocks in blueschist facies terrains and constitute large volumes of the exhumed crust in high pressure metamorphic terrains [see *Carswell*, 1990]. Recently, the term “eclogite engine” has been coined to emphasize that eclogitization is the expected universal fate of aging lithosphere and thus constitutes a key player in plate tectonics [*Anderson*, 2007]. In particular, eclogites are expected to replace basalts and gabbros of the oceanic crust during subduction of oceanic lithosphere. The kinetics of the eclogite-forming reactions suggest a transition at depths exceeding about 50 km [e.g., *Hacker*, 1996; *Kirby et al.*, 1996]. At larger depths a continuous eclogitic layer with a thickness of several kilometers is predicted at the top of the downgoing slab. The deformation characteristics of this layer are of utmost importance for the stress transfer at the plate boundary and therefore the dynamics of subduction zones.

Eclogitized oceanic crust is primarily composed of omphacite and garnet. Natural omphacite is a solid solution of the sodic endmember jadeite (jd: $\text{NaAlSi}_2\text{O}_6$) and the calcic endmember diopside (di: $\text{CaMgSi}_2\text{O}_6$), with up to 10% of acmite ($\text{NaFeSi}_2\text{O}_6$). Microstructures of eclogites presently exposed at Earth's surface reveal that omphacite controls their bulk rheological properties at natural conditions. In many cases, undeformed garnet crystals are embedded in a continuous matrix of omphacite with shape- and crystallographic-preferred orientation. In places, omphacite microstructures are indicative of recovery and recrystallization; mechanical twins and kink bands are observed [e.g., *Aoya*, 2001; *Godard and Van Roermund*, 1995; *Philippot et al.*, 1992; *Piepenbreier and Stöckhert*, 2001; *Stöckhert and Renner*, 1998; *van der Klauw et al.*, 1997; *Van Roermund and Boland*, 1981].

Crystallographic preferred orientations (CPOs) of clinopyroxenes are commonly observed in both natural and experimentally deformed samples. The L-type CPO is characterized by a point maximum of the c axes [001] parallel to the lineation while the b axes [010] form a girdle perpendicular to the lineation. The S-type CPO is characterized by a point maximum of [010] normal to the foliation while [001] axes form a girdle corresponding to the foliation plane [*Helmstaedt et al.*, 1972]. The effect of the order-disorder transition on the activated glide systems and rheological properties of omphacite has been a matter of controversy. On the one hand, microstructural and CPO data of natural omphacite were interpreted such

that cation ordering in omphacite controls development of either L-type LPO (ordered structure) or S-type CPO (disordered structure) [Brenker *et al.*, 2002; Prior *et al.*, 1999]. On the other hand, a more recent study disagrees with a cation-ordering model for dislocation slip [Ulrich and Mainprice, 2005].

Given the challenges associated with performing deformation experiments at upper mantle conditions it is not surprising that the availability of mechanical data on clinopyroxenes correlates with the pressure necessary to stabilize the specific composition (Figure 2). The more sodic the composition, the higher are the required pressures. The calcic endmember, diopside, which is stable at room pressure, has been extensively investigated using single crystals [Ave Lallemand, 1978; Ingrin *et al.*, 1991; Jaoul and Raterron, 1994; Raterron and Jaoul, 1991; Raterron *et al.*, 1994], natural polycrystalline aggregates [Bystricky and Mackwell, 2001; Chen *et al.*, 2006; Kirby and Kronenberg, 1984], and synthetic polycrystalline aggregates [Dimanov *et al.*, 2003; Dimanov and Dresen, 2005; Majumder, 2005 #43; Majumder *et al.*, 2005]. Jin *et al.* [2001] and Zhang *et al.* [2006] performed deformation experiments at a pressure of 3 GPa on aggregates synthesized from natural omphacite crystals with a composition of $di_{73}jd_{27}$ (73 mol% diopside; 27 mol% jadeite) and $di_{58}jd_{42}$, respectively. Synthetic aggregates of jadeite were examined by Orzol *et al.* [2006]. Currently it is difficult to deduce the effect of composition on flow properties, since different experimental techniques and samples of different origin were used in the studies performed so far. Early work [Kolle and Blacic, 1982] suggests that hedenbergite ($CaFeSi_2O_6$) is stronger than chromian diopside. At face value, diopside aggregates appear to be stronger than jadeite aggregates at laboratory conditions yielding steady state dislocation creep [Orzol *et al.*, 2006]. In contrast, it has been concluded that jadeite is stronger than diopside at low to intermediate temperatures, where crystal plasticity controls deformation in indentation experiments [Dorner and Stöckhert, 2004]. The lack of a profound understanding of the rheological characteristics of complete solid-solution series of silicates is not restricted to pyroxenes. Only limited work has been performed on important rock-forming minerals such as plagioclase [e.g., Rybacki and Dresen, 2000] and olivine [Zhao *et al.*, 2007]. Stöckhert [2002] reviews the information from field-based and experimental studies on deformation mechanisms and stress levels in high pressure (HP) and ultra-high pressure (UHP) metamorphic rocks with the aim of constraining the physical conditions along subduction zones to depths of 100 km. HP and UHP rocks are either undeformed or deformed by dissolution-precipitation creep suggesting very low stress levels during (U)HP metamorphism in felsic rocks. Stöckhert concludes that deformation along subduction

zones with a subduction channel filled with crustal material is: (1) highly localized; and (2) occurs predominantly by Newtonian dissolution-precipitation creep at very low stress levels. Accordingly, available flow laws for dislocation creep provide an upper bound for stress levels along subduction zones within the uncertainties of the extrapolation of experimental flow laws to natural conditions.

Studies on eclogites show evidences for dislocation creep even at temperatures as low as 400-500 °C [Piepenbreier and Stöckhert, 2001; Van Roermund and Boland, 1981]. Deformation by dislocation creep at such low temperatures is incompatible with extrapolated flow laws for diopside [Boland and Tullis, 1986; Bystricky and Mackwell, 2001] which implies that Na-pyroxenes jadeite and omphacite have much lower dislocation-creep strength than diopside. Low creep strengths in naturally deformed eclogites may be explained by a strong water weakening effect in Na-pyroxenes [Buatier et al., 1991]. Clearly, further experimental studies on these materials are needed to resolve the “eclogite rheology problem”.

1.2. Scope and approach of this study

The effect of composition on mechanical properties in silicate solid solutions is not clear at present. Considering the knowledge on the rheological behavior of solid solutions of metals acquired in material science, it is not expected that the mechanical behavior of omphacite equals the mechanical behavior of the associated end members. Investigating and quantifying the rheological behavior of the intermediate omphacite compositions and also of the compositional endmembers, diopside and jadeite, is the subject of this study.

In order to determine the mechanisms of deformation and to quantitatively constrain the rheology of omphacite accounting for previous results at low pressures, deformation experiments are conducted on a) synthetic Fe-free polycrystalline omphacite aggregates with five different compositions along the jadeite-diopside-join and natural clinopyroxene samples, b) samples of a natural clinopyroxenite (Sleaford Bay, Australia), and c) at a range of pressures within the limitations due to the phase diagram of omphacite (Figure 2). The deformation experiments are performed at temperatures between 800°C and 1175°C, and with strain rates of 10^{-6} to 10^{-4} s⁻¹. Synthetic samples of the various compositions are prepared following identical preparation procedures and are tested in a single deformation

apparatus at identical conditions. Using synthetic samples has the benefit of providing readily comparable data.

Currently, experiments at the pressure mandated by stability of sodic omphacite can only be performed in Griggs-type apparatus. The apparatus exhibit limited resolution in stress even in their modified versions due to uncertainty in friction associated with the external measurement of axial loads [e.g., *Rybacki et al.*, 1998; *Tingle et al.*, 1993]. Clearly, mechanical data of higher quality could be gained for the calcic endmember in a gas apparatus (pressures <500 MPa). However, the benefits of a systematic study in a single apparatus outweigh the shortcomings of solid-medium apparatus in stress resolution as long as the prime interest is the effect of composition on the rheology of omphacite solid solution.

The effect of pressure on deformation mechanisms of silicate rocks is very important in geoscience. Here, the deformation data on synthetic omphacite aggregates and natural clinopyroxene samples at a range of pressures from 0.7 to 2.5 GPa will be compared with previous results at lower pressure (<500 MPa). Models for the pressure dependence of the deformation characteristics of silicates suggest a link between pressure and the amount of hydrogen incorporated in the lattice which in turn also strongly depends on Fe-content [e.g., *Chen et al.*, 2006; *Kohlstedt*, 2006]. Thus, the discussion in this thesis is concluded by analyzing the interrelation between the effects of pressure and hydrogen content on the rheology behaviour of omphacite.

Constraining the deformation behavior of eclogite rocks at upper mantle conditions will improve the understanding of interplate shear stresses at convergent plate boundaries and will serve as crucial input for large scale modeling addressing forced flow in the mantle wedge and localization of deformation in subduction zones.

2. Background

2.1. Eclogite classification

The term eclogite as a petrographic rock name is restricted to rocks of broadly basaltic composition which lack primary plagioclase and have a predominant assemblage of jadeite-bearing clinopyroxene and garnet [Bell and Kalb, 1969]. Smaller amount of certain other anhydrous minerals are widely recognized in eclogites. Quartz, kyanite, orthopyroxene and rutile are the most common. Coesite, diamond and aragonite are rarer, but notably are indicative of high pressures. The status of accessory hydrous silicates such as glaucophanitic, barroisitic or pargasitic amphibole, phengite, paragonite, phlogopite, talc zoisite and clinozoisite is more debatable [Smith and Etal, 1982]. It is proposed that the use of the specific litho-type name eclogite should be restricted to rocks with more than 70% garnet+jadeite-bearing clinopyroxene, compatible with broadly basaltic rock compositions.

The stability relationships between eclogite facies mineral assemblages and amphibole-bearing blueschist, amphibolite or greenschist facies assemblages are complex and depend on the chemical potential of H₂O in the rock systems undergoing metamorphism. The critical influence of H₂O-activity on the P-T stability of clinopyroxene-dominant eclogite facies assemblages relative to amphibole-dominant assemblages of other metamorphic facies is illustrated in experimental results [Asahara and Ohtani, 2001; Bell and Kalb, 1969]. Natural eclogites have been subdivided into several subgroups (Table 1). The occurrence of eclogites in different geological environments and various mineralogical criteria indicate that eclogites have formed over a wide range of P-T conditions. The classification scheme of Eskola [Eskola, 1921] emphasized the occurrence of eclogites in four contrasted geological settings. The three-fold subdivision scheme of Coleman et al. [Coleman et al., 1965] into eclogite groups A, B, C is based on observed differences in the compositions of the constituent garnets and clinopyroxenes. However, geological setting was emphasized in the classification scheme of Smulikowski [Smulikowski, 1968]. The appropriate equilibration temperature estimates for the three groups of eclogites can be obtained from experimentally-based calibrations of the Fe²⁺ - Mg²⁺ exchange reaction between coexisting garnets and clinopyroxenes [Raheim and Green, 1975].

Reference and subdivision criteria			Proposed scheme	
Coleman et al. (1965) largely mineral compositions	Smulikowski (1964) geological settings	Eskola (1921) geological occurrences	likely origin	equilibrium temperature
Group A pyrope >55 mol. % least jadeitic clinopyroxene	Group I mantle eclogites and garnet websterites associated with peridotites	Type 1 xenoliths in kimberlites, etc.	upper mantle	high 900°C
		Type 2 layers and lenses In alpine-type peridotite bodies	tectonically thickened continental crust	medium
Group B 30-55 mol. % pyrope	Group III common eclogites	Type 3 lenses in migmatitic gneiss complexes		550°C
Group C Pyrope < 30 mol. % most jadeitic clinopyroxene	Group II ophiolitic eclogites	Type 4 blocks in blueschist facies terrains	subducted oceanic crust and arc-trench sediments	low

Table 1: Classification of eclogites and subdivision criteria [after Carswell, 1990].

2.2. Structure and phase stability of omphacite

Omphacite, $(\text{Ca},\text{Na})(\text{Mg},\text{Fe}^{2+},\text{Fe}^{3+},\text{Al})[\text{Si}_2\text{O}_6]$ is the characteristic clinopyroxene occurring in eclogites, but is also found in rocks without garnet, e.g. glaucophane schists and amphibolites. The binary system jadeite-diopside has been studied at pressures of 3 and 4 GPa [Bell and Kalb, 1969] and at 2.8 GPa [Pati et al., 2000]. These studies showed that there is complete solid solution between the two phases at 2.8 GPa and above. At lower pressures or higher temperatures and in the absence of free silica, omphacite breaks down to nepheline, albite and a diopside rich omphacite. In the presence of free silica, omphacite forms albite and a diopside-rich omphacite. The diopside-rich omphacites are stable at

lower pressures. Pure jadeite breaks down to albite and nepheline. The stability of jadeite is pressure sensitive and therefore provides a useful geobarometer for eclogitic rocks. In general, diopsidic omphacite is more stable at lower pressures on the silica-undersaturated jadeite-diopside join than on the silica-saturated albite-diopside join [Bell and Kalb, 1969]. Figure 2 presents the position of the phase stability of different compositions of jadeite-diopside solid solution in a pressure-temperature diagram and in the absence of free silica.

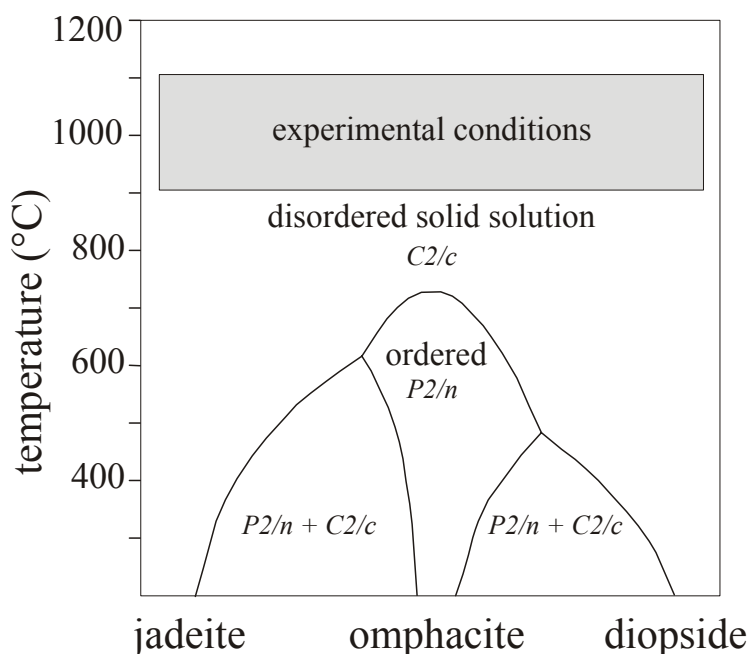


Figure 1: Phase diagram for the jadeite-diopside system [after Carpenter, 1980]. While omphacite crystals of intermediate composition may exhibit ordered structure (space group $P2/n$) up to temperatures of about 700°C, all aggregates tested in the current experiments are in the disordered state (space group $C2/c$) as evidenced by X-ray diffraction.

The system jadeite-diopside shows a thermodynamically continuous transition between disordered and ordered structure [Carpenter, 1983]. At intermediate compositions and sufficiently low temperatures (<700°C), omphacite crystallizes in ordered form (space group $P2/n$) while the more calcic or more sodic omphacites maintain the disordered structure (space group $C2/c$) of the compositional endmembers, diopside and jadeite (Figure 1). The order-disorder transition is considered to involve a nucleation-growth mechanism. To initiate the ordering process during cooling, it is assumed that there must be sufficient Al in octahedral co-ordination. An antiphase domain structure for an ordered omphacite has

been observed by electron microscopy and has been attributed to this order-disorder transition [Champness, 1993]. The domains are relatively large (0.2 μ m) and appear to nucleate on dislocations and subgrain boundaries.

Heating experiments on natural omphacite ($\text{Na}_{0.48}\text{Al}_{0.51}\text{Ca}_{0.47}\text{Mg}_{0.42}\text{Fe}_{0.08}\text{Si}_{1.98}\text{O}_6$) at 1.5 to 1.8 GPa have established 750 ± 20 °C for the order-disorder transition [Fleet et al., 1978]. Experiments on the kinetics of cation ordering in omphacites show that a cooling rate of faster than $\sim 10^\circ\text{C}$ per day through the range of 850 to 750°C is necessary for an omphacite to remain disordered during continuous cooling at a pressure of 1.8 GPa [Carpenter, 1981].

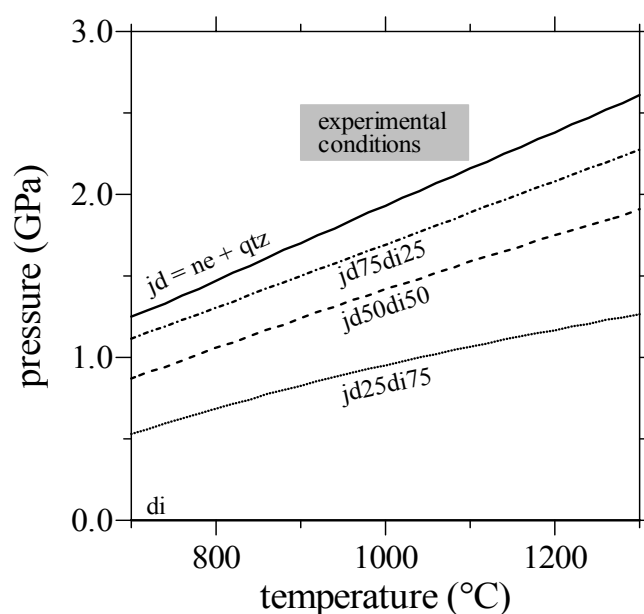


Figure 2: Stability field of omphacite (om) in the system CaO-MgO-Na₂O-Al₂O₃-SiO₂ calculated i) assuming that free SiO₂ does not occur in the presence of the pyroxene phase and ii) employing the thermodynamic data set of Holland and Powell [1998] and the mixing model of Green et al. [2007] by distributing cations according to the internal equilibrium $2 \text{ om} \rightarrow \text{jd} + \text{di}$. The upper solid line represents the univariant equilibrium between the high-pressure phase jadeite (jd) and the phase assemblage “nephelin + quartz”. The calcic endmember diopside (di) is stable at all temperatures. Curves between the two endmember-curves correspond to intermediate compositions in steps of 25% in mol fraction. The field labeled “experimental conditions” approximates confining pressure-temperature conditions of the performed deformation tests considering friction of up to 15%.

2.3. Partial melting of eclogite and omphacite

Few experimental studies have investigated partial melting of eclogite [Rapp *et al.*, 1999; Yaxley and Green, 1998]. All studies agree on the siliceous character of partial melts derived from eclogitic bulk compositions with or without added water. Partial melts of eclogite in anhydrous systems contained ~63% SiO₂, whereas partial melts in hydrous systems contained up to 63% SiO₂ [Green, 1982]. All studies report melts noticeably enriched in Na₂O and TiO₂ relative to their source.

Isobaric partial melting experiments were conducted with a Fe-free synthetic composition of eclogite [Klemme *et al.*, 2002]. All experiments were performed at 3 GPa pressure and temperatures 1100°C - 1400°C under nominally anhydrous conditions. Although H₂O is well known to affect the position of the solidus, its influence on rutile saturation and trace element partitioning is relatively small [Green and Pearson, 1986; Green, 2000; Ryerson and Watson, 1987]. It should be noted that Fe has a relatively small effect on mineral-melt partitioning because of the near ideal mixing between Fe and Mg in most minerals and melts [Wood and Blundy, 1997]. The clinopyroxene crystals were generally around 50 µm in diameter; garnets were rounded and mostly 70 to 100 µm in diameter in the higher temperature (more than melting temperature of clinopyroxene) run.

The hydrous phase relations of primitive mantle compositions in the CaO-MgO-Al₂O₃-SiO₂-H₂O system with 1, 2, and 5 wt. % H₂O have been investigated at 4, 6.5, and 8 GPa [Asahara and Ohtani, 2001]. In this study dissolution temperature of garnet decreases more rapidly than the other phases at 4 and 6.5 GPa. Garnet is stable up to a high degree of melting at 8 GPa. The disappearance temperature of garnet decreases remarkably by about 400°C under the condition of 5 wt. % H₂O at 4 and 6.5 GPa.

The experimental investigations of high-temperature creep of almost pure diopside single crystals [Ingrin *et al.*, 1991; Raterron and Jaoul, 1991] revealed that the mineral begins to melt incongruently and to exsolve numerous tiny precipitates of a molten phase well below its liquidus temperature T_M (~1350°C). In the above experiments, the initiation of melting was detected at a temperature as low as ~1140°C. The composition of the molten precipitates is enriched in silica [Doukhan *et al.*, 1993]. If the material is rapidly cooled to ambient temperature the precipitates are quenched to glass, but for slower cooling rates the precipitates may either redissolve or evolve to a mixture of glass and crystallites of wollastonite (CaSiO₃). Such tiny precipitates can directly only be detected by transmission electron microscopy [Asahara and Ohtani, 2001]. This phenomenon is called early partial

melting (EPM). In the deformation experiments of Raterron and Jaoul [Raterron and Jaoul, 1991], EPM was indirectly detected through the interaction of the precipitates of melt with the mobile dislocations. EPM has been observed by Bolland and Tullis [1986] in clinopyroxenite that deformed at $T=1250^{\circ}\text{C}$ and 300 MPa confining pressure.

2.4. Crystal-plastic deformation

Dislocations are linear defects in crystals. A dislocation is not simply a linear collection of point defects, but is a special category of irregularity that may be visualized as a line in the slip plane that separates slipped from unslipped parts of the crystal. The Burgers vector \vec{b} closes a circuit around the dislocations in a section normal to the dislocation line. In an edge dislocation the dislocation line and Burgers vector are perpendicular, while in a screw dislocation they are parallel.

The density of dislocations is given by the total length of dislocation lines per volume. Dislocations are thermodynamically unstable because they represent a local high energy region in a crystal where the atomic bounds are elastically distorted. The energy per unit length of dislocation depends on the magnitude of the Burgers vector and the shear modulus of the material. Under differential stress dislocation lines expand outward until they leave the crystal or meet obstacles. As dislocations progressively leave the crystals, the Frank-Read source mechanism produces high strain by multiplication of dislocations. At this dislocation, loops are emitted from a part of a dislocation line which is pinned at two points and affected by stresses above a critical stress.

In glide controlled creep local nucleation pairs of kinks bring the dislocation to the next low energy glide plane. The applied stress decreases the activation energy for the migration of kinks. At low temperatures or high strain rates diffusion-controlled processes like diffusion flow or dislocation climb do not proceed fast enough and only glide motion of dislocations is dominant. In many nonmetals large stress is needed to move a dislocation, even if the crystal contains no obstacles.

At higher temperatures dislocation climb occurs, as jogs migrate and atoms diffuse into or out of the extra half plane. Mechanisms based on this climb-plus-glide sequence are referred to as *climb-controlled creep* [Weertman, 1963]. In this mechanism the rate-controlling process at an atomic level is the diffusive motion of single ions or vacancies to or from the climbing dislocation rather than the activated glide of the dislocation itself.

Climb controlled creep is a thermally activated process and the climb velocity is controlled by diffusion of vacancies to or from the dislocations, and therefore depends on the diffusion coefficient of the relevant point defects. In metals the activation energy of self-diffusion, in ionic crystal the diffusion coefficient of the slower species (usually anion) and for alloys diffusion of the solvent or the solute is important. For complicated minerals, activation energy for creep is not simply related to the activation energy of diffusion of any one species [Poirier, 1985]. Recrystallization and recovery reduce dislocation density by climb of dislocation, i.e., activates softening mechanism, and therefore counteracts the hardening effect of dislocation glide [Poirier, 1985].

At medium stresses and high temperatures, dislocation glide and climb occur together. At these conditions, strain is mainly produced by the glide of dislocations. The rate controlling process, however, is dislocation climb. In steady state creep the contribution of hardening and recovery become balanced and in principal unlimited strain occurs at a constant stress. It is found empirically that the creep rate at steady state condition can be represented by the following equation [Ranalli, 1995]:

$$\dot{\varepsilon} = A \cdot \sigma^{n'} \cdot \exp\left(-\frac{Q}{RT}\right)$$

where $\dot{\varepsilon}$ denotes the strain rate, n' the stress exponent, T the absolute temperature, σ the differential stress and Q the molar activation energy of the rate controlling mechanism. A is a constant and R the gas constant. Because of the dependence of $\dot{\varepsilon}$ on σ , this equation is commonly referred to as the power law creep equation. Sherby and Burke [Sherby and Burke, 1968] have defined two ranges of stressing pure metals within which n' is independent of stress. At very low stresses $n'=1$, which means that stress is linearly related to strain rate as in Newtonian-viscous fluids. At higher stresses n' varies from 3 to 8. This is the nonlinear power-law region. The differential stress of geodynamic interest is in the range of 1 to 100 MPa [Ranalli, 1995]. At these stresses and at high temperatures, silicate minerals flow by power-law creep with n' between 3 to 5 [Ranalli, 1995].

2.5. Activation energies of kinetic processes in pyroxenes

In most power low creep models the strain rate is related to the self-diffusion coefficient of the slowest species inside the sample. Therefore the activation energy for self-diffusion of the slowest moving species must be the same as the creep activation energy. Rather

recently, it could be shown that the activation energies of creep and diffusion of Si in olivine are indeed identical [Dohmen *et al.*, 2002].

In the previous section we assumed that jog formation controls the climb velocity and the rate at which vacancies diffuse toward or away from the dislocations. At high concentrations of jogs the climb velocity is nearly equal to the jog velocity along the dislocation. If the concentration of jogs is under-saturated for dislocations in a given sample, the creep activation energy will be larger than the self-diffusion energy, because some energy is required for jog formation. This relation was demonstrated for olivine [Ranalli, 1995].

The creep test and diffusion experiments were carried out on natural and synthetic samples of jadeite and diopside. The results are compiled in Table 1. A power-law creep equation is applied to obtain creep parameters. Wet material is softer than dry material. The difference is related to the water content and it is generally less than 50 %. The advantages of using synthetic samples are mainly in the control of composition, chemical environment, grain size and potential creep mechanisms. Crystal orientations can be controlled in single crystals.

The lower part of Table 2 shows the activation energies obtained from diffusion experiments. Activation energy is dependent on the composition of the samples and the chemical environment (Fe content, oxygen fugacity, Si activity). There is no further data on silicon self-diffusion. Diffusion experiments are performed at room pressure, while creep experiments except one are carried out under confining pressure. The effective diffusivity may also be affected by diffusion along the dislocation core (pipe or core diffusion). In order to exclude the possibility that grain-boundary diffusion does not contribute to bulk mass transport, activation energies for self diffusion were taken from single-crystal diffusion experiments [Kirby and Raleigh, 1973].

A comparison of diffusion data shows that silicon is the slowest species and therefore it controls creep rates in dislocation climb processes [Dimanov *et al.*, 1996]. Maybe due to strong covalent bonding in SiO_4 tetrahedral silicon ions diffuse slower than cations and oxygen in diopsides.

A comparison of data for temperatures below 1500°K shows that activation energies for creep are larger than for self-diffusion of silicon in diopside. We can explain this by jog formation energy in under-saturated samples, so that the activation energy for creep is the sum of the energy for jog formation in under-saturated samples and the energy for self-diffusion.

material	activation energy	method	reference
synthetic jadeitite	326 ± 27 kJ / mol	power law	Orzol [2002]
natural jadeitite	263 ± 19 kJ / mol	power law	Orzol [2002]
wet diopside	490 ± 80 kJ / mol	power law	Boland and Tullis [1986]
dry diopside	380 ± 30 kJ / mol	power law	Kirby and Kronenberg [1984]
dry diopside	760 ± 40 kJ / mol	power law	Bystricky and Mackwell [2001]
diopside single crystal orientation(1) orientation(2)	742 ± 31 kJ / mol 442 ± 29 kJ / mol	power law	Raterron and Jaoul [1991]
oxygen self-diffusion in diopside	226 kJ / g-atm O	diffusion	Farver [1989]
oxygen self-diffusion in diopside	457 kJ / mol	diffusion	Ryerson and Mckeegan[1994]
diffusion of Ca in synthetic diopside	280 kJ / mol for<1515°K 951 kJ / mol for>1515°K	diffusion	Dimanov and Ingrin [1995]
silicon self-diffusion in diopside	211 kJ / mol	diffusion	Bejina and Jaoul [1996]
Mg and Ca self-diffusion in diopside	> 566 kJ for Mg 892-988 kJ for Ca	diffusion	Azough et al. [1998]
oxygen self-diffusion in diopside	310 kJ / mol	diffusion	Pacaud et al. [1999]

Table 2: Activation energy values for creep of diopside and jadeite in power law creep and self-diffusion of their constituents.

3. Materials and methods

3.1. Analytical methods

The cylindrical samples were cut into two parts along (in two cases perpendicular) their axes. For all samples, doubly polished thin sections were prepared from one of these parts for optical microscopy and scanning electron microscopy (SEM) as well as for electron backscatter diffraction (EBSD) and electron microprobe (EMP) analysis. For EBSD analysis, thin sections were chemically polished using a colloidal silica suspension (SYTON®). For a number of samples, the second half was used for the preparation of thin foils for transmission electron microscopy (TEM) and polished slabs with a thickness of 150 to 200 μm for Fourier-transform infrared microspectrometry (FTIR).

The phases in the synthesized samples were determined by powder X-ray diffraction analysis (XRD). The crystallographic orientations and microfabrics of synthetic and deformed samples were analyzed by SEM, using a LEO 1530 instrument with field emission gun and forescatter detector. For EBSD analysis, the SEM was operated at an accelerating voltage of 20 kV, the thin section being tilted at an angle of 70° with respect to the beam, and with a working distance of 25 mm. The HKL *CHANNEL5* software was used for indexing and processing of diffraction data. Automatic EBSD measurements were performed to obtain orientation maps and grain geometry. A misorientation angle of 10° was chosen as threshold between low and large angle grain boundaries. Grain size is given as the diameter of a circle of equivalent area. The shape preferred orientation (SPO) was gained from the orientation of the long axes of grains in the 2D-sections. Crystallographic preferred orientations (CPOs) are displayed as density plots in equal area projections of the lower hemisphere. The contours in the density plots are scaled by multiples of a uniform distribution (MUD). Forward scattered orientation contrast (OC)-imaging was performed to investigate the substructure within the grains, in particular the occurrence of twins. OC-imaging provides qualitative information on the crystallographic orientation [e.g., *Humphreys et al.*, 2001; *Prior et al.*, 1999]. Regions of different crystallographic orientation appear in different gray shades.

Arrangement and density of dislocations were analyzed by transmission electron microscopy (TEM). For the preparation of TEM foils a GATAN PIPS ion mill was used. The TEM foils were examined in a Philips EM301 transmission electron microscope operated at 100 kV. All diffraction contrast images were produced using bright-field (BF) conditions.

Type and concentration of water and water-related defects were studied by Fourier-transform infrared microspectrometry (FTIR) [e.g., *Kronenberg and Wolf*, 1990] at room temperature using an infrared spectrometer (Bruker IFS 48) with an attached IR-microscope. The IR-microscope permits spectrometric analysis with a spatial resolution of about 0.1 mm using polished sections of 0.1 to 0.3 mm thickness. The hydrogen concentration in samples was calculated from the absorption spectra in the wave-number range of 3000 to 4000 cm^{-1} , following the method proposed by Paterson [1982].

3.2. Starting material

Synthetic omphacite aggregates and natural clinopyroxene samples from the Precambrian metamorphic terrain of Sleaford Bay (South Australia) were used in this study.

3.2.1. Synthetic omphacite aggregates

3.2.1.1. Synthesis

Often synthetic aggregates are chosen for deformation studies to control chemical compositions and starting microstructure of material [*Rutter*, 1993]. Natural ultra-high pressure rocks are generally not appropriate as they have been affected by retrogression and deformation during exhumation [*Stöckhert and Renner*, 1998]. To synthesize a material with a suitable microstructure, the nucleation and growth of the grains need to be controlled. Synthetic polycrystalline samples can be produced using appropriately composed gels, glasses or oxides as starting materials. Building upon previous experience by *Dorner* [1999] and *Orzol et al.* [2006], glass powders with five stoichiometric compositions equally spaced along the join between diopside and jadeite were used for synthesis. First, powders were pressed into gold capsules with a length of 18 mm, a wall thickness of 0.2 mm and an outer diameter of 6 mm by uniaxial cold pressing at 100 MPa in several steps. The cold-pressed samples were dried at 150°C for at least 12 hours, and subsequently the capsules were mechanically sealed and stored again in an oven at 150°C.

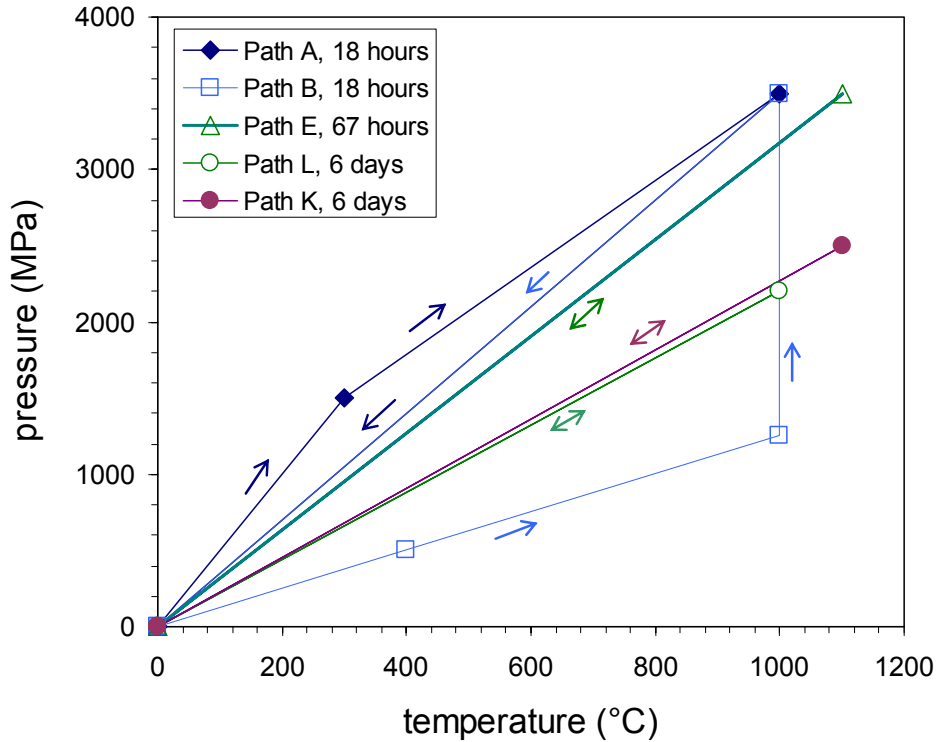


Figure 3: Examples of tested paths for the synthesis of the polycrystalline omphacite aggregates. The time spent at peak conditions is indicated in the legend.

A piston cylinder apparatus with a vessel of 25.4 mm diameter was used for the synthesis experiments. It comprises a servohydraulic control unit for confining pressure and a programmable temperature controller [Renner *et al.*, 1997]. Dry sodium chloride (NaCl) served as pressure transmitting medium. Heating was provided by a graphite resistance furnace. A NiCr-Ni thermocouple was used for measuring temperature in the upper part of samples. Three samples were synthesized in a single run. Several P - T - t paths in the stability field of jadeite were tested to optimize the microstructure of samples (Figure 3). We found that a pressure of $p = 2.2$ GPa, a temperature of $T = 1000^{\circ}\text{C}$ and a run time of 6 days are appropriate with respect to resulting grain size and homogeneous distribution of grains in samples.

3.2.1.2. Microstructure and composition of synthetic samples

Seventeen synthesis experiments were carried out to optimize the starting microstructure and to provide starting material for deformation tests. Only for 100%di-samples, we found 100% crystallization for all paths. The optical micrographs and SEM images of synthetic samples show nearly similar grain shape (average grain sizes are different for five composition of omphacite) with simply curved high angle grain boundaries (Figure 4). Synthesized samples exhibit grain sizes in the range 6 to 100 μm with a tendency for grain size to be smallest for samples with a composition of $\text{di}_{25}\text{jd}_{75}$. Grain sizes were determined by automated EBSD measurements or line intercept determinations on SEM images. Grain size distribution and grain shape varies systematically with composition. In diopside samples, grains are mostly equant and of narrow size range while grains in jadeite samples exhibit irregular shape and a wide range in size (Figure 5). Intermediate compositions show transitional features between those of the two compositional endmembers. Generally, grains don't show undulatory extinctions or subgrains under the optical microscope; however, the state of grains with a size of only a few microns is difficult to resolve optically.

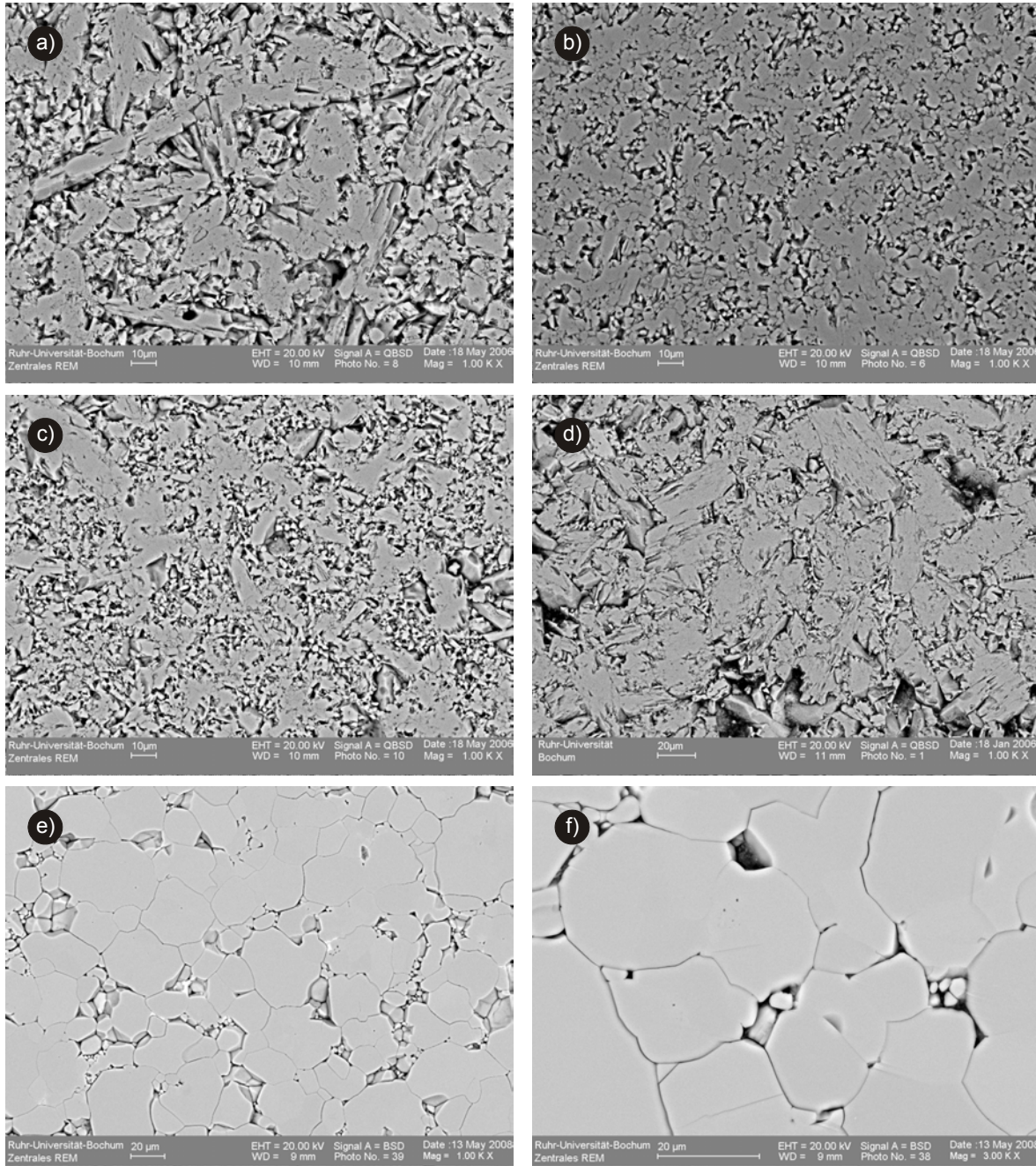


Figure 4: BSE images showing microstructure in undeformed samples synthesized for ~6 days. a) jadeite at $P=2.2$ GPa, $T=1000^{\circ}\text{C}$, b) $\text{di}_{25}\text{j}_{75}$ at $P=2.5$ GPa, $T=1100^{\circ}\text{C}$, c) $\text{di}_{50}\text{j}_{50}$ at $P=2.2$ GPa, $T=1000^{\circ}\text{C}$, d) $\text{di}_{75}\text{j}_{25}$ at $P=2.2$ GPa, $T=1000^{\circ}\text{C}$, e,f) diopside at $P=2.2$ GPa, $T=1000^{\circ}\text{C}$. Omphacite of jadeite-rich compositions show an acicular grain shape, whereas omphacite of diopside-rich compositions show an isometric grain shape with smoothly curved grain boundaries.

The EBSD analyses show very weak SPOs in synthesized samples (Figure 5). Grains of a size below 10 μm are randomly oriented (Figure 5); larger grains exhibit a weak SPO in synthetic diopside samples. An appreciable CPOs was not found in any of the samples after synthesis.

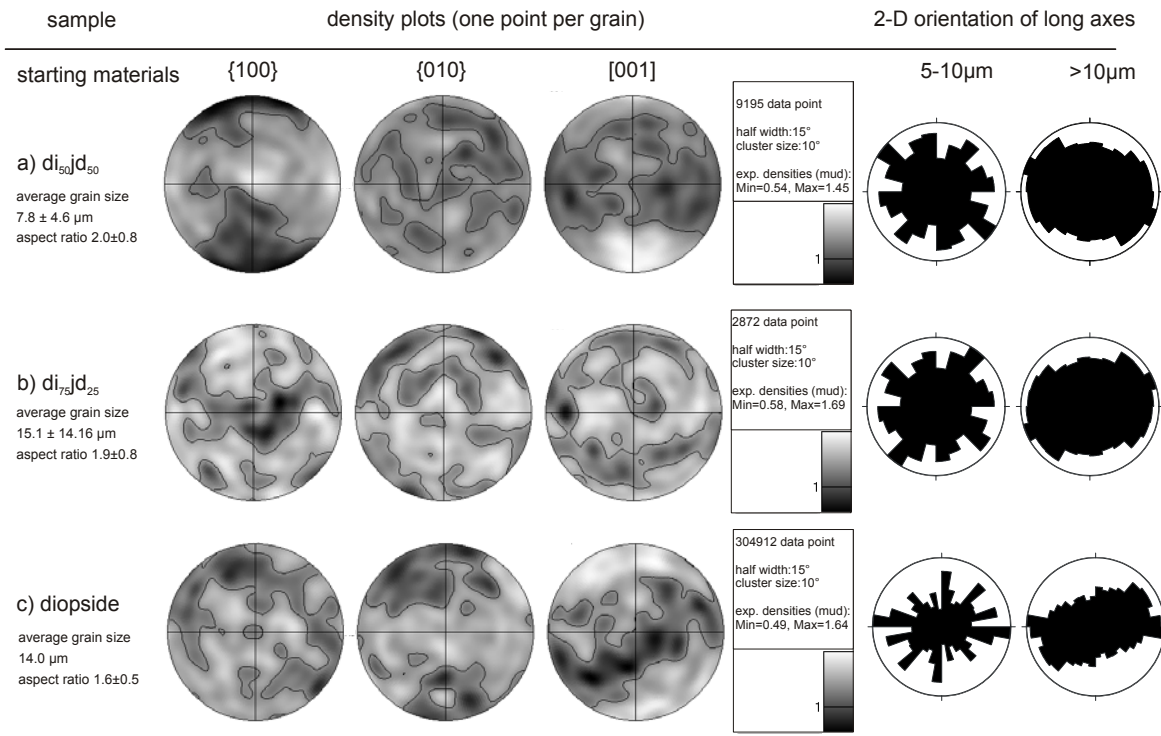


Figure 5: Selected automated EBSD measurements (2 μm step size) of starting materials. Left) density plots (equal area projection of the lower hemisphere) are displayed for the poles to (100) and (010) planes and the [001] direction. Right) 2-D orientation of long axes of grains with diameters <10 μm and >10 μm are displayed in a rose diagram. In a) and b) the section perpendicular and in c) parallel to the cylinder axis of the samples are displayed.

TEM micrographs of starting material reveal grains with smoothly curved to straight boundaries and poor in dislocations. An unspecified phase, interpreted to represent a quenched non-wetting hydrous melt, occurs between grains (Figure 6).

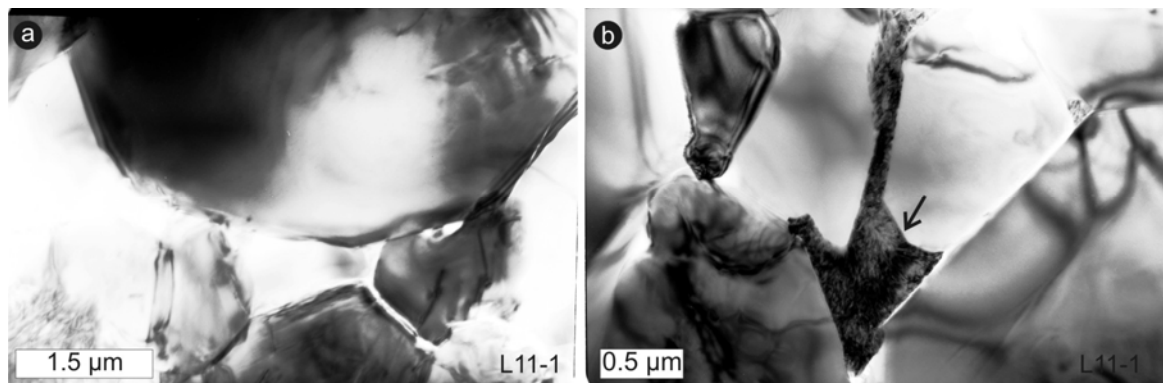


Figure 6: TEM-bright field micrographs of starting material ($di_{75}jd_{25}$, sample L11) showing grains with smoothly curved to straight boundaries and poor in dislocations. An unspecified phase, interpreted to represent a quenched non-wetting hydrous melt, occurs between the jadeite crystals (arrow in b).

Degree of crystallization and crystal structure in synthesized samples were determined by powder X-ray diffraction analysis. Within the limit of detection, the X-ray diffraction analysis indicates a single crystalline phase in synthesized omphacite aggregates (Figure 7). However, TEM analysis revealed the presence of a secondary phase in jd - and $di_{25}jd_{75}$ - samples (Figure 6). The volume percentage is less than about 3% in jd -samples and even less in $di_{25}jd_{75}$ - samples. The exclusive occurrence at triple junctions and the gently curved appearance are features often found for melt inclusions. Furthermore, the X-ray pattern of synthetic aggregates corresponded to disordered state of omphacite (Figure 8).

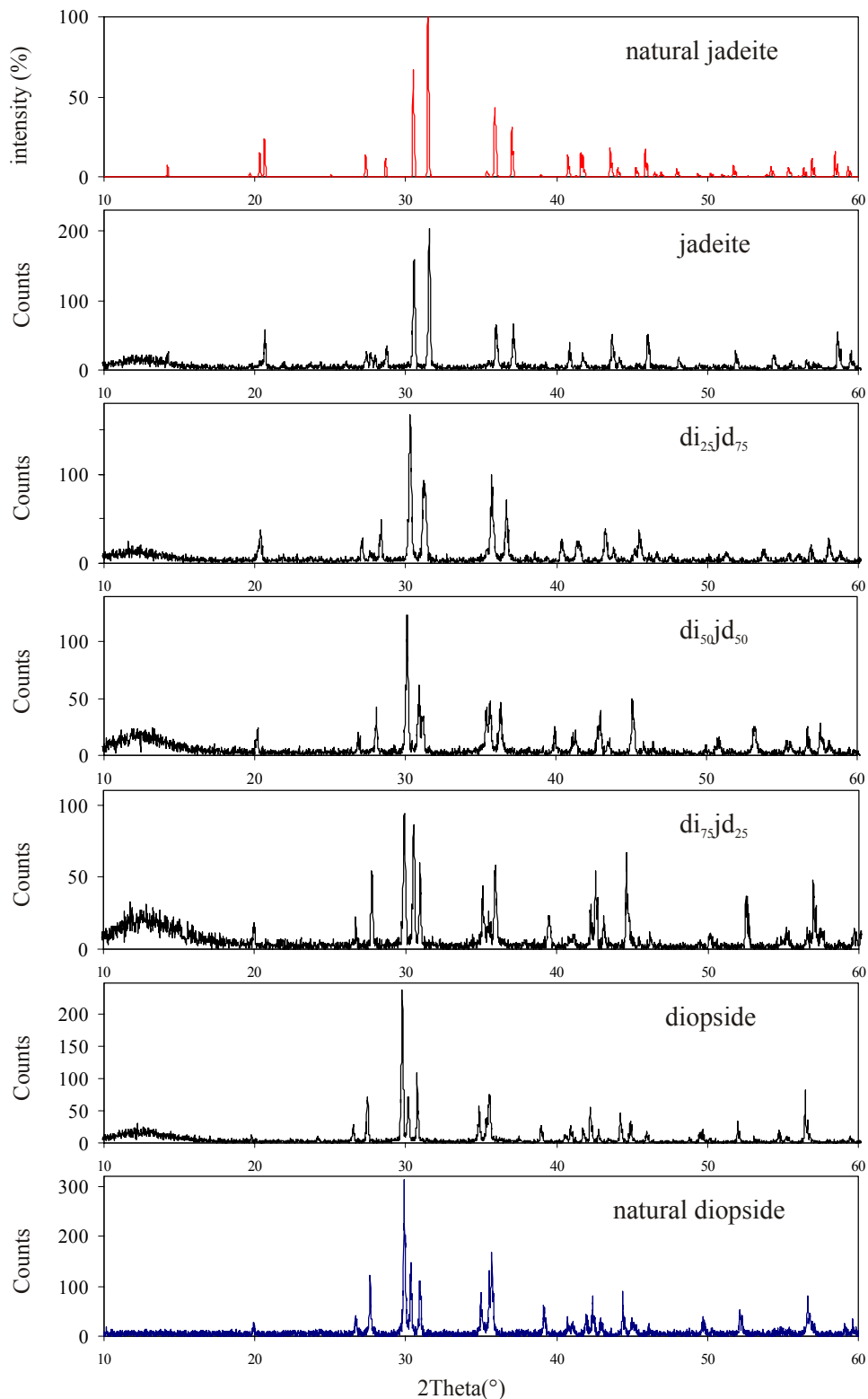


Figure 7: X-ray diffraction patterns for different composition of omphacite aggregates and for natural diopside (Yakutia, Siberia, Russia with composition of $\text{CaMgSi}_2\text{O}_6$) and natural jadeite (San Benito County, California with composition of $\text{NaAl}_{0.9}\text{Fe}^{3+}_{0.1}\text{Si}_2\text{O}_6$) samples.

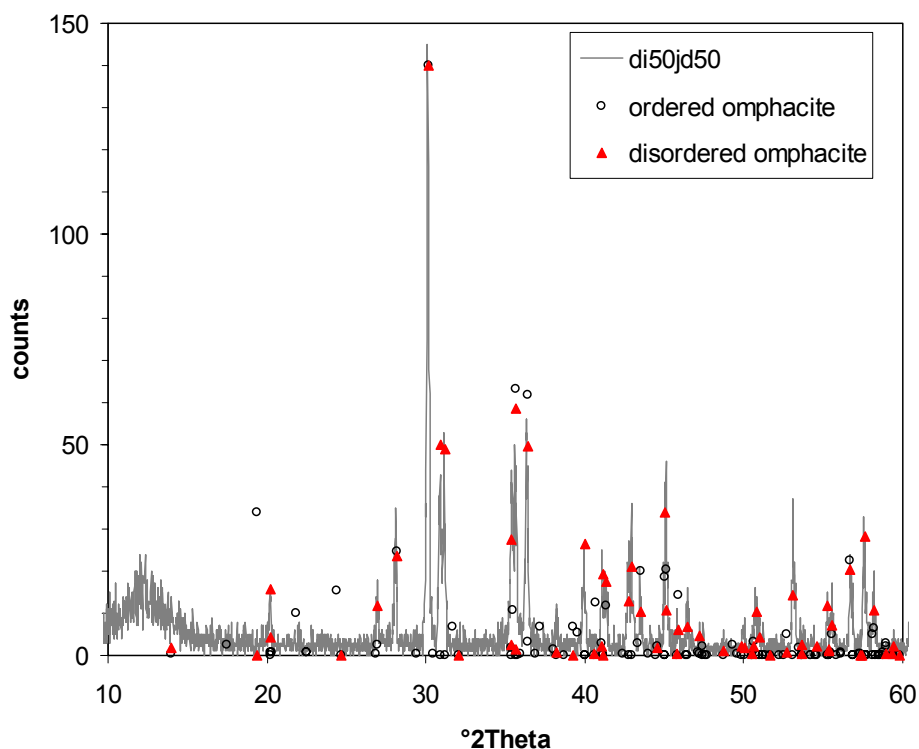


Figure 8: Powder-cell pattern (green and red point) for ordered and disordered omphacite (by W.Kraus and G.Nolze version 2.4, 2000) and X-ray diffraction pattern for di50jd50 synthetic omphacite sample (dark line). Additional peaks in the diffraction pattern for synthetic samples are due to the gold of the capsule used for synthesis. The X-ray pattern shows disordered state of omphacite.

The chemical compositions of synthesized samples were determined by electron microprobe (EMP) analysis (jd₁₀₀: Na_{0.97}Al_{1.01}Si₂O₆; di₂₅jd₇₅: Na_{0.72}Al_{0.76}Ca_{0.26}Mg_{0.26}Si₂O₆; di₅₀jd₅₀: Na_{0.48}Al_{0.51}Ca_{0.50}Mg_{0.51}Si₂O₆; di₇₅jd₂₅: Na_{0.24}Al_{0.26}Ca_{0.76}Mg_{0.76}Si₂O₆; di₁₀₀: Al_{0.01}Ca_{1.00}Mg_{0.97}Si_{1.96}O₆). The major constituting oxides of the omphacite aggregates after synthesis are presented in Table (3) based on *electron microprobe analyses*.

composition	jadeite	di₂₅jd₇₅	di₅₀jd₅₀	di₇₅jd₂₅	diopside
w (%) Na ₂ O	14.91	10.46	6.83	3.45	0.02
w (%) Al ₂ O ₃	26.25	18.44	12.02	6.21	0.34
w (%) CaO	0.03	7.90	14.08	19.94	25.98
w (%) MgO	0.05	5.62	10.20	14.36	17.87
w (%) SiO ₂	59.40	58.23	57.66	56.78	53.17
w (%) FeO	0.04	0.01	0.02	0.03	0.00
w (%) K ₂ O	0.01	0.01	0.01	0.01	0.00
w (%) total	100.68	100.68	100.82	100.77	98.49

Table 3: Electron microprobe (EMP) analysis for synthetic omphacite aggregates samples.

3.2.2. Natural samples

A comprehensive description of natural Sleaford Bay clinopyroxenite was given by Kirby and Christie [1977]. The composition of $\text{Na}_{0.01}\text{Al}_{0.01}\text{Ca}_{0.96}\text{Mg}_{0.69}\text{Fe}_{0.15}\text{Si}_{1.97}\text{O}_6$ was determined by electron microprobe analysis. In addition, Mauler et al. (2000) reported quartz (about 5%), apatite (less than 1%) and opaque minerals (1%) to be present. The size of the polygonal grains of $\sim 280 \mu\text{m}$ was determined based on SEM and optical micrograph images (Figure 9). The clinopyroxenite rock does not show any apparent foliation and indications of intracrystalline deformation, such as undulose extinction and deformation lamellae within grains, are not found. Grain boundaries are generally straight or gently curved and intersect at triple junctions with angles of $\sim 120^\circ$ (Figure 9).

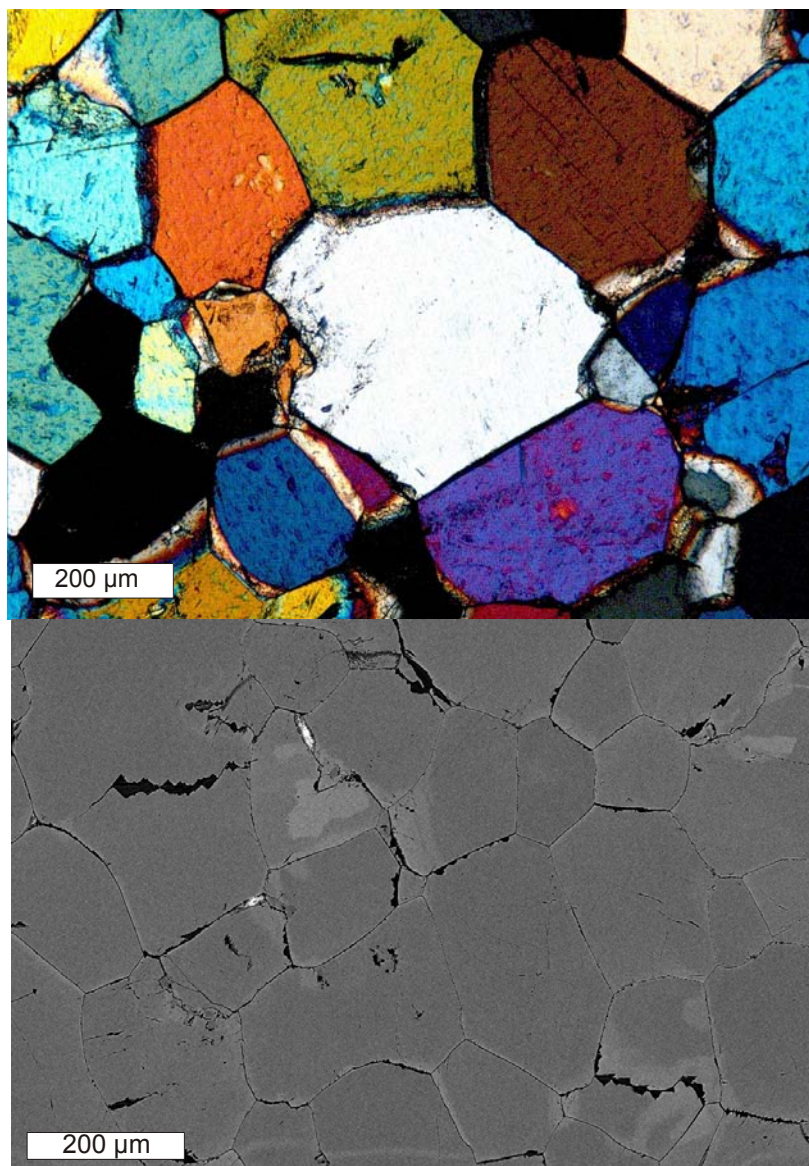


Figure 9: Cross-polarized optical micrograph (top) and BSE image (bottom) of natural Sleaford Bay clinopyroxenite. The grains show inhomogeneous chemical composition especially in the vicinity of grain boundaries.

3.2.3. Hydrogen content

Fourier-transform infrared (FTIR) spectras exhibit broad absorption bands between 3000 and 3700 cm^{-1} for synthetic omphacite aggregates (Figure 10). In agreement with previous studies [*Bromiley and Keppler, 2004; Bromiley et al., 2004*], jadeite and diopside samples additionally show pronounced peaks at 3614 and 3650 cm^{-1} , respectively, while such peaks

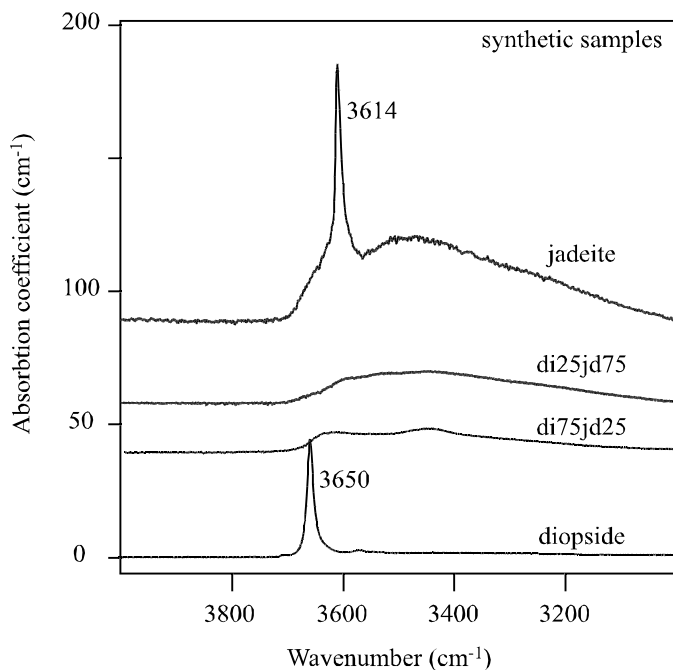


Figure 10: FTIR spectra for synthetic omphacite aggregates.

do not occur for intermediate compositions (Figure 10). Table (4) shows the quantitative evaluation of the absorption spectra for synthetic and natural samples. Estimated bulk hydrogen content of our synthetic samples systematically decreases from sodic to calcic compositions (Table 4). In comparison to experimentally determined solubility of hydrogen in synthetic Na-rich clinopyroxene and Cr-diopside [*Bromiley and Keppler, 2004; Bromiley et al., 2004*], all our synthetic omphacite samples appear to be above saturation (Figure 25).

composition	sample	water/hydrogen content			temperature (°C)	pressure (GPa)
		(mol H ₂ O/l)	(ppm H ₂ O)	(H/10 ⁶ Si)		
jd	L12-4-A	0.512	2793	35471	1100	2.2
	L12-4-B	0.530	2891	36715	1100	2.2
di ₂₅ jd ₇₅	L13-3-A	0.169	922	11709	1100	2.2
	L13-3-B	0.155	845	10731	1100	2.2
di ₅₀ jd ₅₀	L13-2-A	0.110	600	7620	1100	2.2
	L13-2-B	0.0947	517	6565	1100	2.2
	L13-2-C	0.0889	485	6159	1100	2.2
di ₇₅ jd ₂₅	L11-1-A	0.109	595	7556	1100	2.2
	L11-1-B	0.108	589	7480	1100	2.2
di	L32-1	0.0848	463	5880	1100	2.2
natural clinopyroxene	SB	0.0032	18	229		

Table 4: Hydrogen content of omphacite aggregates (synthesized at given conditions) and one natural clinopyroxene sample (SB). The water content by weight is calculated using 3.3 g/cm³ as average density of samples. The bulk water/hydrogen contents were estimated from FTIR spectra according to the method outlined by *Paterson* [1982]. For the synthetic samples, the reported values represent a single FTIR analysis while for the samples of the natural clinopyroxeneite (SB) averages of 10 analyses (with standard deviation of 0.00101 mol H₂O/l) are given.

3.3. Deformation experiments

3.3.1. Experimental procedure

Synthesized samples and natural clinopyroxene samples were machined to cylindrical shape with ~7.3 mm length and ~3.7 mm diameter, and then dried at 150°C for at least 24 hours. Platinum capsules with a thickness of 0.1 mm were used for jacketing. All deformation experiments were performed in a modified Griggs-type solid-medium apparatus [*Rybacki et al.*, 1998]. Three media served as confining pressure medium, the eutectic mixture of CsCl-NaCl (34.5 mol% NaCl and 65.5 mol% CsCl) for experiments at $T \leq 1000^\circ\text{C}$ and $P \leq 2.5$ GPa, NaCl for experiments at $T > 1000^\circ\text{C}$ and $P = 0.75$ to 2.7 GPa,

and KCl for two experiments (omph63, omph57) at $T > 1000^{\circ}\text{C}$ and $P = 2.5$ GPa. At 2.5 GPa, the nominal confining pressure of most deformation tests, the melting temperature of CsCl-NaCl mixture is about 1000°C [Kim *et al.*, 1972]. Two NiCr-Ni thermocouples were used for controlling and measuring of the temperature at the lower and upper sample ends, respectively; a graphite furnace provided heating (Figure 11).

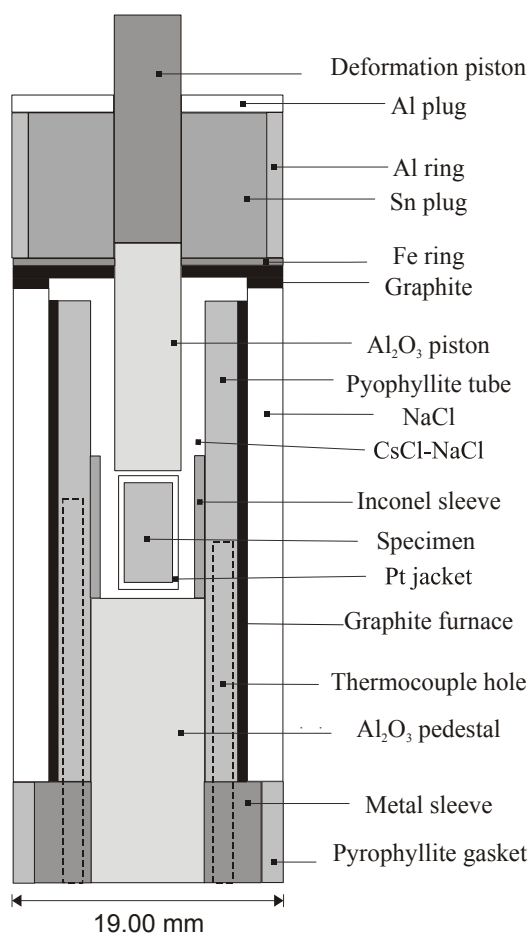


Figure 11: Sketch of the sample assembly used for deformation tests.

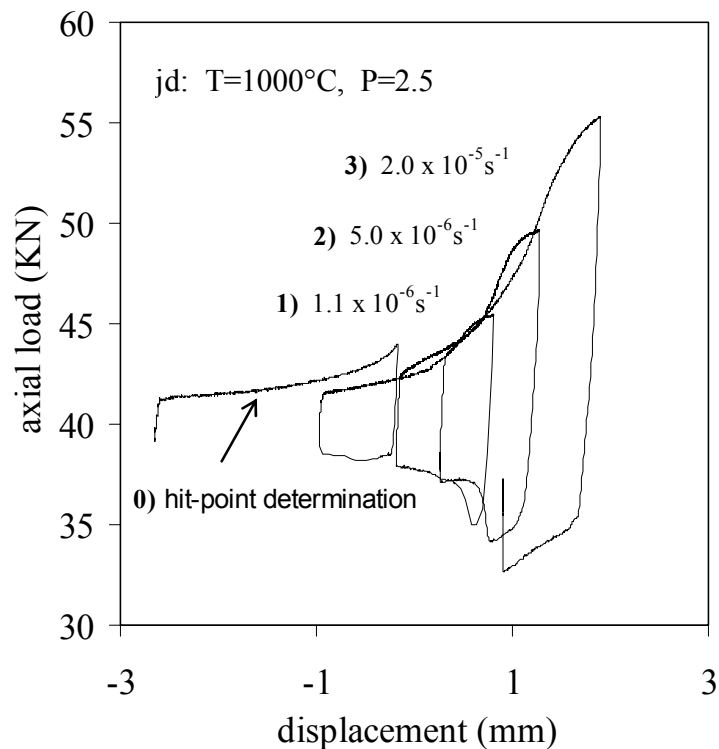


Figure 12: Axial load-displacement record of a strain-rate stepping experiment performed on a jadeite sample (omph18, Table 5) at a nominal confining pressure of 2.5 GPa and a temperature of about 1000°C at indicated strain rates.

Pressure and temperature were raised with 14 MPa/min and 5°C/min, respectively, to avoid damage of the graphite furnace and to minimize pressure gradients within the assembly. The axial piston was periodically advanced into the assembly until reaching final condition. At run conditions, the hit point was first determined by advancing the deformation piston at a velocity of 1 mm/hour. Subsequently, the deformation piston was withdrawn for approximately 1 mm before its direction of movement was reversed again for the actual deformation stage at specified strain rate. In several experiments, this procedure was repeated up to three times to explore the effect of strain rate (Figure 12). At the end of the final deformation stage, the piston was retracted for at least 1 mm from the sample, before pressure and temperature were decreased with rates of 83 MPa/min and ~30°C/min, respectively.

3.3.2. Derivation of stress-strain curves

Stress-strain curves were derived from the recorded forces and displacements assuming constant sample volume, correcting for friction and for stiffness of the axial load column. Strain was calculated from the displacement of deformation piston after hit point and the initial length of a sample at room temperature or after considering previous shortening in strain rate stepping tests. Nominal uncertainty in strain is on the order of 0.1% accounting for the accuracy of the displacement transducer and uncertainty in stiffness correction. The uncertainty in reported strain rates of a factor of ~ 1.1 results mostly from the uncertainty in current sample length. The nominal uncertainty in the derived stress is estimated to 20 MPa considering a load cell accuracy of 0.02% over its range of 160 kN and an uncertainty in the sample diameter of 0.1 mm. However, a significant methodological uncertainty for stress arises from the determination of the contribution of friction to the external load cell reading [Renner *et al.*, 2001; Rybacki *et al.*, 1998]. Here, we applied a dynamic correction, i.e., the approximately linear portion of the axial load-displacement curves prior to a hit point served

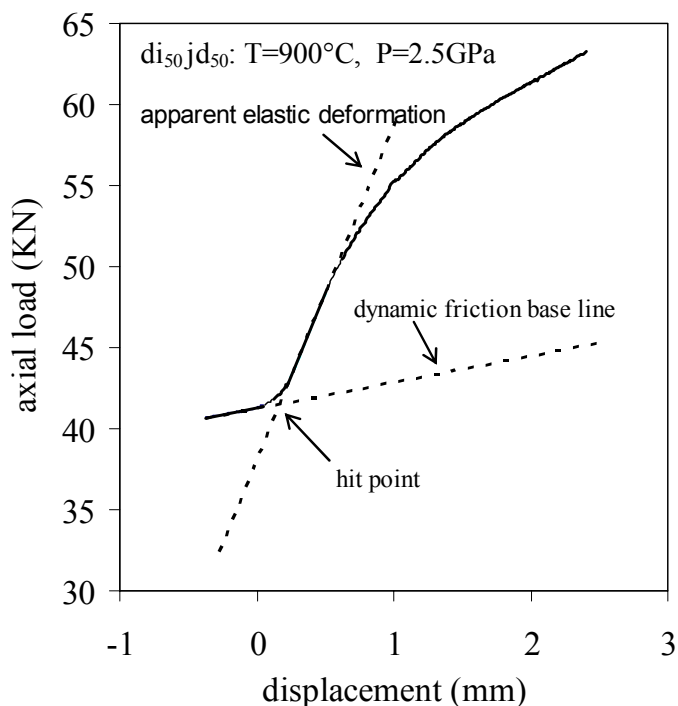


Figure 13: Processing of the axial load-displacement curves involved a dynamic friction correction as here exemplified for a $di_{50}jd_{50}$ -sample deformed at a temperature of 900°C and a strain rate of $2 \times 10^{-5} \text{ s}^{-1}$.

as friction baseline (Figure 13). A major source of uncertainty is the friction on the alumina piston on top of samples (Figure 11). The total friction is measured by the external load cell only when the tungsten carbide piston and the alumina piston, which are glued to each other before an experiment, actually stay in contact during the entire experiment. In case the alumina piston rests on top of the sample during piston retraction because tin penetrates between the tungsten carbide piston and the alumina piston rather than salt between the alumina piston and the sample, stress on the sample is overestimated by the friction on the alumina piston in subsequent deformation cycles. The magnitude of overestimation depends on experimental conditions: the higher the temperature and the less the piston velocity the less the viscous friction on the alumina piston. Uncertainty associated with the extrapolation of the friction baseline, the variability of the baseline from

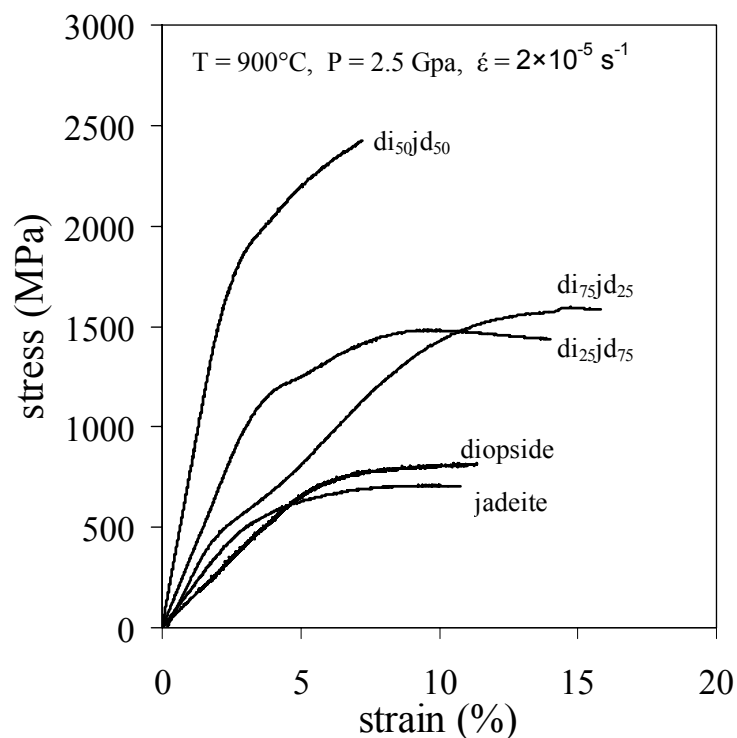


Figure 14: Stress-strain curves for omphacite samples of indicated compositions deformed at a temperature of 900°C, a confining pressure of 2.5 GPa, and a strain rate of $2 \times 10^{-5} \text{ s}^{-1}$. The strength of intermediate compositions exceeds the strength of the compositional endmembers, jadeite and diopside.

test to test, and the state of the alumina piston all add up to an uncertainty of 50 to 100 MPa and therefore hinder a reliable determination of differential stress below about 100 MPa. Actual pressure may be lower than the nominal pressure by about 10% and actual temperature is within about 20°C of the readings of the two thermocouples [see *Rybacki et al.*, 1998]. The thermocouple readings were not corrected for the effect of pressure on electromotive force (e.m.f.).

4. Results of deformation experiments

4.1. Synthetic aggregates

4.1.1. Mechanical data

A number of 32 experiments were deformed at temperatures between 900 and 1100°C, a confining pressure of 2.5 GPa, and constant strain rates between 1.1×10^{-6} and $8.5 \times 10^{-5} \text{ s}^{-1}$ (Table 5). A total of 24 tests were conducted at a single set of conditions to allow for an unequivocal correlation of the mechanical data and the microstructure of the deformed sample. In 8 step tests, a sample was axially loaded up to three times at different strain rates. To investigate the effect of pressure on deformation mechanisms, 4 experiments were performed on synthetic diopside aggregates at a pressure <2.5 GPa (Table 6). For diopside samples, the range in pressure at which experiments can be performed is the largest of all omphacites due to their stability down to ambient pressure (Figure 2). This series of tests also provided a chance for comparison of results with previously published data collected in low-pressure gas-medium apparatus. The force-displacement curves for all experiments are attached in appendix A. Typical examples of force versus displacement curves and of the derived stress versus strain curves are presented in Figures (12), (13) and (14). While not all samples exhibit plastic deformation at constant stress, a systematic relation between experimental conditions and apparent softening or hardening behavior was not found indicating uncertainties in friction correction as the cause rather than actual material behavior. Indeed, the vast majority of samples are homogeneously shortened and thickened after deformation. The reported flow stresses (Table 5), simply referred to as strength in the following, are those attained at apparent mechanical steady state or, if steady state was not achieved, the maximum stresses. The reproducibility of mechanical data obtained in tests at similar conditions on different samples is on the order of $\pm 10\%$ (see Table 5).

For all compositions, strength systematically decreases with increasing temperature and decreasing strain rate as expected for thermally activated plastic deformation processes. The effect of composition on relative strength, however, evolves with increasing temperature. At the lowest investigated temperature of 900°C, intermediate compositions are clearly stronger than either compositional endmember of which jadeite is systematically

the weaker one. At 1100°C, we find a rather monotonous decrease in strength from diopside to jadeite aggregates.

Best-fit parameters of a power law relation

$$\dot{\varepsilon} = A \cdot \sigma^{n'} \cdot \exp\left(-\frac{Q}{RT}\right) \quad (1)$$

were determined for the gained mechanical data using a non-linear inversion method [Sotin and Poirier, 1984] that accounts for the reported uncertainties in experimental data, strain rate $\dot{\varepsilon}$, stress difference σ , and absolute temperature T (Table 5). Here, A , n' , Q , and R denote the pre-exponential factor, the stress exponent, the apparent activation energy of creep, and the universal gas constant, respectively. Determined stress exponents vary between ~ 3 and ~ 10 ; to first order we observe an increase from sodic to calcic composition (Table 7, Figure 15). Apparent activation energies for creep vary between >200 and <600 kJ/mol. A clear relation to composition is not found, in fact a uniform value of ~ 350 kJ/mol lies within the uncertainty range of all compositions.

In cases, the difference between axial strain determined from sample dimensions after quenching and permanent strain calculated from the displacement transducer exceeds $\delta\varepsilon = \pm 5\%$, the maximum uncertainty in recorded strain due to uncertain hit-point determination (Table 5). Deformed samples often show quench cracks. Quench cracks increase sample length causing the permanent axial strain to fall short of the recorded strain. Samples that are shorter than the estimated recorded strain likely experienced non-hydrostatic quenching and are therefore excluded from the microstructure analyses.

composition	sample	temperature (°C)	strain rate (1/s)	stress (MPa)	strain (%)		micro-analysis	grain size (µm)	melt content (%)
					rec.	total			
jd	Omph57	1108 ± 8	4.8 x 10 ⁻⁶	50	20.1	16.8	SEM,EBSD	7.5 ± 3.0 ^a	<4
	Omph16	1013 ± 13	1.1 x 10 ⁻⁶	182	11.2		SEM,EBSD	5.2 ± 4.0	<2
		1010 ± 10	5.0 x 10 ⁻⁶	296	12.1				
		1012 ± 12	2.0 x 10 ⁻⁵	435	11.0				
	Omph18	1018 ± 18	1.1 x 10 ⁻⁶	227	14.2		SEM,EBSD	9.3 ± 4.4	<2
		1020 ± 20	5.0 x 10 ⁻⁶	325	14.1				
		1015 ± 15	2.0 x 10 ⁻⁵	432	15.0				
	Omph54	1080 ± 20	2.0 x 10 ⁻⁵	100	12.1				
	Omph10	908 ± 8	3.0 x 10 ⁻⁶	399	9.2				
		908 ± 8	1.5 x 10 ⁻⁵	704	10.8				
907 ± 7		7.5 x 10 ⁻⁵	1037	12.1					
di ₂₅ jd ₇₅	Omph25	908 ± 8	1.6 x 10 ⁻⁵	1481	14.0	32.0	SEM	5 ^b	<4
	Omph14	1012 ± 12	5.0 x 10 ⁻⁶	305	6.5	19.1	SEM,EBSD	3.3 ± 1.2	
		1009 ± 9	8.5 x 10 ⁻⁵	1203	3.1				
	Omph17	998 ± 2	1.1 x 10 ⁻⁶	265	8.1	15.0	SEM,EBSD	2.1 ± 1.2	<2
	Omph51	982 ± 18	2.0 x 10 ⁻⁵	590	27.6				
	Omph59	1117 ± 17	5.2 x 10 ⁻⁶	293	15.1				
di ₅₀ jd ₅₀	Omph52	1100 ± 1	4.9 x 10 ⁻⁶	501	7.3	2.3	SEM	9	
	Omph22	912 ± 12	1.1 x 10 ⁻⁶	1280	23.2	31.4	SEM,EBSD,TEM	7.3 ± 4.7	
	Omph11	900	3.0 x 10 ⁻⁶	1356	6.1				
		900	1.5 x 10 ⁻⁵	2445	7.3				
		900	7.5 x 10 ⁻⁵	2700	8.2				
	Omph12	1004 ± 4	5.0 x 10 ⁻⁶	416	4.2				
		1003 ± 3	2.0 x 10 ⁻⁵	1024	11.6				
		1003 ± 3	8.5 x 10 ⁻⁵	1741	6.1				
	Omph30	1105 ± 5	1.1 x 10 ⁻⁶	410	18.8				
	di ₇₅ jd ₂₅	Omph28	887 ± 13	4.8 x 10 ⁻⁶	1534	11.3	3.1	SEM,EBSD,TEM	10.0 ± 6.0
Omph19		1109 ± 9	1.1 x 10 ⁻⁶	450	8.1	13.0	SEM,EBSD,TEM	10.1 ± 6.1	
		1114 ± 14	5.2 x 10 ⁻⁶	632	14.0				
Omph21		912 ± 12	1.1 x 10 ⁻⁶	1450	18.0	20.0	SEM,EBSD	8.4 ± 4.8	
Omph09		907 ± 7	3.0 x 10 ⁻⁶	1588	16.1				
		907 ± 7	1.5 x 10 ⁻⁵	2024	8.2				
Omph29	995 ± 5	5.0 x 10 ⁻⁶	818	11.3					
di	Omph32	905 ± 5	3.8 x 10 ⁻⁶	1601	22.8	25.8	SEM,EBSD	5.0 ± 4.0	
	Omph38	990 ± 10	4.6 x 10 ⁻⁶	867	30.6	27.7	SEM,EBSD	7.5 ± 4.0	
	Omph47	1069 ± 31	4.8 x 10 ⁻⁶	544	20.1	18.8	SEM,EBSD,TEM	11.0 ± 7.0	
	Omph50	993 ± 7	2.0 x 10 ⁻⁵	1088	26.2	20.1	SEM,EBSD	8.7 ± 5.4	
	Omph53	882 ± 18	3.0 x 10 ⁻⁶	1060	22.1	6.8	SEM	11	
	Omph61	902 ± 2	7.9 x 10 ⁻⁵	1647	15.6	0.2	SEM	11	
	Omph62	1127 ± 27	2.0 x 10 ⁻⁵	497	12.6	13.9	SEM	11	
	Omph08	890 ± 10	1.5 x 10 ⁻⁵	1217	10.5				
	Omph15	925 ± 25	1.1 x 10 ⁻⁶	1091	10.3				
	Omph27	910 ± 10	7.9 x 10 ⁻⁵	1487	11.7				
	Omph26	980 ± 20	5.0 x 10 ⁻⁶	853	6.3				
	Omph63	1092 ± 8	2.0 x 10 ⁻⁵	672	14.1				

Table 5: Experimental conditions and results for the deformation experiments on the synthetic polycrystalline omphacite aggregates at a nominal confining pressure of 2.5 GPa. The reported temperature is the average of the upper and lower thermocouple. In the test on sample omph11 the upper thermocouple failed. Grain sizes are based on automated EBSD measurements (a: quoted as average \pm standard deviation) or line intercept determinations on SEM images (b). Melt content was estimated from SEM images. Axial strain is reported as derived from the recorded force-displacement curves (rec.) and from length measurements on samples recovered after quenching to ambient conditions (total).

sample	pressure (GPa)	temperature (°C)	strain rate (1/s)	stress (MPa)	strain (%)	
					recorded	total
omph43	2.0	975 \pm 25	5.0 $\times 10^{-6}$	822	22.0	24.2
omph49	1.5	987 \pm 13	5.0 $\times 10^{-6}$	725	27.8	29.3
omph55	0.75	1003 \pm 3	5.0 $\times 10^{-6}$	620	11.7	20.3
		1003 \pm 3	2.0 $\times 10^{-5}$	883	16.5	
omph64	1.8	1055 \pm 45	5.2 $\times 10^{-6}$	750	8.4	13.5
		1046 \pm 54	2.0 $\times 10^{-5}$	1152	8.1	

Table 6: Experimental conditions and results for the deformation experiments on the synthetic polycrystalline diopside aggregates at quoted confining pressures < 2.5 GPa.

composition	$\ln(A \text{ [MPa}^{-n} \text{s}^{-1}])$	n' [-]	Q [kJ/mol]
di	-29.6 \pm 4.8	8.1 \pm 1.5	391 \pm 79
di ₇₅ jd ₂₅	-10.3 \pm 3.2	5.5 \pm 1.9	414 \pm 136
di ₅₀ jd ₅₀	-4.7 \pm 1.1	3.5 \pm 0.2	323 \pm 18
di ₂₅ jd ₇₅	4.3 \pm 3.6	3.0 \pm 0.5	281 \pm 63
jd	3.5 \pm 6.3	4.2 \pm 0.8	413 \pm 79

Table 7: Parameters of a power law (1) fit to the data reported in table (5).

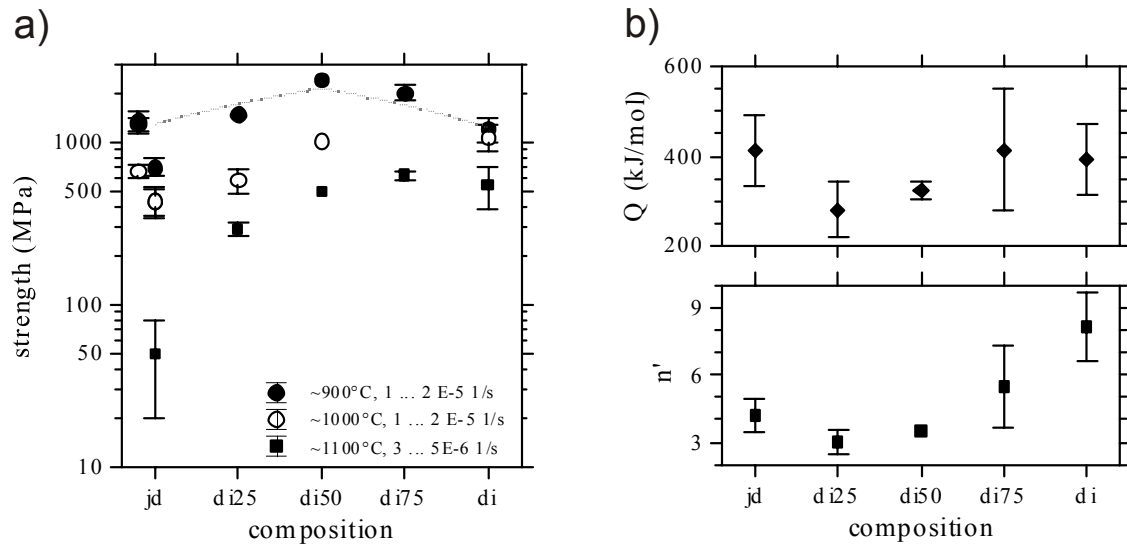


Figure 15: a) Variation of measured strength with composition at indicated temperatures and strain rates. The dotted lines represent the relations between strength and composition when relying on scaling with melting temperature (increase for sodic compositions) and shear modulus (decrease for calcic compositions). Flow stress determined for synthetic jadeite aggregates by *Orzol et al.* [2006] is given for comparison (shifted slightly to the left for presentational purposes). b) Relation between sample composition and apparent activation energy for creep, Q (top), and apparent stress exponent, n' (bottom), gained from fitting a power law (1) to the data reported in table (5).

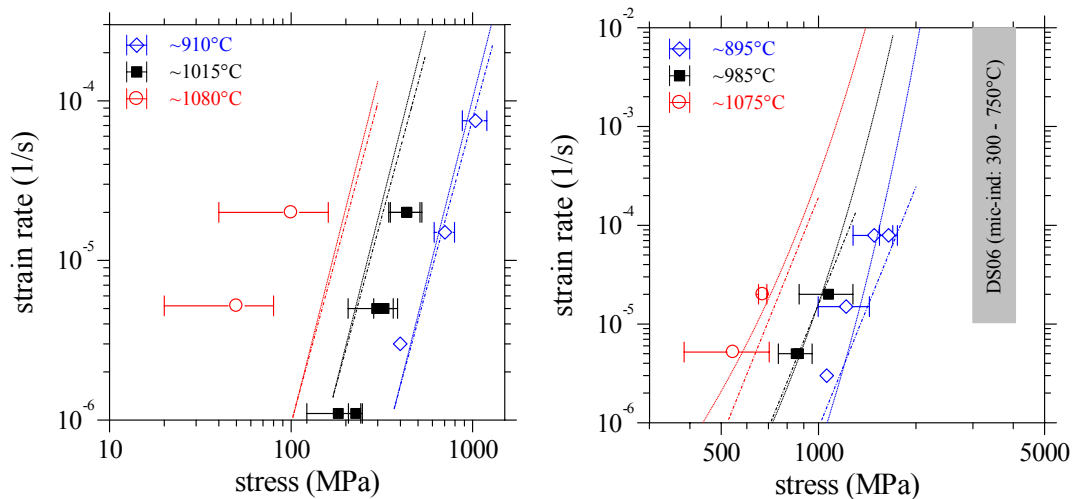


Figure 16: Relation between stress and strain rate for jadeite (up) and diopside (down) aggregates. Error bars represent variation of temperature in the vicinity of sample that measured during experiments by upper thermocouples and uncertainty in friction base line and sample dimensions. Note, the two experiments on jadeite aggregates with nominal flow stresses below 100 MPa fall below the methodological uncertainty.

4.1.2. Microstructures

Grain size of deformed samples shortened by a maximum of 30% does not differ significantly from the grain size of undeformed samples (Table 5). However, intracrystalline deformation is documented in deformed samples by microtwins, undulatory extinction and subgrain boundaries (Figure 17, Figure 18, Figure 19). The density of twins systematically decreases from diopside to jadeite composition. While almost all grains are twinned in diopside samples, twins are even absent in jadeite samples deformed above 900°C. The twins can be resolved by OC and TEM investigations because their spacing and width is typically less than 0.5 μm (Figure 18, Figure 19). They can also be observed in the optical microscopy images (Figure 17). Based on these size characteristics they qualify as microtwins. EBSD measurements showed that they are of the (100) [001] type [Kirby and Christie, 1977]. In cases, twins are wedge-shaped and terminate within grains (Figure 19e). Furthermore, twin lamellae are slightly curved in grains of high defect density (Figure 19b). Zones of high dislocation density coincide with twin lamellae in places (Figure 19a-c). Some dislocations in untwinned areas are curved and tangled (Figure 19a,f). The grain boundaries of twinned grains exhibit peculiar steps of varying step lengths (Figure 19c). The occurrence of subgrain boundaries correlates inversely with twin density and thus with composition. Jadeite samples exhibit the most pronounced subgrains with a size of 1 to 10 μm (Figure 18) whereas this microstructural feature becomes less prominent with increasing calcic component. In contrast to the starting material (Figure 5), deformed samples show a more pronounced lineation (Figure 20). Rather independent of composition axis-parallel sections of deformed samples, show a (SPO) with the long axis of grains oriented preferentially perpendicular to the shortening direction in particular for the grains larger than 10 μm (Figure 20). In addition, samples of sodic composition exhibit a significant (CPO) of the poles to (100) and (010) planes parallel to the shortening direction and the [001] direction perpendicular to the shortening direction (Figure 20). CPO in samples with the most calcic composition is notably weaker than in the sodic samples when deformed to similar strains.

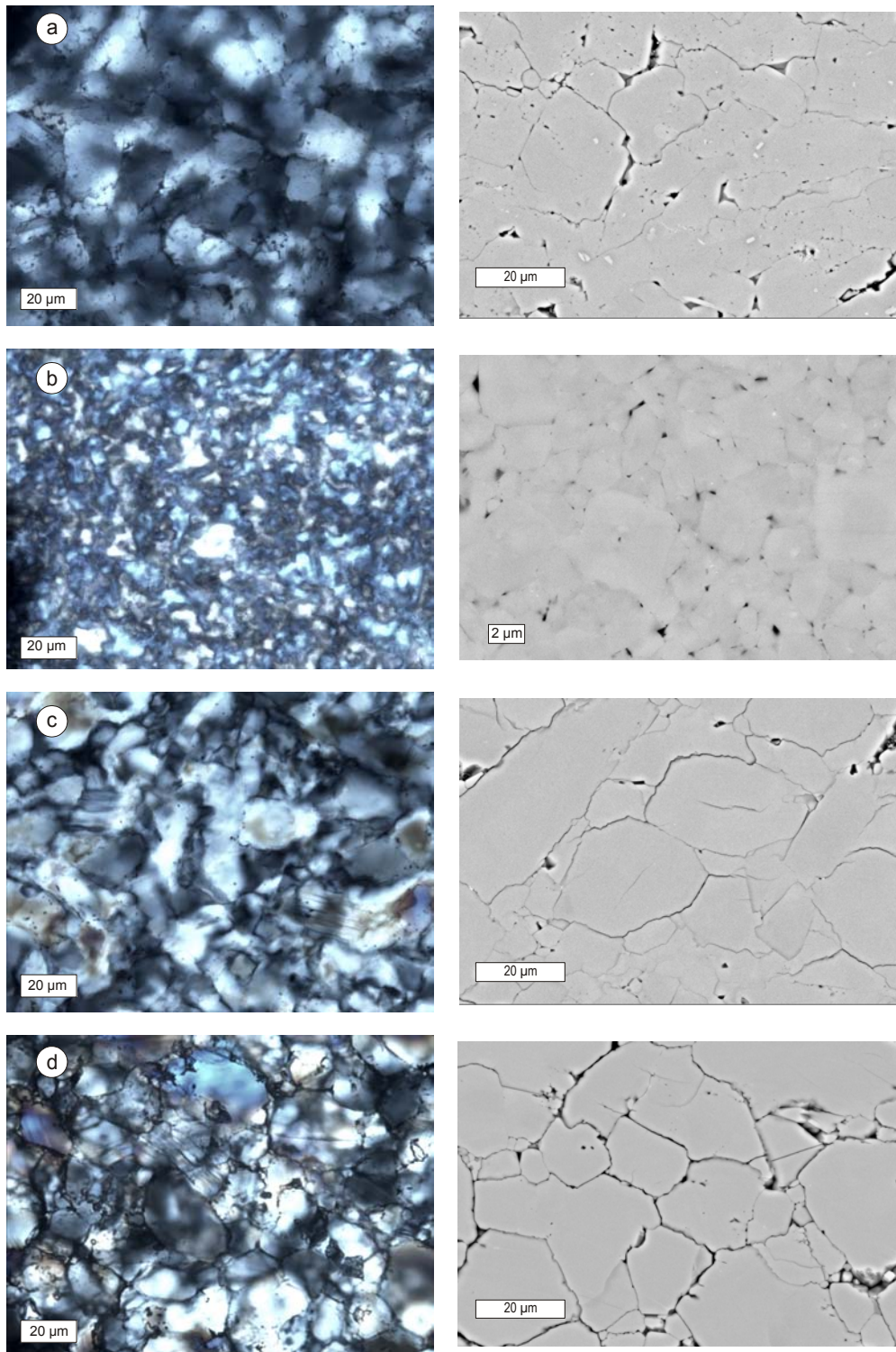


Figure 17: Photomicrograph (left) and BSE images (right) of deformed samples; a) jadeite (omph18) $T = 1012^{\circ}\text{C}$, $\sigma_d = 432 \text{ MPa}$, $\epsilon = 30\%$; b) 25%di (omph17), $T = 998^{\circ}\text{C}$, $\sigma_d = 265 \text{ MPa}$, $\epsilon = 15\%$; c) 75%di (omph19) at 1114°C , $\sigma_d = 632 \text{ MPa}$, $\epsilon = 14\%$; d) diopside (omph47) $T = 1069^{\circ}\text{C}$, $\sigma_d = \text{MPa}$, $\epsilon = 20\%$. Grain boundaries are commonly sutured.

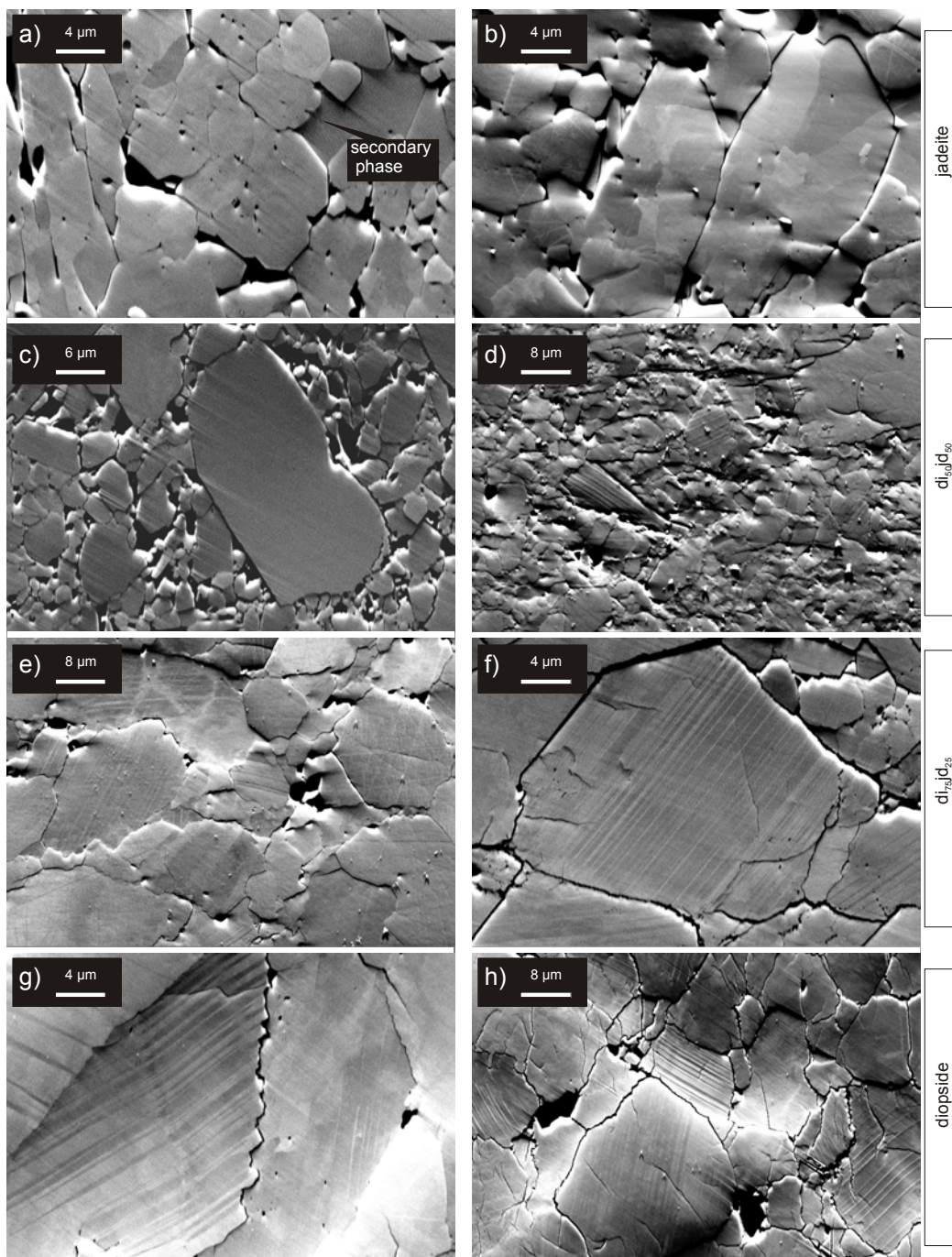


Figure 18: OC-images of deformed samples; jadeite samples deformed at a) 1108°C (omph57) and b) 1010°C (omph16); $di_{50}jd_{50}$ samples deformed at a) 1100°C (omph52) and d) 912°C (omph22); $di_{75}jd_{25}$ samples deformed at a) 1114°C (omph19) and f) 887°C (omph28); diopside samples deformed at g) 993°C (omph50) and h) 882°C (omph53). The confining pressure during deformation of all samples was 2.5 GPa (for details see Table 3). Subgrains are widespread in jadeite (a,b), whereas mechanical twins tend to be more frequent in diopside-rich compositions (e-h). High-angle grain boundaries between grains of low twin density and grains with a high twin density are strongly sutured (g). The secondary phase inside the jadeite aggregate extended well at high temperature.

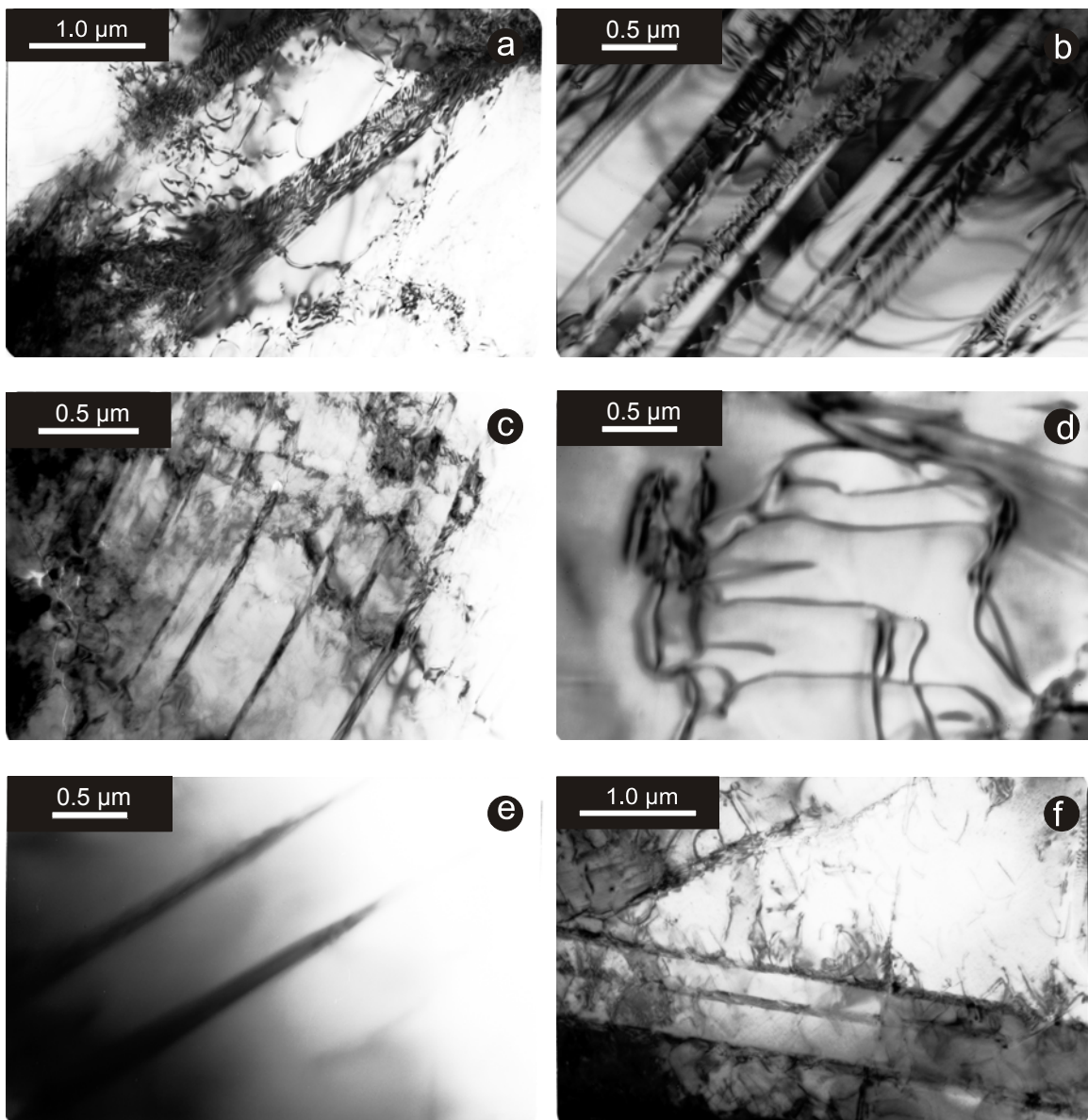


Figure 19: TEM-bright field micrographs of deformed omphacite. a-d) $di_{75}jd_{25}$ sample exhibits zones of high defect density that can coincide with twin lamellae. In a) and b) twin lamellae can be slightly curved and occur in a grain of high defect density. d) exhibits curved dislocations. e, f) diopside sample exhibits wedge shape of twins (e) and slightly curved twin lamellae in a grain of high defect density (c).

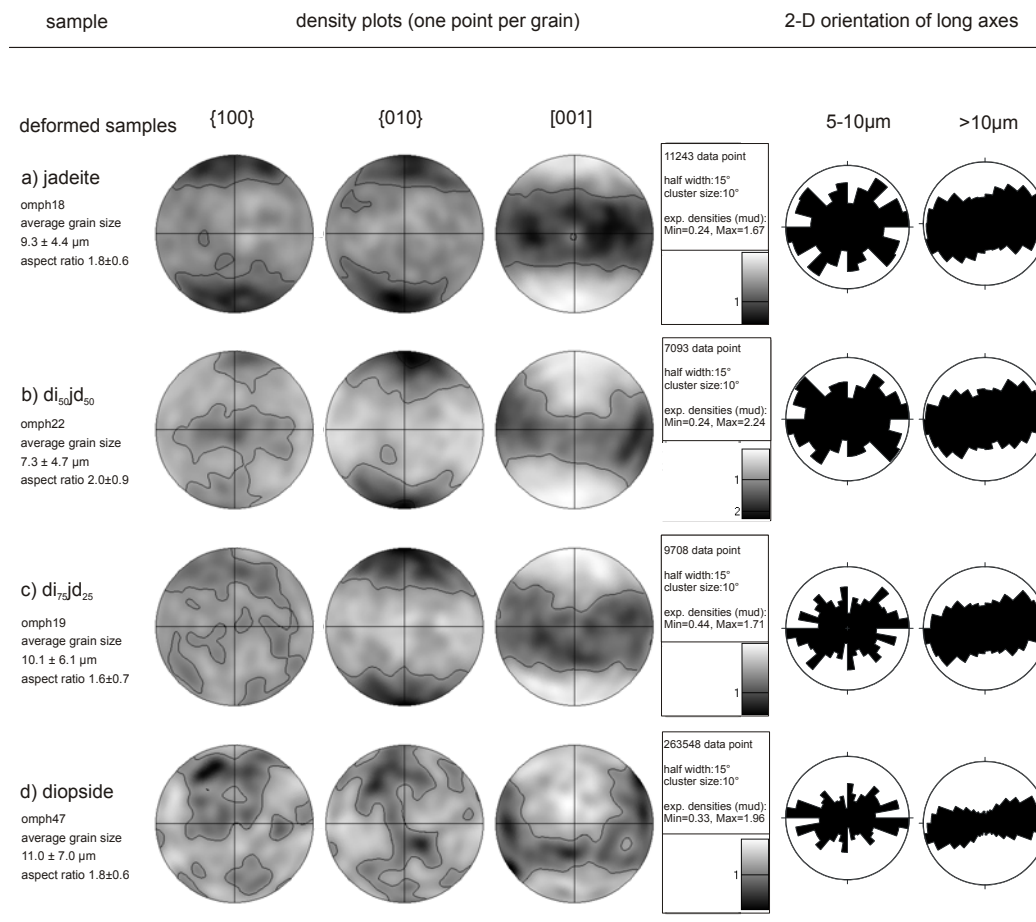


Figure 20: Selected automated EBSD measurements (2 μm step size) deformed samples. Left: density plots (equal area projection of the lower hemisphere) are displayed for the poles to {100} and {010} planes and the [001] direction. Deformed samples were cut parallel to the axial load direction. Right: 2-D orientation of long axes of grains with diameters <10 μm and >10 μm are displayed in a rose diagram.

4.2. Natural clinopyroxene samples

4.2.1. Mechanical data

Deformation experiments were performed on 7 natural clinopyroxene samples at temperatures between 800 and 1170°C, confining pressures between 1.5 and 2.7 GPa, and constant strain rates between 1.1×10^{-6} and $2.0 \times 10^{-5} \text{ s}^{-1}$. A total of 3 tests were conducted at a single set of conditions to allow for an unequivocal correlation of the mechanical data and the microstructure of the deformed sample. In 4 step tests, a sample was axially loaded

up to three times at different strain rates. The force-displacement curves for deformation experiments on natural clinopyroxene samples are attached in appendix B. The reproducibility of mechanical data obtained in tests at similar conditions is good (see Table 8). This series of tests provides a chance for a comparison with previously published data on natural Sleaford Bay clinopyroxenite and thereby for an investigation of the effects of pressure and Fe-content on strength of calcic pyroxenite samples.

The reported flow stresses for natural clinopyroxene samples (Table 8), referred to as strength in the following, give stresses at apparent mechanical steady state or, if steady state was not achieved, the maximum stresses. For all experiments, strength systematically decreases with increasing temperature and decreasing strain rate. For experiments at ~900°C, strength increases with an increase in confining pressure from 1.5 GPa to 2.5 GPa (Table 8).

Sample	Pressure (GPa)	Temperature (°C)	Strain rate (1/s)	Stress (MPa)	Strain (%)	
					recorded	total
c1		890 ± 10	4.9 × 10 ⁻⁶	1001	24	14
c4	2.5	904 ± 4	1.45 × 10 ⁻⁶	681	11	16
		903 ± 3	4.85 × 10 ⁻⁶	1046	12	
		902 ± 2	1.00 × 10 ⁻⁵	1362	8	
c3		1092 ± 8	4.9 × 10 ⁻⁶	415	25	20
c6		1088 ± 12	1.13 × 10 ⁻⁶	200	6.7	6.7
		1087 ± 13	4.91 × 10 ⁻⁶	407	4.6	
		1086 ± 14	2.00 × 10 ⁻⁵	538	7.1	
c2	1.5	897 ± 3	5.00 × 10 ⁻⁶	830	24	19
c8		789 ± 11	1.14 × 10 ⁻⁶	1052	11.3	15
		789 ± 11	4.92 × 10 ⁻⁶	1398	15.2	
c7	2.7	1170 ± 5	1.10 × 10 ⁻⁶	107	4.5	10
		1148 ± 27	5.00 × 10 ⁻⁶	232	8.7	
		1160 ± 15	2.00 × 10 ⁻⁵	340	25	

Table 8: Experimental conditions and results for the deformation experiments on the natural clinopyroxenite samples.

composition	$\ln(A \text{ [MPa}^{-n} \text{s}^{-1}])$	n' [-]	Q [kJ/mol]
Sleaford Bay cpx	-8.1±1.8	2.8±0.4	231±35

Table 9: Parameters of a power law (1) fit to the data for Sleaford Bay clinopyroxenite samples deformed at 2.5 GPa and 2.7 GPa confining pressures.

The parameters of a power law relation (eq.1) were determined using a non-linear inversion method [Sotin and Poirier, 1984] for mechanical data of natural clinopyroxene samples (Table 8). These flow parameters are constrained restricting to the mechanical data gathered at 2.5 and 2.7 GPa confining pressure.

4.2.2. Microstructures

As in the synthetic omphacite aggregates, significant changes in grain size are not observed for the deformed natural clinopyroxenes after a maximum of 25% shortening (Figure 21, Figure 22). However, intracrystalline deformation is documented in deformed samples by microtwins, undulatory extinction and subgrain boundaries, too (Figure 21, Figure 22). Twinning and microcracking are the predominant features in all deformed samples. At high temperatures ($T > 1100^\circ\text{C}$), subgrain boundaries are well developed and small new grains are found in the vicinity of the boundaries of the “old” grains (Figure 21, Figure 22b,d). The development of subgrain boundaries correlates inversely with twin density in the vicinity of grain boundaries in high temperature experiments (Figure 21, Figure 22). Twin lamellae are slightly curved in low temperature ($T \leq 900^\circ\text{C}$) experiments (Figure 21c). The grain boundaries of twinned grains sutured (Figure 22c). The microcracks occur generally perpendicular to cylinder axes (e.g. Figure 22b) thus they are interpreted to result from quenching.

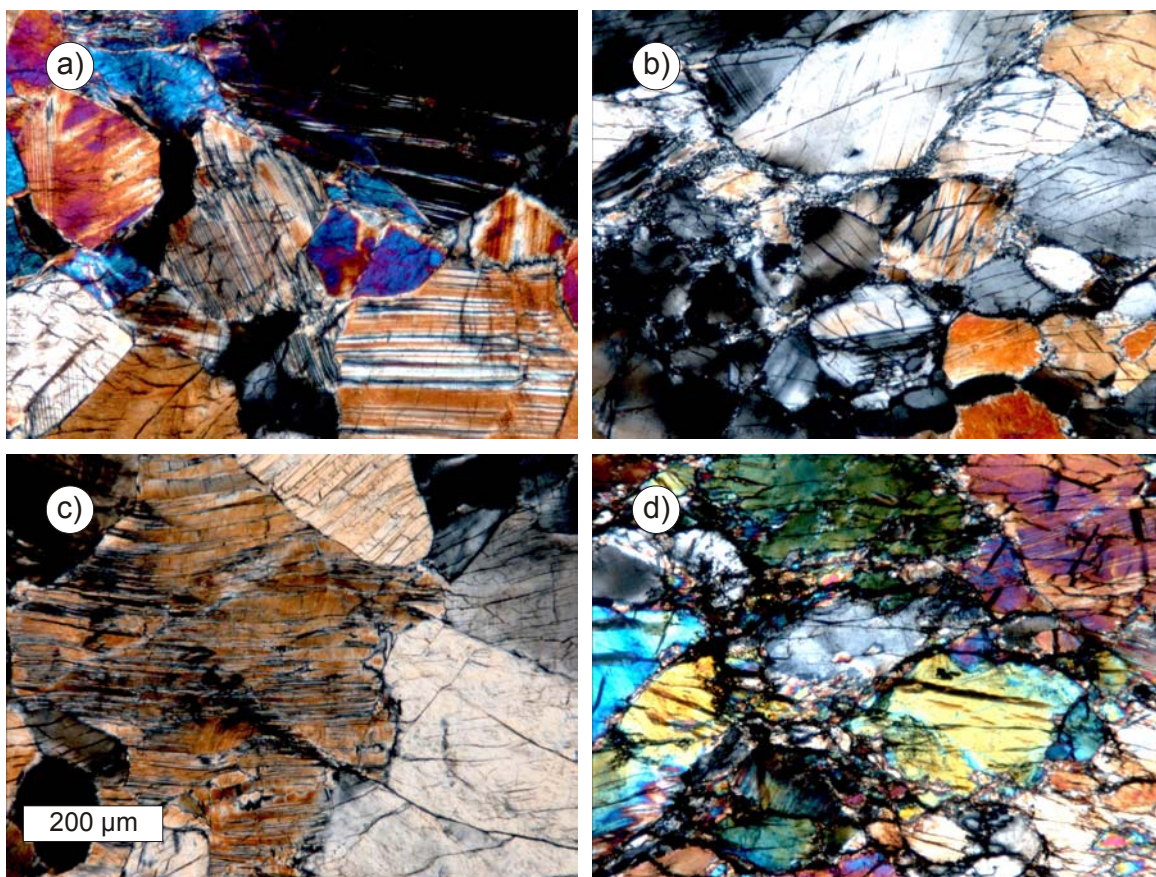


Figure 21: Optical micrographs of deformed clinopyroxene samples. a) c2 at $P = 1.5$ GPa, $T = 897^{\circ}\text{C}$, b) c3 at $P = 2.5$ GPa, $T = 1092^{\circ}\text{C}$, c) c4 at $P = 2.5$ GPa, $T = 903^{\circ}\text{C}$, d) c7 at $P = 2.7$ GPa, $T = 1170^{\circ}\text{C}$ (see table 8 for deformation conditions). The scale bar applies to all images. The direction of axial loading is perpendicular to the long axes of the images.

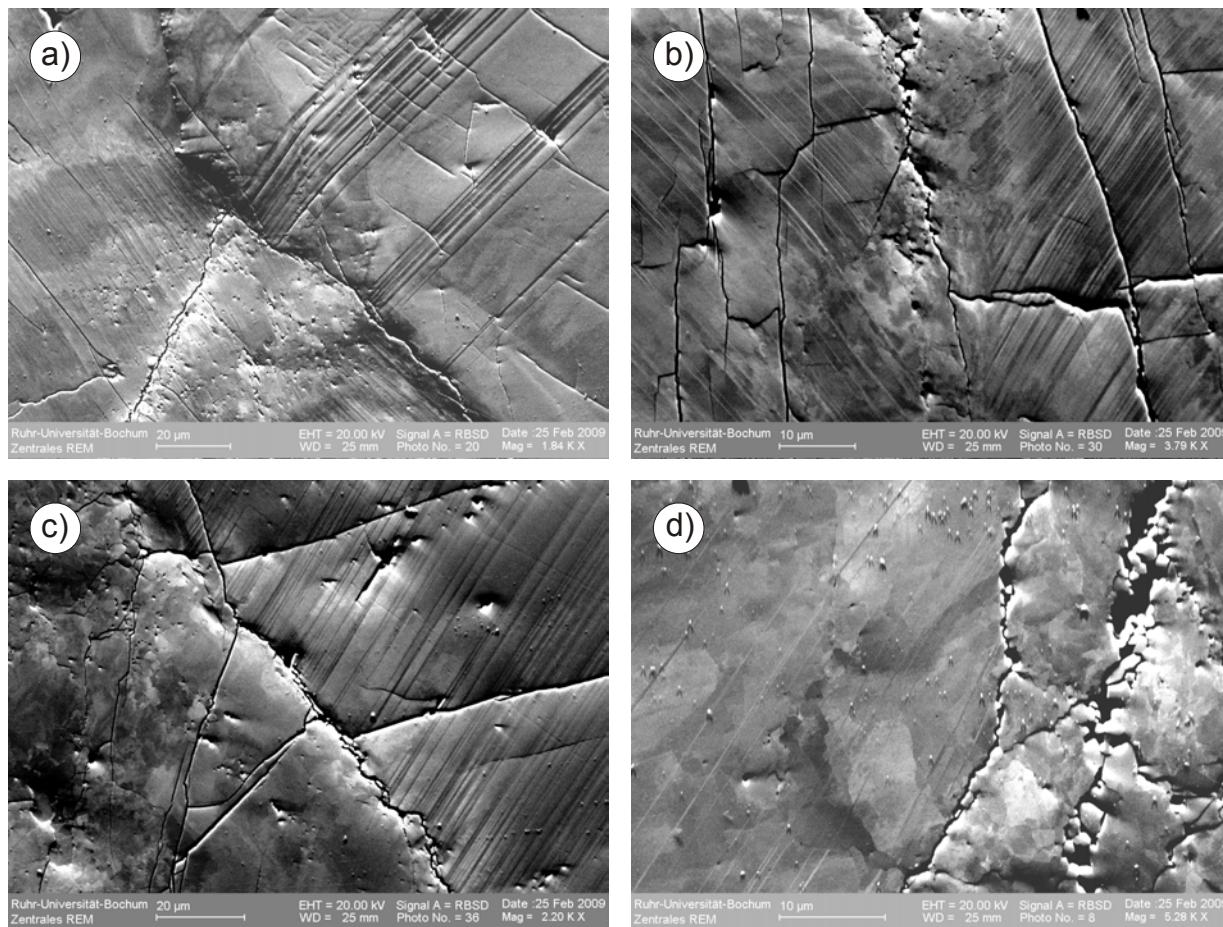


Figure 22: OC-images of deformed clinopyroxene samples a) c2 at $P = 1.5$ GPa, $T = 897^{\circ}\text{C}$, b) c3 at $P = 2.5$ GPa, $T = 1092^{\circ}\text{C}$, c) c4 at $P = 2.5$ GPa, $T = 903^{\circ}\text{C}$, d) c7 at $P = 2.7$ GPa, $T = 1170^{\circ}\text{C}$ (see table 8 for deformation conditions). Samples deformed at $T > 1100^{\circ}$ exhibit well developed subgrain boundaries (b, d). The direction of axial loading is perpendicular to the long axes of the images.

4.3. Hydrogen content of deformed samples

The FTIR spectra of deformed synthetic jadeite and diopside aggregates are similar to the ones of undeformed samples indicating that the hydrogen speciation is not significantly affected by the deformation processes (see Figure 10 and Figure 24), but water content of synthetic deformed samples is generally higher than the undeformed ones. In contrast to the synthetic omphacite aggregates, the water content of undeformed clinopyroxene samples is significantly lower than that of deformed samples (Figure 23). The water content of deformed natural clinopyroxene samples at high temperature ($>1100^{\circ}\text{C}$) experiments is lower than at low temperature ($\leq 1000^{\circ}\text{C}$) experiments. There is no systematic relation

between hydroxyl content and pressure in deformed natural clinopyroxene samples (Figure 23). The water content of deformed synthetic diopside aggregates and deformed natural Fe-bearing clinopyroxene samples at low temperature ($\leq 1000^\circ\text{C}$) is fairly similar (Figure 23), suggesting a weak effect of Fe-content on hydrogen incorporation in deformed samples.

composition	sample	water/hydrogen content			temperature ($^\circ\text{C}$)	pressure (GPa)
		(mol $\text{H}_2\text{O}/\text{l}$)	(ppm H_2O)	($\text{H}/10^6 \text{ Si}$)		
jd	omph57-1	0.551	3005	38163	1108	2.5
	omph57-2	0.491	2678	34010	1108	2.5
$\text{di}_{50}\text{jd}_{50}$	omph52-1	0.0657	358	4546	1100	2.5
	omph52-2	0.0644	351	4457	1100	2.5
di	omph62-1	0.129	704	8940	1127	2.5
	omph53-1	0.178	971	12331	882	2.5
	omph53-2	0.161	878	11150	882	2.5
	Omph61-1	0.256	1396	17729	902	2.5
	Omph61-2	0.242	1319	16751	902	2.5
	Omph55-1	0.154	839	10655	1003	0.75
	Omph55-2	0.148	807	10248	1003	0.75

Table 10: Hydrogen/water content of synthetic omphacite aggregates deformed at given temperature and pressure. The water content by weight is calculated using 3.3 g/cm^3 as the average density of samples. The bulk hydrogen content was estimated from FTIR spectra according to the method outlined by *Paterson* [1982]. Reported values are based on the analysis of a single FTIR spectrum.

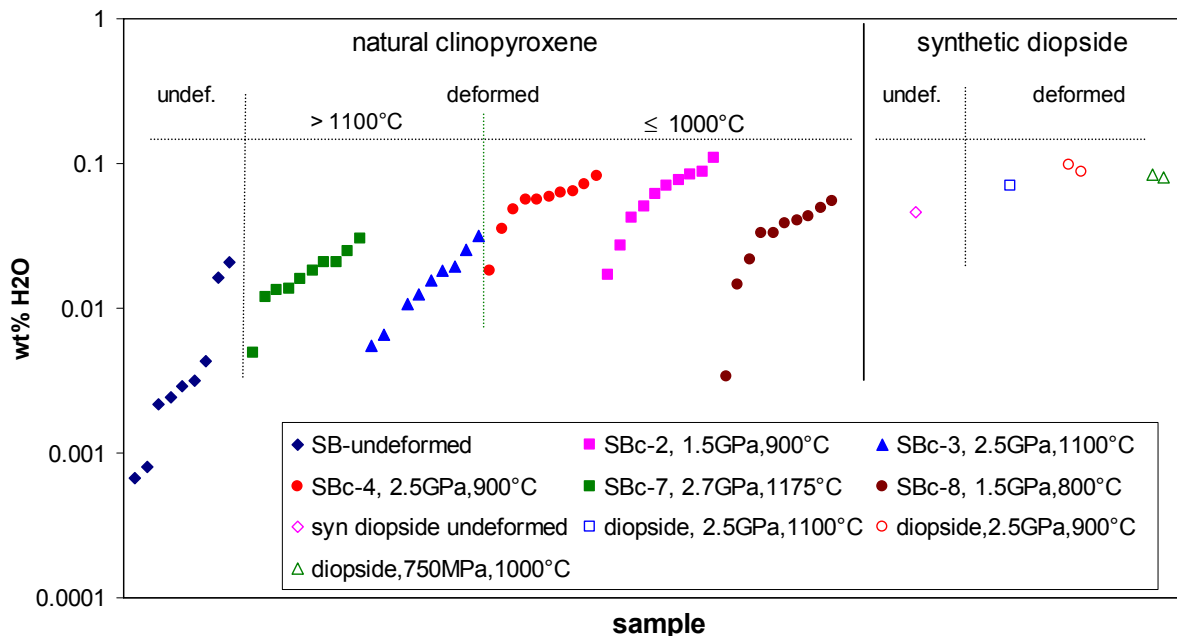


Figure 23: Variability of water content in natural clinopyroxene samples and synthetic diopside aggregates before and after deformation at quoted temperature and confining pressure.

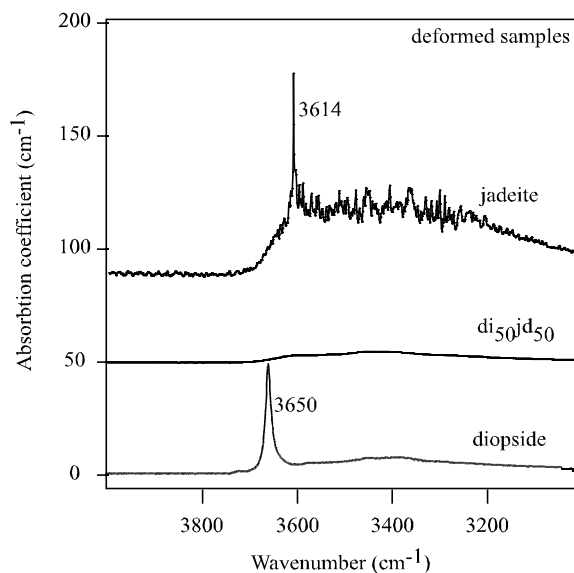


Figure 24: FTIR spectra for deformed synthetic omphacite aggregates.

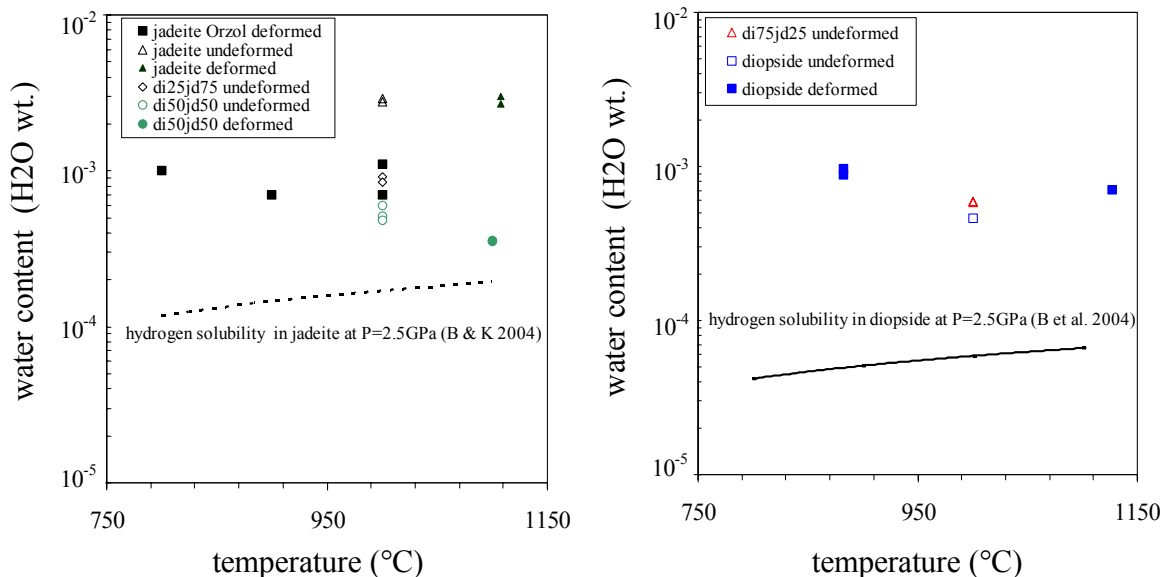


Figure 25: Bulk water content of synthetic omphacite aggregates (before and after deformation) in comparison to estimates of water solubility in jadeite [Bromiley and Keppler, 2004] (left side) and diopside [Bromiley et al., 2004] (right side). Solubility decreases with increasing diopside component as does the estimated water content of synthesized samples.

4.4. Effect of pressure on strength

The effect of confining pressure on flow stress of synthetic diopside and natural clinopyroxene samples is illustrated in Figure 26. The relation between strength and pressure for synthetic diopside aggregates appears to switch from pressure-strengthening to pressure-weakening above 1000°C at the imposed strain rates (Figure 26). At 1000°C, the strength of synthetic diopside samples increases with increasing confining pressure (Figure 26a), while at higher temperature (>1000°C) the reverse relation is observed (Figure 26b). This latter trend of softening with pressure is complemented by data gained by Bystricky and Mackwell [2001] and Chen et al. [2006] for natural clinopyroxene. In contrast, our experiments on natural clinopyroxene at a low temperature of 900°C yield strengthening with increasing confining pressure (Figure 26a) in agreement with the low temperature trend of the synthetic aggregates.

Apparent activation volumes V^* were calculated for synthetic diopside and clinopyroxene samples at identical conditions of temperature and strain rate (Figure 26). The indicated apparent activation volumes V^* were calculated by identifying the observed slopes of flow stress versus confining pressure as $V^*/(nRT)$ valid if pressure dependence originates from the activation energy $Q = Q_0 + pV^*$ alone. For natural clinopyroxene the relation between

strength and pressure shows pressure-strengthening at 900°C, i.e., a positive activation volume (Figure 26a).

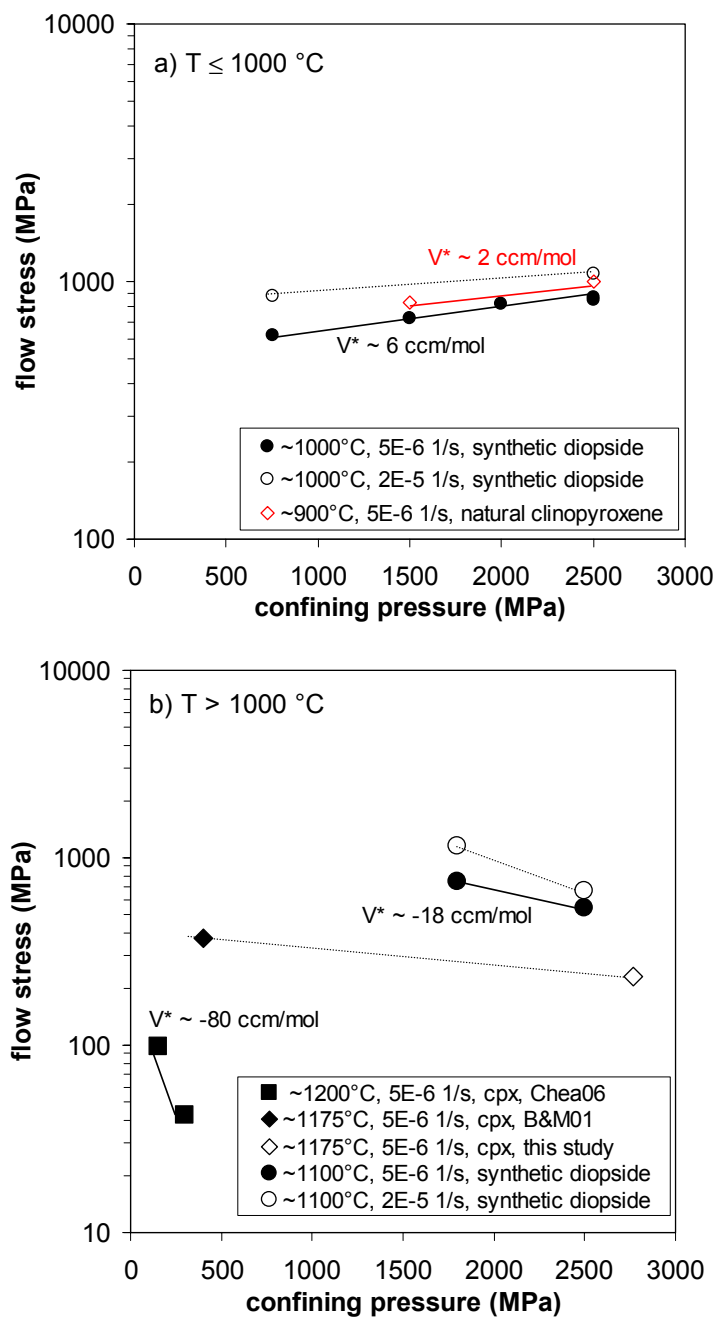


Figure 26: Relation between flow stress and confining pressure for synthetic diopside and natural clinopyroxene samples at indicated strain rates and for a) low temperature and b) high temperature. The hydrogen content is nearly constant ($\sim 0.08 \text{ wt\% H}_2\text{O}$) in this suite of samples. The indicated apparent activation volumes V^* are calculated from the observed slopes as $V^*/(nRT)$ and by using $n=8$ for synthetic diopside, $n=2.8$ for natural clinopyroxene, $n=2.7$ for natural clinopyroxene of Chen et al. [2006] data.

5. Discussion

5.1. Comparison to previous work

The strength of natural clinopyroxene samples determined in this study at 900°C and 1.5 GPa compares well with the results of Kirby and Kronenberg [1984] gained for similar conditions. Furthermore, the strength of synthetic diopside aggregates and natural Fe-bearing clinopyroxene samples is fairly similar at this moderate temperature (Figure 27), suggesting a weak effect of Fe-content on deformation processes at these conditions. At 1100°C, the strength of the natural clinopyroxene samples is significantly lower than that of synthetic diopside aggregates at similar confining pressure and strain rate (Figure 27) possibly indicating that at high temperatures (>1000°C) Fe-content decreases the strength of clinopyroxenes since hydrogen content is fairly similar for synthetic aggregates and

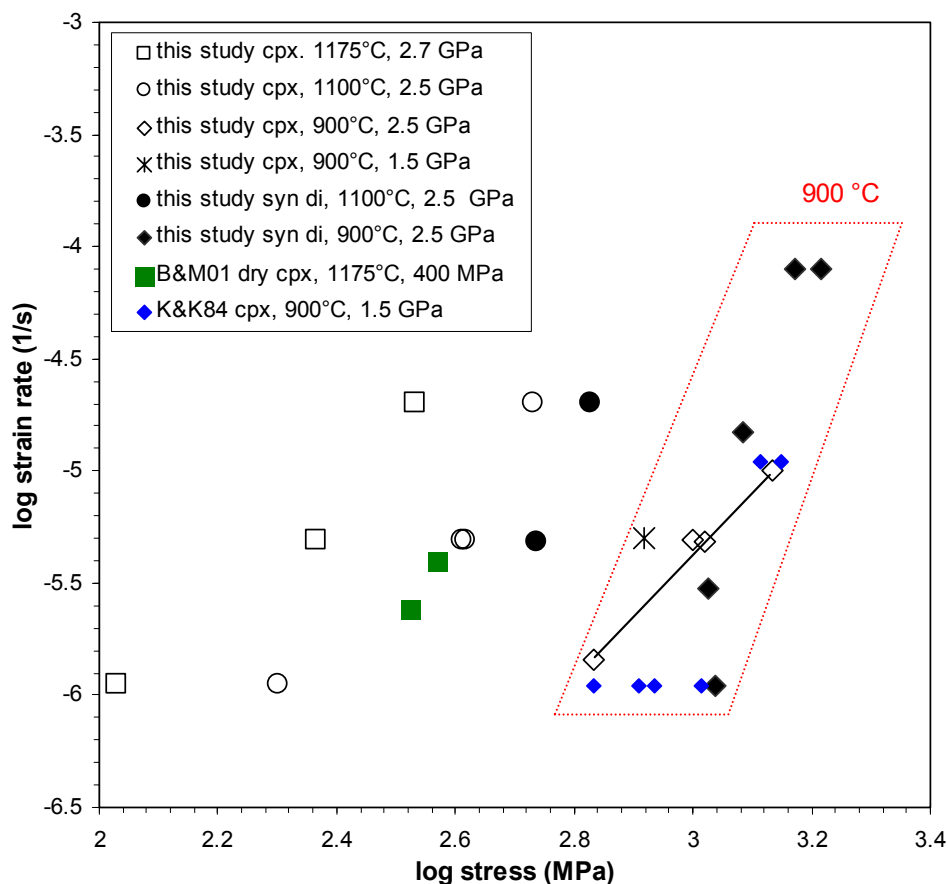


Figure 27: Strain rate-stress relations for natural clinopyroxene from Kirby and Kronenberg [K&K, 1984], Bystricky and Mackwell [B&M, 2001], and this study in comparison to results for synthetic diopside aggregates (this study).

natural aggregates deformed at high temperature (Figure 23). The strength of undried-natural clinopyroxene samples determined in this study at 2.5 GPa and 1175°C is much lower than the strength of pre-dried clinopyroxene samples deformed by Bystricky and Mackwell [2001] at 400 MPa and 1175°C (Figure 27). This relation indicates an independent effect of hydrogen content on high-temperature strength of clinopyroxene.

In direct comparison, stress exponent and activation energy derived for our jadeite aggregates agree well with those found by *Orzol et al.* [2006]. However, absolute strength values determined in this study are systematically lower than those previously determined (Figure 15). At a given stress, the difference corresponds to less than an order of magnitude in strain rate. For synthesis, we used a different glass precursor, and we did not employ seeding. Still, grain sizes achieved by the two approaches are comparable. Bulk water contents of our samples estimated by FTIR spectroscopy exceed the contents of about 0.06 to 0.12 mol H₂O/l quoted by *Orzol et al.* [2006] by a factor of 3 to 5. Microscopic inspection reveals that samples rich in jd-component (jd₁₀₀ and jd₇₅di₂₅) contain up to 4% of an unspecified phase (Figure 17, Figure 18a), which probably represents a quenched hydrous melt. The presence of this melt phase is thought to be responsible for the observed lower strength of synthetic jadeite samples compared to those investigated by *Orzol et al.* [2006]. A minor amount of non-wetting melt has probably a moderate effect on strength, as found by *Dimanov et al.* [2003] for diopside, and by *Cooper and Kohlstedt* [1986] and *Hirth and Kohlstedt* [1995] for olivine aggregates.

The mechanical data for omphacite aggregates of intermediate composition compare fairly well with the results of Zhang et al. [2006], who investigated synthetic aggregates prepared from crushed natural omphacite crystals (di₅₈jd₄₂; FeO = 1.74 wt.%; 100-200 ppm by wt. H₂O). The combined data constrain an apparent stress exponent of ~6.5 at a temperature of ~1100°C (Figure 28a). Jin et al. [2001] deformed synthetic Fe-bearing omphacite aggregates (di₇₃jd₂₇; FeO/MgO = 0.17; 100-200 ppm by wt. H₂O) at a temperature of 1500 K and a confining pressure of 3 GPa. At a strain rate of $4.6 \times 10^{-4} \text{ s}^{-1}$, a strength of ~300 MPa was derived from two stress strain curves. The conditions of these experiments are too far away from ours for a direct comparison.

In principle, it is not possible to directly compare the stress-strain rate relations obtained by deformation experiments on single crystals with those obtained on polycrystalline samples. However, our strength data on di₁₀₀ and di₇₅jd₂₅ samples agree well with the strength dependent on strain rate obtained for single crystals at temperatures above ~1000°C, where the glide system $\{110\}1/2\langle a \pm b \rangle$ was activated [*Raterron and Jaoul*, 1991] (Figure

28b). Between 800 and 1000°C, the glide system (100)[001] dominates deformation of single crystals in the tested orientation [Raterron and Jaoul, 1991]. The latter system is among those considered to govern CPO development in diopside aggregates, namely (100)[001], (010)[100], and (010)[001] [Bascou et al., 2001; 2002; Buatier et al., 1991; Godard and Van Roermund, 1995; Ulrich and Mainprice, 2005].

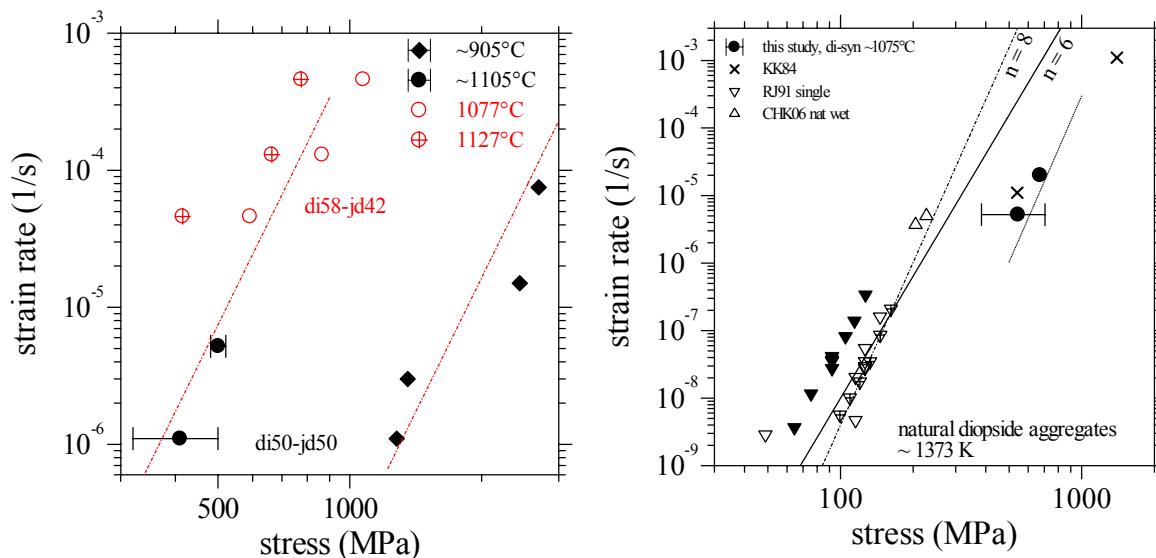


Figure 28: a) Comparison of results for intermediate compositions from this study (labeled di₅₀-jd₅₀; solid symbols) and the study of Zhang et al. [2006] (labeled di₅₈-jd₄₂; open and crossed symbols). The dashed lines represent an apparent stress exponent of 6.5. b) Comparison of our results for synthetic diopside aggregates (solid circles) with single crystal data of Raterron and Jaoul [1991] (inverted triangles) and data for natural Sleaford Bay clinopyroxenite reported by Kirby and Kronenberg [1984] (crosses) and Chen et al. [2006] (triangles). The lines represent the indicated stress exponents.

The CPO patterns observed for synthetic deformed samples are weak (Figure 20), probably due to the limited total strain. Qualitatively the patterns compare to the S-type of Godard and van Roermund [1995]. The [001] orientation describes a girdle perpendicular to the shortening direction, while the poles to the (010) plane define a point maximum parallel to the shortening direction. According to Ulrich et al. [2005], the S-type pattern is consistent with axial symmetric compression. Similar textures are observed in naturally deformed omphacite from eclogites [Godard and Van Roermund, 1995] and in experimentally deformed jadeite aggregates [Orzol et al., 2006]. A distinct type of CPO pattern, the L-type characterized by a point maximum of [001] parallel to the lineation and a girdle of [010]

perpendicular to the lineation, was reported for natural eclogites [e.g., *Helmstaedt et al.*, 1972]. Based on electron microscopy on natural samples, *Brenker et al.* [2002] postulated that cation ordering in omphacite controls development of either L-type (ordered structure) or S-type patterns (disordered structure). A subsequent study on three mantle eclogite xenoliths did not support this hypothesis [*Ulrich and Mainprice*, 2005]. Since in our case omphacite is disordered, and strain results from axial symmetric compression, the observations on CPO do not contribute to solve this controversy.

5.2. Mechanisms controlling deformation of omphacite

The microstructural and mechanical records indicate the combined activity of dislocation glide, dislocation climb and mechanical twinning during deformation of synthetic omphacite aggregates rather insensitive to composition. On the grain scale, (100) twins and low angle grain boundaries are two conspicuous microstructural features in deformed samples (Figure 18, Figure 19). The low angle grain boundaries represent activation of dislocation climb and twinning is intimately connected with glide since it results from nucleation and propagation of partial dislocations [*Frost and Ashby*, 1982].

Two state variables are central for the mechanics and kinetics of deformation of crystals by motion of dislocations, temperature and stress. The relative magnitude of these two variables with respect to melting temperature and shear modulus are associated with regimes dominated by different dislocation processes [*Frost and Ashby*, 1982]. Dislocation climb accommodated by formation and migration of jogs, steps of an edge dislocation out of its glide plane, is a thermally activated process realized by vacancy diffusion. The extent of thermal activation of diffusion processes scales with the melting temperature of a substance [e.g., *Karato et al.*, 1995; *Poirier*, 1985]. For a dislocation to glide, in contrast, the potential barrier of the lattice has to be overcome, i.e., the dislocation or a portion of it has to be activated from a low energy position in the lattice to the gliding state. By representing the strength of the lattice potential, the shear modulus constitutes the central scaling parameter for this process.

While melting temperatures increase from jadeite (1380°C) to diopside (1650°C) [*Bell and Davis*, 1969], the relation between shear modulus and composition is opposite (67 GPa for jadeite and 56 GPa for diopside) [*Duffy and Anderson*, 1989]. As a consequence, the conditions explored in our tests yield separate ranges of scaled temperature and stress for the compositional endmembers (Figure 29). The tests on jadeite aggregates correspond to

the highest homologous temperatures and the lowest normalized stresses while those on diopside aggregates represents the lowest homologous temperatures and the highest normalized stresses. The boundary between the conditions for diopside and jadeite aggregates is close to a homologous temperature of $\sim 2/3 T_m$, which is considered to separate “low-temperature glide” and “high-temperature climb” for metals [Weertman, 1999].

The notion that the deformation of aggregates with calcic composition is controlled by glide kinetics is supported by further details of the mechanical data. Apparent stress exponents as large as the ones derived for calcic aggregates (Table 7) are considered unlikely for cases where dislocation climb is the rate-controlling step. Furthermore, the increase in strength from diopsidic to intermediate compositions found here for 900 and 1000°C correlates with the composition-dependence of the shear modulus, which suggests glide as the relevant dislocation mechanism. *Dorner and Stöckhert* [2004] found such a correlation between shear modulus and strength of pyroxene single crystals by indentation hardness measurements at temperatures between 300 and 750°C. In these comparatively low temperature experiments, climb cannot be significantly activated, leaving glide as the predominant mechanism of plastic deformation. The correlation between the trends of shear modulus and observed strength with composition near the calcic endmember suggests that the deformation of the calcic pyroxenes is still controlled by dislocation glide, despite the higher temperatures of our experiments.

The relative weakness of the aggregates with the most sodic composition indicates that for these the transition to climb-controlled deformation occurs at temperatures between those attained in the present study and those explored by *Dorner and Stöckhert* [2004]. Considering the deformation of the more sodic aggregates to be controlled by dislocation climb is in perfect agreement with the observed apparent stress exponents (Table 7) and the ubiquity of subgrain boundaries (Figure 18).

Two notes are mandated in the context of explaining our observations by a switch in controlling dislocation mechanism with changes in composition and temperature. First, the small amount of melt in the jadeite aggregates is thought to cause the moderate weakening compared to the results of *Orzol et al.* [2006], but this weakening does not alter the general trend of strength with composition. Second, strength increases from either compositional endmember towards intermediate compositions at 900 and 1000°C. While a switch in

controlling dislocation mechanism suffices to explain this observation, we cannot exclude that the deviation from ideal endmember composition is additionally associated with solid

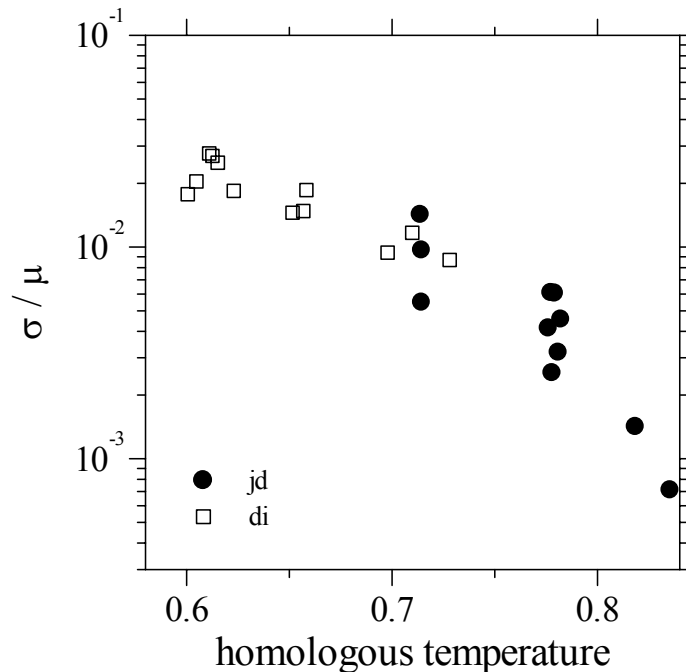


Figure 29: Normalized results for the compositional endmembers, jadeite and diopside. Determined strength values are given in relation to shear modulus and temperatures of experiments are given in relation to melting temperature. Melting temperatures of omphacite increase from $T_{m,jd} = 1380$ °C for jadeite to $T_{m,di} = 1650$ °C for diopside at a pressure of 3 GPa [Bell and Davis, 1969]. Thus, the homologous temperature ($\theta = T/T_m$) of our jadeite aggregates, ranging from 0.71 to 0.83, consistently exceeds the one of the diopside aggregates. The relation between shear modulus and composition is opposite to the one between melting temperature and composition. We calculated the ratios σ/μ using the temperature and pressure variations of shear modulus (0.013 GPa/°K, 4.5 for jadeite and 0.010 GPa/°K, 4.5 for diopside) quoted by Duffy and Anderson [1989].

solution hardening known from metals [e.g. Caceres and Blake, 2008; Dieter, 1986] resulting because solutes constitute discrete obstacles for the glide of dislocations.

The micromechanical models adopted below rest on the notion that the task of quantifying the overall kinetics of a large number of conceivable processes affecting the motion of a huge number of dislocations in a large number of grains constituting a polycrystalline aggregate can be reduced to identifying the slowest of sequential and the fastest of parallel processes. For modeling of deformation, the transitional behaviors were neglected. Here,

assumption is that, the available data for jadeite and diopside represent two distinct deformation regimes kinetically controlled by two different deformation mechanisms. The motion of a dislocation comprises stages of unhindered glide and stages during which obstacles are overcome by climb of edge segments or cross-slip of screw segments [e.g., *Hirth and Lothe*, 1982; *Reed-Hill and Abbaschian*, 1994]. Bulk strain rate is determined by the average strain achieved during glide phases between successive encounters with obstacles and the average time it takes to overcome obstacles. While the explicit calculation of bulk kinetics may be complicated, to first order the processes of glide on the one hand and climb or cross-slip on the other hand are sequential while climb and cross-slip operate concurrently and independently, i.e., are parallel processes.

5.2.1. Modeling the deformation of jd-aggregates by climb-controlled creep

The velocity with which dislocations climb is limited by the formation and mobility of jogs, steps of dislocations out of a glide plane, realized by vacancy diffusion. *Weertman* [1968] derived a general rate equation for climb-controlled creep

$$\dot{\epsilon}_{W, \text{climb}} = \alpha \frac{\mu \Omega D_{\text{eff}}}{b^{3.5} M^{0.5} kT} \left(\frac{\sigma}{\mu} \right)^{4.5}, \quad (2)$$

here given as in *Poirier* [1985] (μ : shear modulus; Ω : atomic volume; b : Burgers vector).

The dimensionless factor α is of order 1 and may differ for the two diffusion processes considered to contribute to the effective self-diffusion coefficient

$$D_{\text{eff}} = D_1 + \pi R_0^2 \rho_d D_{\text{dc}}, \quad (3)$$

volume diffusion through the lattice (D_1) and short circuit diffusion along dislocation cores (D_{dc}) of width R_0 . Eq. (2) covers popular special cases of “power-law creep” with stress exponents ranging from 3 to 6.5, when the stress-dependence of the density of dislocation sources, M , and dislocation density, ρ_d , are incorporated appropriately [see *Poirier*, 1985]. The formulation of the effective diffusion coefficient assumes that the fastest of alternative paths for the slowest constituent controls overall kinetics. The exact formulation of the contribution from core diffusion is a matter of debate [e.g., *Balluffi et al.*, 2005; *Frost and Ashby*, 1982]. In this model, the temperature dependence of creep is determined by the activation enthalpies of the involved diffusion coefficients, e.g., $D_1 = D_{1,0} \exp(-\Delta H_1 / RT)$.

The apparent stress exponent of close to 4 observed for jadeite aggregates (Table 7) is most obviously explained by a combination of a moderate dependence of dislocation density on stress and lattice diffusion as the rate-controlling parameter in eq. (2). Specifically, for $M = \text{const.}$ and $D_{\text{eff}} \approx D_1$ the stress exponent assumes a value of 4.5. The dislocation density sources considered as $M \sim 10^{16.5 \pm 1.5} \text{ m}^{-3}$ to represent a reasonable range for the dislocation source density, i.e., 1 to 1000 sources in a grain of a diameter of $\sim 10 \mu\text{m}$. The lower bound of this range was actually quoted by *Weertman* [1957] when modeling the deformation of zinc. With this estimate and $\mu_{\text{jd}} \sim 75 \text{ GPa}$, $b \sim 5 \cdot 10^{-10} \text{ m}$, and $\Omega_{\text{jd}} \sim 10^{-28} \text{ m}^3$, we gain an order of magnitude of $D_1^{\text{jd}} = A_{\text{climb}}^{\text{jd}} (\mu b)^{3.5} M^{0.5} kT \exp(-\Delta H_{\text{creep}}^{\text{jd}} / RT) / \alpha \Omega \sim 10^{-21 \pm 1.5} \text{ m}^2/\text{s}$ at 1000°C where we used the pre-exponential factor $A_{\text{climb}}^{\text{jd}}$ and an activation enthalpy for creep $\Delta H_{\text{creep}}^{\text{jd}}$ inverted for a prescribed stress exponent of 4.5 (Table 11). Alternatively, for $M = M_0 (\sigma / \sigma_0)^2$ and $D_{\text{eff}} \approx D_1$ the stress exponent amounts to 3.5. With $M_0 \sim 10^{16.5} \text{ m}^{-3}$ at $\sigma_0 \sim 100 \text{ MPa}$, almost the same estimate was gained for D_1^{jd} (see Figure 30a). These two estimates compare well to directly measured lattice diffusion coefficients for Si in various silicates [*Bejina and Jaoul*, 1997], in particular considering a) that it may be overestimated by up to an order of magnitude due to the weakening effect of melt and b) the relatively low melting temperature of jadeite. In jadeite studies for the slowest diffusing species using direct diffusion methods are lacking. In diopside crystals, Si appears to be the slowest diffusing species but the difference in diffusion coefficients among silicon, oxygen, and calcium are moderate mandating a multicomponent formulation [*Bejina and Jaoul*, 1996; R. Dohmen pers. communication]. A dominance of dislocation core diffusion, i.e., $D_{\text{eff}} \approx \pi R_0^2 \rho_{\text{d}} D_{\text{dc}}$, is unlikely for jadeite aggregates since reaching a stress exponent of about 4 then requires an unrealistically strong dependence of dislocation source density on stress of $M \propto \sigma^4$ considering the well established scaling relation $b^2 \rho_{\text{d}} = (\sigma / \hat{\alpha} \mu)^2$ with $\hat{\alpha}$ in the order of 0.1 to 3 [*Kohlstedt et al.*, 1995; *Takeuchi and Argon*, 1976; *Taylor*, 1934].

The diopside data can also be modeled by equation (2) which allows for stress exponents as high as 6.5 that reach the lower limit of the determined range (Table 11). An exponent of 6.5 results for a dominance of dislocation core diffusion, i.e., $D_{\text{eff}} \approx \pi R_0^2 \rho_{\text{d}} D_{\text{dc}} \sim \pi b^2 \rho_{\text{d}} D_{\text{dc}} = \pi (\sigma / \hat{\alpha} \mu)^2 D_{\text{dc}}$, and a stress-independent density of dislocation

sources. For this scenario, we gain an order of magnitude estimate of the coefficient for dislocation core diffusion of $D_{dc}^{di} = \hat{\alpha}^2 A_{climb}^{di} \mu^{5.5} b^{3.5} M^{0.5} kT \exp(-\Delta H_{creep}^{di} / RT) / \pi \alpha \Omega < 10^{-16.5} \text{ m}^2/\text{s}$ that appears too low in comparison to the expected order of magnitude (Figure 30). In the absence of appropriate data, we have to rely on grain boundary and interface diffusion coefficients for silicates as a lower bound for dislocation core diffusion coefficients [Balluffi *et al.*, 2005]. An estimate too low in comparison to independently determined diffusion coefficients is in accord with our reasoning that climb is not rate-controlling in diopside aggregates at the explored conditions. Climb could yield a faster than the observed rate, but glide as the slower sequential step is rate-controlling. Since cross-slip is operating parallel to climb it can be discarded as rate-limiting. For cross-slip to be rate controlling it had to be the slower of the two sequential processes, glide and cross-slip but the faster of the two parallel processes, climb and cross-slip. Yet, climb is faster than glide.

5.2.2. Glide-controlled deformation of diopside aggregates

The lattice resistance represented by the Peierls stress σ_p constitutes the central mechanical parameter for dislocation glide. An explicit flow law for glide-controlled creep

$$\begin{aligned} \dot{\epsilon}_{glide} &= 12\nu \frac{a}{b^{2.5} M^{0.5}} \left(\frac{\sigma}{\mu}\right)^{2.5} \exp\left[-\frac{Q_{glide}}{RT} \left(1 - \frac{\sigma}{\sigma_p}\right)\right] \\ &\equiv A_{glide} \sigma^{2.5} \exp\left[-\frac{Q_{glide}}{RT} \left(1 - \frac{\sigma}{\sigma_p}\right)\right] \end{aligned} \quad (4)$$

was proposed by *Weertmann* [1957] which formally coincides with the one given by *Frost and Ashby* [1982] when the dislocation source density M is assumed be linearly proportional to stress (a : distance between glide planes). The frequency

$$\nu = \nu_s \sqrt{\frac{5}{4ab} \frac{\sigma_p}{\mu}} \quad (5)$$

which is related to lattice vibrations (shear wave velocity $\nu_s^2 = \mu / \rho$) and the apparent activation energy

$$Q_{glide} = N_A \sqrt{\frac{32a^3 b^3 \mu \sigma_p}{10\pi^2}} \approx 0.57 N_A \sqrt{a^3 b^3 \mu \sigma_p} \quad (6)$$

both scale with the square root of the Peierls stress. Relying on the estimate of the Peierls stress for an edge dislocation from elastic theory [e.g., *Hirth and Lothe*, 1982], the pre-factor $12v_s/b^{2.5}M^{0.5}$ in eq. (4). can be written as

$$12v_s\sqrt{\frac{5a}{\pi(1-p)Mb^6}}\exp\left(-\frac{\pi a}{(1-p)b}\right)\sim O_{(1)}\frac{v_s}{\sqrt{M}}\frac{\sigma_p^{11/12}N_A^{5/6}}{\mu^{1/12}Q_{\text{glide}}^{5/6}}. \quad (7)$$

Since Peierls stress, apparent activation energy, and pre-exponential factor are not independent of each other, one can either stick with the traditional parameterization of the flow law using A_{glide} , σ_p , and Q_{glide} or alternatively take the perspective that the three central, purely geometrical characteristics of the gliding dislocations, a , b , and M , control strain rate. It is important to emphasize that in eqs. (5) to (7) derived from elastic models the parameters a and b have phenomenological rather than simple crystallographic character for multi-constituent minerals with low symmetry and complex bonding [*Hirth and Lothe*, 1982]. Furthermore, the representation of the elastic behavior of a solid by only two elastic parameters (here, shear modulus and Poisson's ratio) rests on the assumption of isotropy, which is clearly not true for pyroxenes.

a)

composition	n [-]	$\ln(A_{\text{climb}} [\text{MPa}^{-n} \text{s}^{-1}])$	ΔH_{creep} [kJ/mol]
jd	4.5	4.8±5.6	443±57
	3.5	0.7±4.3	341±43
di	6.5	-25.7±2.6	313±27

b)

composition	model	M [m ⁻³]	σ_p [GPa]	Q_{glide} [kJ/mol]	a_{calc} [nm]	b_{calc} [nm]	$\ln(A_{\text{glide}})$ [MPa ^{-2.5} s ⁻¹]
di	eqs. (4), (7)	<i>3.4·10^{16.5±1.6}</i>	7.4±0.9	528±23	0.23±0.02	0.74±0.02	15.4±3.1

Table 11: Results of micromechanical modeling for a) climb-controlled creep according to eq. (2) and b) glide-controlled creep according to eqs. (4) and (7). Italic font indicates parameters that were prescribed in the inversion [stress exponents in a) and the range of dislocation source density in b)]. Bold printed values are actual inversion results while normal font indicates parameters calculated from the inverted ones using $\mu_{\text{di}} \approx 56$ GPa and $v_{\text{s,di}} \approx 4140$ m/s.

Eq. (4) fits our mechanical data for synthetic diopside aggregates at least as well as the simple power law relation (1) (see Figure 16b). Constraining the dislocation source density to a reasonable range of $M \sim 10^{16.5 \pm 1.6} \text{ m}^{-3}$, the inversion yields a Peierls stress (Table 11) that nearly coincides with the value of $6.5 \pm 0.8 \text{ GPa}$ found by *Dorner and Stöckhert* [2004] for diopside. Note, evaluating the hardness data relying on eq.(4), rather than the slightly modified version used by *Dorner and Stöckhert* [2004] yields a somewhat lower value of $5 \pm 1 \text{ GPa}$. Furthermore, a consistency check using the characterization of *Frost and Ashby* [1982] demonstrates that by holding $Q_{\text{glide}} < 0.2\mu b^3$ the apparent activation energy qualifies as a case of “weak obstacles”. The corresponding obstacle spacing $l \ll \mu b / \sigma_p \sim 10b$ indeed suggests lattice or Peierls resistance to constitute the principal obstacle for glide. Finally, the values of a and b calculated from the inversion results are obviously of the right order of magnitude for lattice parameters. Thus, all parameters determined for the dislocation glide model are fully consistent with physical considerations or independently determined data.

Eq. (11) fits the mechanical data for Sleaford Bay clinopyroxenite samples well (using a shear modulus of 56.1 GPa and a shear wave velocity of 4140 m/s). Without any constraints on the fitting parameters, we gain a reasonable dislocation source density of $M \sim 10^{16.0 \pm 1.6} \text{ m}^{-3}$, a Peierls stress of $\sigma_p = 8.5 \pm 1.3 \text{ GPa}$, and an apparent activation energy $Q_{\text{glide}} = 508 \pm 22 \text{ kJ/mol}$. These fitting parameters closely agree with our results for synthetic polycrystalline diopside aggregates (Table 11) indicating that the deformation of the natural pyroxenite samples is also governed by dislocation glide at the explored conditions.

composition	model	M [m^{-3}]	σ_p [GPa]	Q_{glide} [kJ/mol]	a_{calc} [nm]	b_{calc} [nm]	$\ln(A_{\text{glide}})$ [$\text{MPa}^{-2.5} \text{ s}^{-1}$]
Sleaford Bay cpx	eqs. (4), (7)	$1.0 \cdot 10^{16.0 \pm 1.6}$	8.5 ± 1.3	508 ± 22	0.22 ± 0.02	0.77 ± 0.02	26.56 ± 3.1

Table 12: Results of micromechanical modeling for glide-controlled creep according to eqs. (4) and (7). Bold printed values are actual inversion results while normal font indicates parameters calculated from the inverted ones using $\mu_{\text{di}} \approx 56 \text{ GPa}$ and $v_{\text{s,di}} \approx 4140 \text{ m/s}$.

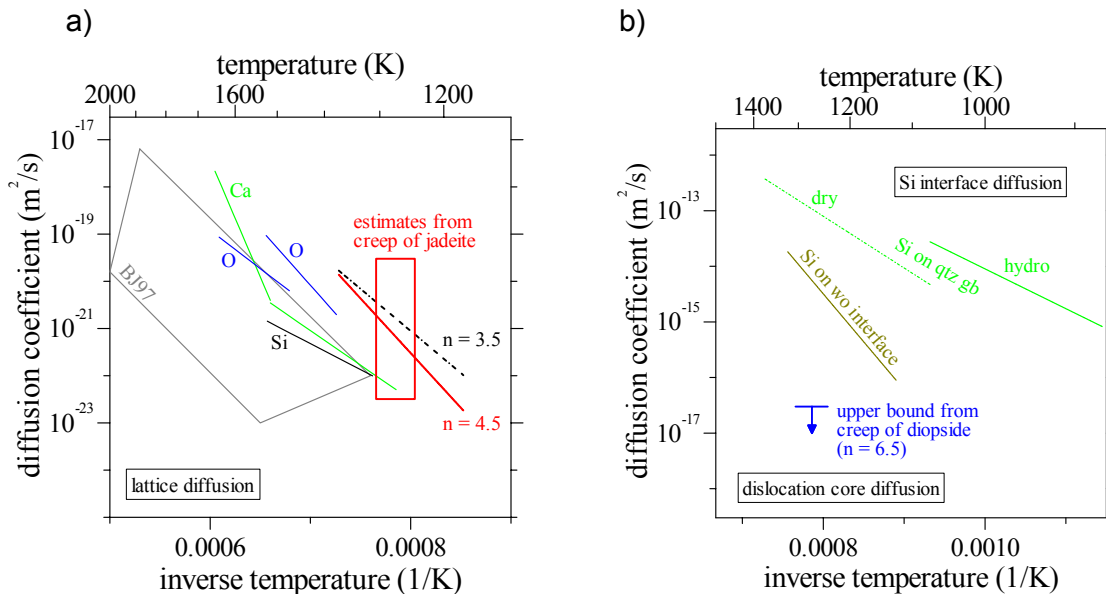


Figure 30: Comparison between diffusion coefficients estimated from modeling the observations for a) jadeite and b) diopside aggregates using eq. (2) for climb-controlled creep and diffusion data from the literature. a) the thick solid and dashed lines give the estimates for lattice diffusion coefficients for stress exponents of 4.5 and 3.5, respectively (Table 11). The slopes of these lines are constrained by the corresponding activation enthalpies, ΔH_{creep} . The box indicates the absolute uncertainty of the estimates. The trapeze-like area labeled BJ 97 represents silicon self-diffusion coefficient data in silicate mineral obtained by different authors [Bejjina and Jaoul, 1997]. The thin solid lines labeled with elements give diffusion coefficient of mentioned element in diopside at different temperature. b) The micromechanical modeling yields an upper bound for the dislocation core diffusion coefficient indicated by the thick horizontal line and the arrow. For comparison, literature data for Si interface diffusion are given (Si on quartz grain boundary under dry and hydrothermal conditions [Farver and Yund, 2000]; Si on wollastonite interfaces [Milke and Heinrich, 2002]).

5.3. Rheological scaling relations

Constraining the rheology of the mechanical endmembers, jadeite and diopside, employing two different micromechanical constitutive equations was the necessary first step toward the ultimate goal of quantitatively describing the behavior of omphacite aggregates of intermediate composition. In particular, the lack of understanding how the sequential processes of glide and climb can be combined in a unifying flow law hinders a quantitative modeling of the compositional dependence of the rheology of omphacite aggregates. Therefore, simple scaling relations are used in the following that are expected to be applicable for the two considered deformation mechanisms.

5.3.1. The effect of composition on strength

In the case of climb-controlled creep, the thermal activation term associated with the effective diffusion coefficient in eq. (2) suggests a homologous temperature scaling such that $D \propto \exp(-\Delta H / RT) \equiv \exp(-\alpha / \Theta)$. Note, while omphacites along the join diopside-jadeite melt incongruently, the difference between solidus and liquidus is moderate (<30 K) at elevated pressure [Bell and Davis, 1969], permitting calculation of “unique” estimates of homologous temperatures for intermediate compositions. The activation enthalpy observed for jadeite aggregates (Table 11) yields an estimate of $\alpha \approx 30$. Thus, the relation between strength as given by eq. (2) and bulk composition ($X=0$ corresponds to jadeite, $X=1$ corresponds to diopside) results to

$$\begin{aligned} \left. \frac{\partial \ln \sigma}{\partial X} \right|_{\dot{\epsilon}, T} &\approx \frac{1}{n} \left(3.5 \frac{\partial \ln \mu}{\partial X} + \frac{1}{6} \frac{\partial \ln \Omega}{\partial X} - \frac{\alpha}{\Theta^2} \frac{\partial \Theta}{\partial X} \right) \\ &\approx \frac{1}{4.5} (-0.9 + 0.01 + 6.0) = 1.1 \pm 0.2 \end{aligned} \quad (8)$$

The calculation demonstrates that the dependence of climb-controlled strength on composition is in fact dominated by the change in melting temperature. The dependence of shear modulus on composition is subordinate and the relation of lattice parameters on composition is negligible.

In contrast, the dependence of shear modulus on composition dominates the scaling relation for glide-controlled creep as described by eq. (4). We arrive at an estimate of

$$\begin{aligned} \left. \frac{\partial \ln \sigma}{\partial X} \right|_{\dot{\epsilon}, T} &\approx -\frac{1}{n'} \left. \frac{\partial \ln \dot{\epsilon}_{\text{glide}}}{\partial X} \right|_{\dot{\epsilon}, \sigma} \approx \frac{1}{n'} \left(2.5 + \frac{Q_{\text{glide}}}{RT} \right) \frac{\partial \ln \mu}{\partial X} \\ &\approx \frac{1}{8.3 \pm 1.5} (2.5 + 50) (-0.9) = -1.8 \pm 0.4 \end{aligned} \quad (9)$$

whose magnitude is actually controlled by the relation between the apparent activation energy and shear modulus (6). Here, we refrained from explicitly tracking the dependence of lattice parameters on composition right the way because $\partial \ln \mu / \partial X \gg \partial \ln \Omega / \partial X$ as shown above. The estimated scaling relations (8) and (9) compare favorably with the observed trend in strength dependent on composition at given temperature and strain rate (Figure 16).

5.3.2. The effect of hydrogen content and pressure on strength

Considering the above discussion of glide-controlled and climb-controlled creep of omphacite aggregates, we envision these two deformation regimes for diopside aggregates, too. For these regimes, different ideas have been proposed to explain the effect of hydrogen (protons) on the strength of nominally anhydrous silicate minerals. Basically, hydrogen incorporation changes the speciation and concentration of point defects. On the one hand, hydrolysis of Si-O bonds may affect the Peierls barrier important for dislocation glide. On the other hand, the addition of positively charged protons may affect jog mobility controlling dislocation climb [Chen *et al.*, 2006; Kohlstedt, 2006]. The availability of hydrogen to a system, as expressed by water fugacity, and the degree to which hydrogen can be incorporated in the lattice of the solid constituents, quantified by solubility, constitute the two central parameters for the point defect chemistry of hydrogen-associated defects. Since both parameters, fugacity and solubility, strongly depend on pressure, the effect of hydrogen and pressure on strength on silicates must be considered together.

Our results indicate that at temperatures below about 1100°C dislocation glide controls the deformation of diopside aggregates. In this regime, the relation of flow stress to pressure is likely controlled by the dependence of the elastic parameter on pressure [Poirier, 1985]. While hydrolysis of Si-O bonds may affect the Peierls barrier, too, little quantitative information on this effect is available for any material. In addition, the observed pressure-strengthening at temperatures below 1000°C appears to be independent of the hydrogen content of tested samples. Recall that the hydrogen content of the natural samples

deformed at low temperature (<1000°C) in this study is considerably less than that of the synthetic aggregates (see Table 11, Figure 23). When accounting for the pressure-dependence of the various parameters in eq. (4) in the same way as done for compositional effects in eq. (9), one finds that the dependence of the apparent activation energy (eq. (6)) on shear modulus and its pressure sensitivity dominate the scaling relation. Using $\partial \ln \mu / \partial p \approx 1 / \mu \approx 1 / 60 \text{ GPa}^{-1}$ [Duffy and Anderson, 1989], one arrives at an estimate for the sensitivity of strength to pressure of $\partial \ln \sigma / \partial p|_{\dot{\epsilon}, T} \sim 0.05 \text{ to } 0.12 \text{ GPa}^{-1}$. This estimate corresponds to an apparent positive activation volume of $V^* < 10 \text{ cm}^3 / \text{mol}$ in reasonable agreement with the observations (Figure 26).

At high temperature ($T > 1000^\circ\text{C}$), when dislocation climb is believed to be rate controlling, the experimental data of this study constrain a weakening effect of pressure on strength of diopside. The analysis of the data yields an apparent activation volume of $-18 \text{ cm}^3 / \text{mol}$ (Figure 26). Recall that the natural samples appear to gain water when deformed at high temperature ($>1000^\circ\text{C}$) in our apparatus (Figure 23). The resulting hydrogen contents are similar to that of the synthetic samples. At face value, data of Chen et al. [2006] also indicate a negative activation volume at 1200°C (Figure 26). Notably, samples of Sleaford Bay clinopyroxenite deformed by Chen et al. [2006] and also Bystricky and Mackwell (2001) were pre-dried and consequently had much lower hydrogen contents than either our natural or synthetic samples. A negative activation volume has been reported before for dislocation climb controlled deformation of olivine aggregates [Li et al., 2006]. In case of olivine this observation from deformation experiments coincides with measurements of a slightly negative activation volume for silicon self-diffusion [see Bejina et al.].

In a first step, we can follow the phenomenological homologous temperature scaling concept with $D \propto \exp[-(\Delta E + \Delta V) / RT] \equiv \exp(-\alpha / \Theta)$ assuming that the change in melting temperature scales with the intrinsic activation volume ΔV of the rate-controlling atomic processes. Recall that this scaling approach worked well to explain the dependence of strength on composition for climb-controlled creep of omphacite aggregates (see 5.3.1.). The melting temperature of diopside increases with increasing pressure, i.e., the homologous temperature decreases. Thus, a decrease in diffusion coefficient is expected with increasing pressure. Our study does not provide unique direct constraints on the kinetics of dislocation climb controlled creep of diopside aggregates. The activation enthalpy for climb controlled creep observed for jadeite aggregates yields an estimate of $\alpha \approx 30$ in good agreement with a number of silicates [Karato, 1989]. Using this value for a

first order analysis, the predicted pressure dependence of the diffusion coefficient amounts to

$$\begin{aligned} \left. \frac{\partial \ln D}{\partial p} \right|_T &= -\frac{\alpha}{\Theta^2} \frac{\partial \Theta}{\partial p} \approx \frac{30}{(0.75)^2} \left(-0.055 \frac{1}{\text{GPa}}\right) = -2.9 \text{ GPa}^{-1} \\ \Delta V &\equiv -RT \left. \frac{\partial \ln D}{\partial p} \right|_T \approx 8.31 \frac{\text{J}}{\text{mol} \cdot \text{K}} \cdot 1300 \text{ K} \cdot 2.9 \text{ GPa}^{-1} \quad (10) \\ &= 3.1 \cdot 10^{-5} \frac{\text{m}^3}{\text{mol}} \approx 31 \frac{\text{cm}^3}{\text{mol}} \end{aligned}$$

Consequently, the homologous temperature scaling predicts an increase in strength with pressure in contrast to the observed pressure-weakening (Figure 26).

The failure of the simple homologous temperature scaling mandates further analyses. In the absence of direct information on the effect of pressure on silicon self-diffusion in clinopyroxene, the likely rate controlling atomistic step, we systematically examine the relation between previously reported activation parameters for creep of clinopyroxene aggregates and thermodynamic conditions. Note, the apparent activation energies quoted in the following simply result from an analysis of deformation data for which the various authors relied on the phenomenological power law, equation (1). At face value, the correlation of these apparent activation energies for creep with confining pressure (Figure 31b) reveals a negative activation volume in accord with our direct observations (Figure 26). However, the various data sets also represent different conditions for hydrogen which may bias the pressure effect. If, for example, bulk strain rate depends on water fugacity, i.e., $\dot{\epsilon} \propto f_{\text{H}_2\text{O}(p,T)}^\alpha \exp(-H_{(p)}/RT)$, as suggested by Chen et al. [2006] and Hier-Majumder et al. [2005] the apparent activation energy for creep follows as $Q \equiv -R \partial \ln \dot{\epsilon} / \partial(1/T) = H_{(p)} - \alpha R \partial \ln f_{\text{H}_2\text{O}(p,T)} / \partial(1/T)$ and the apparent activation volume results as $V \equiv \partial Q / \partial p = V^* - \alpha R \partial^2 \ln f_{\text{H}_2\text{O}(p,T)} / \partial(1/T) \partial p$, i.e., the variations in fugacity from experiment to experiment potentially mask the true intrinsic activation enthalpy and its variation with state (Figure 31c, d).

In the presence of a sufficiently large reservoir of free water, diopside crystals incorporate a well defined amount of hydrogen. The actual amount depends on temperature and pressure and is referred to as solubility. The variation of solubility with thermodynamic conditions is conveniently quantified using the fugacity of the free water phase. For example, Bromiley et al. [2004] found $C_{\text{OH}} = B f^{1/2} \exp(-p \Delta V_{\text{OH}} / RT)$ for the hydrogen solubility in Cr-diopside. It is furthermore believed that this relation between solute concentration and fugacity can be

inverted when the solubility limit is not reached. A “shortage” of water is indicated when samples contain less hydrogen than in principle possible at given pressure and temperature. One can calculate the effective fugacity of the “short” water phase from the hydrogen concentration and it will be less than the fugacity of free water at the same conditions.

All data at low confining pressure (<500 MPa) indicate a weakening effect of water on the flow strength of clinopyroxene [e.g., *Chen et al.*, 2006; *Dimanov et al.*, 2003; *Dimanov and Dresen*, 2005]. A general decrease of apparent activation energy for creep with increasing hydrogen content is found (Figure 31a). Thus, interpreting the above described relation between activation energy and pressure actually has to be considered with caution. In closer detail, the increasing contribution of a hydrogen-related defect appears to continuously decrease the activation energy for samples with hydrogen contents below the solubility limit (Figure 31b). The collected data give some indication that this reducing effect diminishes when solubility is reached. One has to consider that the correlation between activation energy and hydrogen content may be further complicated toward low hydrogen contents because below a certain hydrogen content deformation kinetics will be unaffected by the small amount of hydrogen defects but will be controlled by the concentration of some other point defect. This critical hydrogen content may be quite low though and actually fall below the currently tested conditions [compare *Costa and Chakraborty*, 2008].

We now explicitly account for an effect of hydrogen concentration on the diffusivity of vacancies of the rate-controlling species, i.e., $D = D_{0(C_{OH})} \exp[-(\Delta E + \Delta V) / RT]$. Then, the apparent activation volume results as

$$\begin{aligned} \Delta \tilde{V} &\equiv -RT \left. \frac{\partial \ln D}{\partial p} \right|_T = -RT \frac{\partial \ln D_0}{\partial p} + \Delta V \\ &= -RT \frac{\partial \ln D_0}{\partial C_{OH}} \frac{\partial C_{OH}}{\partial p} + \Delta V \end{aligned} \quad (11)$$

According to Bromiley et al. [2004], the hydrogen solubility in diopside calculates as $C_{OH} = Bf^{1/2} \exp(-p\Delta V_{OH} / RT)$. The apparent activation volume of hydrogen incorporation was determined to $\Delta V_{OH} = 7.43 \text{ cm}^3/\text{mol}$ and the variation of fugacity with pressure can be calculated from the equation of state of pure water (Figure 31d). Thus, for wet samples, i.e., samples that achieved their maximum capacity to store hydrogen at given pressure and temperature, the relative variability in hydrogen concentration with pressure is

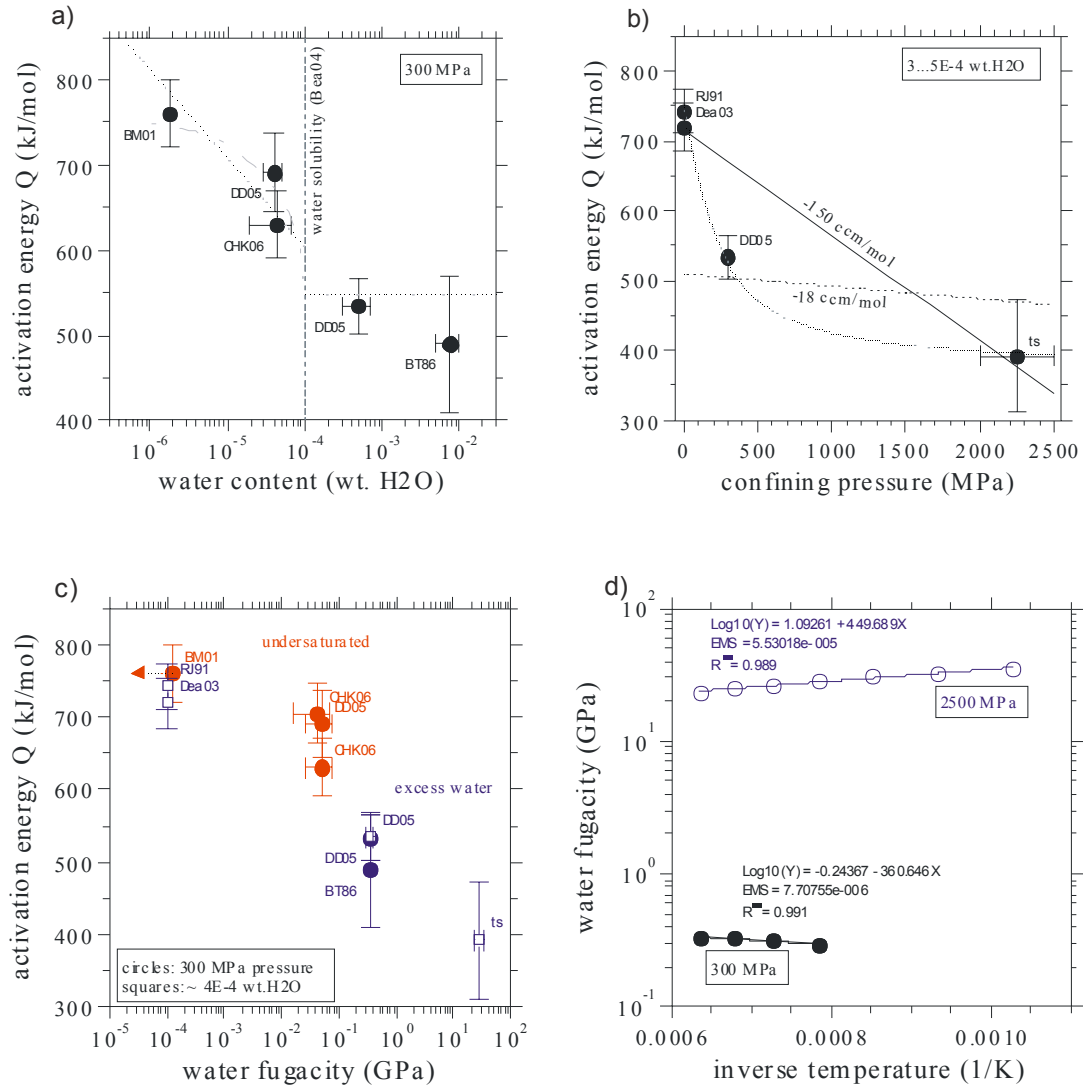


Figure 31: Relation between apparent activation energy for creep of clinopyroxene aggregates and a) water content at 300 MPa confining pressure, b) confining pressure at a water content of 3 to $5 \cdot 10^{-4}$ wt. H₂O corresponding to water in excess of the solubility for diopside aggregates, and c) water fugacity estimated from the water content (undersaturated samples after Bromiley et al. [2004] or the equation of state of water (excess water), d) Water fugacity trends with temperature at indicated pressures. In a), grey dashed lines indicate hypothetical relations. In b), lines and numbers indicate apparent activation volumes corresponding to the trends associated with the data. (BT86: Boland and Tullis [1986], BM01: Bystricky and Mackwell [2001], CHK06: Chen et al. [2006], DD05: Dimanov and Dresen [2005], Dea03: Dimanov et al. [2003], KK84: Kirby and Kronenberg [1984], RJ91: Raterron and Jaoul [1991], Bea04: Bromiley et al. [2004], ts: this study).

$\partial \ln C_{\text{OH}} / \partial p = 0.5 \partial \ln f / \partial p - \Delta V_{\text{OH}} / RT \approx (1.1 - 0.7) \text{ GPa}^{-1}$. For a simple power law relation between diffusion coefficient and hydrogen concentration, i.e., $D_0 \propto C_{\text{OH}}^\alpha$, we find-

$\partial D_0 / \partial p = \alpha \partial \ln C_{\text{OH}} / \partial p$. Since the diffusion coefficient dominates the dependence of strength on pressure compared to shear modulus and lattice parameters, i.e.,

$$\left. \frac{\partial \ln \sigma}{\partial p} \right|_{\dot{\epsilon}, T} \approx \frac{1}{n} \left(3.5 \frac{\partial \ln \mu}{\partial p} + \frac{1}{6} \frac{\partial \ln \Omega}{\partial p} - \frac{\partial \ln D}{\partial p} \right) \approx -\frac{1}{n} \frac{\partial \ln D}{\partial p} \quad (12)$$

the fugacity term constitutes the only significant contributor to a negative activation volume. The strength of samples for which hydrogen concentration is controlled by preparation rather than by the activity of free water at run conditions, the “accidental” bias between pressure and hydrogen content has to be explicitly accounted for as attempted in Figure 31b where data from experiments at a range of pressures but with nominally almost identical hydrogen content in the samples are collected. This collection qualitatively supports our findings of a negative activation volume but also indicates a non-trivial relation between activation energy and pressure. Clearly, further work is needed to improve the characterization the conditions of the various studies with respect to water activity before a more quantitative model can be constrained.

5.4. Geological implications

Experimental deformation studies have greatly improved our knowledge about the flow behavior of rocks. The large differences in strain rate between laboratory studies and natural deformation conditions and differences between thermodynamic conditions of geological environments and laboratory conditions are main problems in extrapolating laboratory derived data to natural conditions. At face value, our tests apply only to temperatures at which disordered omphacite is stable and to “wet” high pressure environments as probably found in subduction zones. Omphacites of intermediate compositions are disordered at $T > 700^\circ\text{C}$ (Figure 1). While *Brenker et al.* [2002] suggested that the glide systems are different for ordered and disordered omphacite, *Ulrich et al.* [2005] questioned a significant effect of ordering on the glide systems relevant for CPO development.

While our diopside samples are undoubtedly “wet” in the sense that the amount of hydrogen present is close to or exceeds the hydrogen solubility (Figure 25), the kinetics of dislocation glide are intrinsically much less sensitive to point defect chemistry than the

kinetics of dislocation climb and are probably less sensitive to the presence of water-related defects in the nominally anhydrous pyroxenes. Numerical studies revealed that Peierls-type flow laws (eq. 4) as used here to model the glide controlled deformation of diopside aggregates may play a crucial role for plastic deformation to localize in shear zones [Karato *et al.*, 2001; Kaus and Podladchikov, 2006].

It is likely impossible to judge whether glide was rate limiting during ancient deformation of omphacite in presently exposed rocks. In fact, glide-controlled deformation may be inferred from the microstructural record, where inhomogeneous crystal plastic deformation is evident, but features indicating climb and dynamic recrystallization are absent. Microstructures observed in omphacite in eclogitic rocks are variable [e.g., Boland and Tullis, 1986; Buatier *et al.*, 1991; Godard and Van Roermund, 1995; Müller and Franz, 2008; Van Roermund and Boland, 1981], but deformation twin lamellae on (100) and subgrain boundaries are almost omnipresent features. Subgrains resulting from post-deformational recovery are difficult to differentiate from incipient dynamic recrystallization. Apparently, Piepenbreier and Stöckhert [2001] give the only report of unequivocal evidence for dynamic recrystallization in eclogite rocks. Geothermometric arguments suggest that the corresponding deformation proceeded below about 500°C. This temperature estimate is indeed in accord with the extrapolation of the flow laws derived in this study to natural strain rates indicating a switch from glide to climb between 400 and 500°C (Figure 32). Note, the predicted transition temperature is the lowest possible because the applied laws in this study for the deformation of melt-bearing jadeite aggregates kinetically controlled by climb (Table 11a) and diopside aggregates controlled by glide (Table 11b) constitute lower bounds for the two deformation mechanisms in the system di-jd according to the discussed scaling relations. When allowing for the presence of Fe as typical for natural omphacites, however, some weakening compared to the current predictions is possible due to the reduction in shear modulus on the one hand and due to the acceleration of diffusion kinetics on the other hand resulting from the relation between the multivalence of iron and the incorporation of hydrogen into silicates' lattices.

With considering lower bounds for Fe-free systems, predicted stresses are on the order of about 1 GPa for a temperature of about 500°C. Several geological observations suggest that stresses of this magnitude are not characteristic of high-pressure subduction zone environments (see Stöckhert [2002] for a review). Recent 2D geodynamic modeling by [Kaus and Podladchikov, 2006] showed that 1D strength envelopes as presented in Figure 32 tend to overestimate stresses in the lithosphere because shear heating remains

unaccounted for and in-situ stress-depth profiles do not obey a constant strain rate boundary condition. I propose localized and episodic high-stress events as deduced for several crustal environments [Küster and Stöckhert, 1999; Trepmann and Stöckhert, 2003] as a hypothesis in accord with both, the geological record and these methodological considerations. Strain-free recrystallites restricted to the immediate vicinity of garnet crystals [Müller and Franz, 2008] may be a product of stress concentration on an even smaller scale.

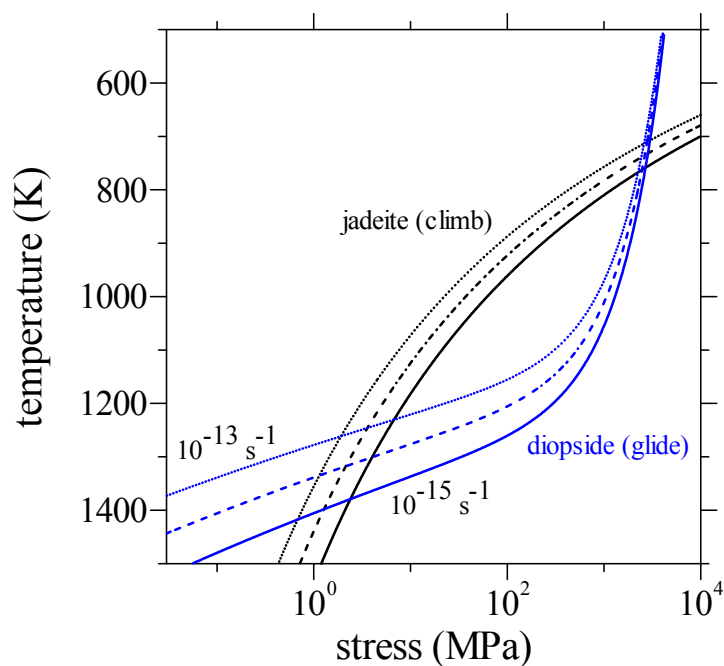


Figure 32: Extrapolation of the determined climb and glide flow laws for jadeite and diopside aggregates (Table 11) to geological strain rates of 10^{-13} (dotted lines), 10^{-14} (dashed lines), and 10^{-15} s^{-1} (solid lines).

6. Summary

Synthetic omphacite aggregates were crystallized from glass powders with five compositions along the solid-solution series, diopside-jadeite in the stability field of jadeite. Triaxial compression experiments were performed on the synthesized samples in a solid medium apparatus at a confining pressure of 2.5 GPa, temperatures between 900 and 1100°C, and strain rates between $1.1 \times 10^{-6} \text{ s}^{-1}$ to $8.5 \times 10^{-5} \text{ s}^{-1}$. To investigate the effect of confining pressure on deformation mechanisms, 4 experiments were run at <2.5 GPa on synthetic diopside aggregates. Also 7 experiments were carried out on samples of Fe-bearing Sleaford Bay clinopyroxenite at confining pressures ranging from 1.5 to 2.7 GPa in order to compare these results with published data and to investigate the effect of Fe-content on the strength of samples. Bulk water content of synthetic samples systematically decreases with increasing diopside component. The strength of synthetic aggregates decreases with increasing temperature and decreasing strain rate. Jadeite is the weaker endmember at all explored conditions. Intermediate compositions are stronger than either endmember at 900°C and 1000°C. Samples of calcic compositions deformed at high differential stresses reveal abundant mechanical (100)[001] twins, whereas jadeite aggregates deformed at low differential stress show well developed subgrain boundaries and locally recrystallized grains. A weak crystallographic preferred orientation is developed in the deformed samples. Combining the mechanical data and observed microstructures for deformed synthetic samples reveal that the rate-controlling deformation mechanism differs for the two compositional endmembers. Deformation of diopside aggregates is controlled by dislocation glide at the explored conditions, while the kinetics of dislocation climb controls the deformation of jadeite aggregates. The performed micromechanical modeling yields physically plausible flow law parameters. The variation in strength with composition obeys scaling by the dependence of melting temperature and shear modulus on composition. The strengths of natural clinopyroxene samples are near to synthetic diopside aggregates at lower temperatures. The apparent insensitivity of the deformation behavior of pyroxene aggregates to Fe- and H-content is in accord with these conclusions because in contrast to climb-controlled deformation, glide-controlled deformation should be insensitive to impurity concentrations that affect diffusion kinetics. Since water fugacity and hydroxyl solubility change with confining pressure, the effect of pressure and hydrogen must be considered together in deformation experiments. The comparison of deformation data on natural

clinopyroxene and synthetic diopside shows strengthening of samples with pressure and a positive activation volume at 900°C, while a switch to pressure-weakening seems to occur above 1000°C. The extrapolation of the constrained flow laws to geological strain rates indicates considerable strength for omphacite aggregates at temperatures up to 1000°C. Long term deformation of eclogites in subduction zones by dislocation creep appears therefore unlikely. It is suspected that exhumed eclogites exhibiting omphacite microstructures indicative of crystal plastic deformation probably experienced high-stress episodes related to seismic events.

References

- Anderson, D. L. (2007), The Eclogite Engine: Chemical geodynamics as a Galileo thermometer, in *Plates, Plumes, and Planetary Processes, GSA Special Paper*, edited by G. R. F. D. M. Jurdy, pp. 47-64, GSA.
- Aoya, M. (2001), P-T-D path of eclogite from the Sanbagawa belt deduced from combination of petrological and microstructural analyses, *Journal of Petrology*, *42*, 1225–1248.
- Asahara, Y., and E. Ohtani (2001), Melting relations of the hydrous primitive mantle in the CMAS-H₂O system at high pressures and temperatures, and implications for generation of komatiites, *Phys. Earth Planet. Inter.*, *125*, 31-44.
- Ave Lallemand, H. G. (1978), Experimental deformation of diopside and websterite, *Tectonophysics*, *48*, 1-27.
- Azough, F., R. Freer, K. Wright, and R. Jackson (1998), A computer simulation study of point defects in diopside and the self-diffusion of Mg and Ca by a vacancy mechanism, *Mineralogical Magazine*, *62*(5), 599-606.
- Balluffi, R. W., S. M. Allen, and W. C. Carter (2005), *Kinetics of Materials*, J. Wiley & Sons.
- Bascou, J., G. Barruol, A. Vauchez, D. Mainprice, and M. Egydio-Silva (2001), EBSD-measured lattice-preferred orientations and seismic properties of eclogites, *Tectonophysics*, *342*, 61-80.
- Bascou, J., A. Tommasi, and D. Mainprice (2002), Plastic deformation and development of clinopyroxene lattice preferred orientations in eclogites, *Journal of structural geology*, *24*, 1357-1368.
- Bejina, F., and O. Jaoul (1996), Silicon self-diffusion in quartz and diopside measured by nuclear micro-analysis methods, *Physics of the Earth and Planetary Interiors*, *97*(1-4), 145-162.
- Bejina, F., and O. Jaoul (1997), Silicon diffusion in silicate minerals, *Earth and Planetary Science Letters*, *153*, 229-238.
- Bejina, F., O. Jaoul, and R. C. Liebermann (1999), Activation volume of Si diffusion in San Carlos: Implications for upper mantle rheology, *Journal of Geophysical Research*, *104*, 25529-25542.
- Bell, P. M., and B. T. C. Davis (1969), Melting relation in the system jadeite-diopside at 30 and 40 kilobars, *American Journal of Sciences*, *267A*, 17-32.
- Bell, P. M., and K. Kalb (1969), Stability of omphacite in the absence of excess silica, *Carnegie Inst. Washington, Ann. Rept. Dir. Geophys. Lab., 1967-1968*, 97-98.
- Boland, J. N., and T. E. Tullis (1986), Deformation behavior of wet and dry clinopyroxenite in the brittle to ductile transition region, in *Mineral and Rock Deformation: Laboratory Studies*, edited by B. E. Hobbs and H. C. Heard, American Geophysical Union.
- Brenker, F. E., D. J. Prior, and W. F. Müller (2002), Cation ordering in omphacite and effect on deformation mechanism and lattice preferred orientation (LPO), *Journal of Structural Geology*, *24*, 1991-2005.
- Brenker, F. E., D. J. Prior, and W. F. Müller (2002), Cation ordering in omphacite and the effect on deformation mechanisms and lattice preferred orientation (LPO), *J. Strat. Geol.*, *24*(12), 1991-2005.
- Bromiley, G. D., and H. Keppler (2004), An experimental investigation of hydroxyl solubility in jadeite and Na-rich clinopyroxene, *Contrib. Mineral. Petrol.*, *147*, 189-200.
- Bromiley, G. D., H. Keppler, C. McCammon, F. A. Bromiley, and S. D. Jacobsen (2004), Hydrogen solubility and speciation in natural, gem-quality chromian diopside, *Am. Mineralogist*, *89*, 941-949.
- Bromiley, G. D., H. Keppler, C. McCammon, F. A. Bromiley, and S. D. Jacobsen (2004), Hydrogen solubility and speciation in natural, gem-quality chromian diopside, *American Mineralogist*, *89*, 941-949.

- Buatier, M., H. L. M. van Roermund, M. R. Drury, and J. M. Lardeaux (1991), Deformation and recrystallization mechanisms in naturally deformed omphacites from the Sesia-Lanzo zone; geophysical consequences, *Tectonophysics*, 195, 11-27.
- Bystricky, M., and S. Mackwell (2001), Creep of dry clinopyroxene aggregates, *Journal of Geophysical Research*, 106(B7), 13443-13454.
- Bystricky, M., and S. Mackwell (2001), Creep of dry clinopyroxene aggregates, *Journal of Geophysical Research*, 106, 13443-13454.
- Caceres, C. H., and A. H. Blake (2008), Solute and temperature effects on the strain hardening behaviour of Mg-Zn solid solutions, *Materials Science Forum*, 567-568, 45-50.
- Carpenter, M. (1981), Time-temperature-transformation (TTT) analysis of cation disordering in omphacites., *Contributions to Mineralogy and Petrology*, 78, 433-440.
- Carpenter, M. (1983), Microstructure in sodic pyroxenes, *Periodico di Mineralogia-Roma*, 52, 271-301.
- Carpenter, M. A. (1980), Mechanisms of exsolution in sodic pyroxenes, *Contributions to Mineralogy and Petrology*, 71, 289-300.
- Carswell, D. A. (1990), *Eclogite facies rocks*, 392 pp., Chapman & Hall, New York.
- Champness, P. (1993), Speculation on an order-disorder transformation in omphacite, *American Mineralogist*, 58, 540-542.
- Chen, S., T. Hiraga, and D. L. Kohlstedt (2006), Water weakening of clinopyroxene in the dislocation creep regime, *J. Geophys. Res.*, 111, B08203.
- Chen, S., T. Hiraga, and D. L. Kohlstedt (2006), Water weakening of clinopyroxene in the dislocation creep regime, *Journal of Geophysical Research*, 111, B08203.
- Coleman, R. G., D. E. Lee, L. B. Beatty, and W. W. Brannock (1965), Eclogites and eclogites: their differences and similarities, *Geol. soc. Amer. Bull.*, 76, 483-508.
- Cooper, R. F., and D. L. Kohlstedt (1986), Rheology and structure of olivine-basalt partial melts, *Tectonophysics*, 91, 9315-9323.
- Costa, F., and S. Chakraborty (2008), The effect of water on Si and O diffusion rates in olivine and their relation to transport properties and processes in the upper mantle, *Physics of Earth and Planetary Interiors*, 166, 11-29.
- Dieter, G. E. (1986), *Mechanical Metallurgy*, Mc Graw-Hill.
- Dimanov, A., and J. Ingrin (1995), Premelting and high-temperature diffusion of Ca in synthetic diopside: an increase of the cation mobility, *Physics and Chemistry of Minerals*, 22, 437-508.
- Dimanov, A., O. Jaoul, and V. Sautter (1996), Calcium self-diffusion in natural diopside single crystals, *Geochimica et Cosmochimica Acta*, 60(21), 4095-4106.
- Dimanov, A., M. P. Lavie, G. Dresen, J. Ingrin, and O. Jaoul (2003), Creep of polycrystalline anorthite and diopside, *Journal of Geophysical Research*, 108, B12061.
- Dimanov, A., M. P. Lavie, G. Dresen, J. Ingrin, and O. Jaoul (2003), Creep of polycrystalline anorthite and diopside, *J. Geophys. Res.*, 108, B12061.
- Dimanov, A., and G. Dresen (2005), Rheology of synthetic anorthite-diopside aggregates: implications for ductile shear zones, *Journal of Geophysical Research*, 110.
- Dohmen, R., S. Chakraborty, and H. W. Becker (2002), Si and O diffusion in olivine and implications for characterizing plastic flow in the mantle, *Geophysical Research Letters*, 29(21), 26-21, 26-24.
- Dorner, D. (1999), Experimente zur Synthese von Jadeite, Ruhr-Universität Bochum, Diploma thesis.
- Dorner, D., and B. Stöckhert (2004), Plastic flow strength of jadeite and diopside investigated by microindentation hardness tests, *Tectonophysics*, 379(1-4), 227-238.
- Doukhan, N., J. C. Doukhan, J. Ingrin, O. Jaoul, and P. Raterron (1993), Early partial melting in pyroxenes, *American Mineralogist*, 78, 1246-1256.

- Duffy, T. S., and D. L. Anderson (1989), Seismic velocities in mantle minerals and the mineralogy of the upper mantle, *Journal of Geophysical Research*, *94*, 1895-1912.
- Eskola, P. (1921), On the eclogites of Norway, *Vidensk. Selsk. I. Mat. Naturv. Kl.*, *8*, 1-118.
- Farver, J., and R. Yund (2000), Silicon diffusion in a natural quartz aggregate: constraints on solution-transfer diffusion creep, *Tectonophysics*, *325*, 193-205.
- Farver, J. R. (1989), Oxygen self-diffusion in diopside with application to cooling rate determinations, *Earth Planetary Science Letters*, *92*, 383-396.
- Fleet, M. E., C. T. Herzberg, G. M. Bancroft, and L. P. Aldridge (1978), Omphacite studies, I. The P2/n to C2/c transformation, *American Mineralogist*, *63*, 1100-1106.
- Frost, H. J., and M. F. Ashby (1982), *Deformation-Mechanism Maps*, Pergamon Press.
- Godard, G., and H. L. M. Van Roermund (1995), Deformation-induced clinopyroxene from eclogites, *Journal of structural geology*, *17*, 1425-1443.
- Green, E., T. Holland, and R. Powell (2007), An order-disorder model for omphacitic pyroxenes in the system jadeite-diopside-hedenbergite-acmite, with applications to eclogitic rocks, *American Mineralogist*, *92*, 1181-1189.
- Green, T. H. (1982), Anatexis of mafic crust and high pressure crystallization of andesite, in *In Andesites*, edited by R. S. Thorpe, pp. 465-487, John Wiley, New York.
- Green, T. H., and N. J. Pearson (1986), Ti-rich accessory phase saturation in hydrous mafic-felsic compositions at high P,T, *Chem. Geol.*, *54*, 185-201.
- Green, T. H., Blundy, J. D., Adam, J., Yaxley, G. M. (2000), SIMS determination of trace element partition coefficients between garnet, clinopyroxene and hydrous basaltic liquids at 2-7.5 GPa and 1080-1200°C, *Lithos*, *53*, 165-187.
- Hacker, B. R. (1996), Eclogite formation and the rheology, buoyancy, seismicity, and H₂O content of oceanic crust, in *Subduction top to bottom*, edited by G. E. Bebout, et al., pp. 337-346, Am Geophys Union, Washington, DC.
- Helmstaedt, H., O. L. Anderson, and A. T. Givasci (1972), Petrofabric studies of eclogite, spinel-websterite, and spinel-lherzolite xenoliths from kimberlite-bearing breccia pipe in southeastern Utha and northeastern Arizona, *Journal of Geophysical Research*, *77*, 4350-4365.
- Hier-Majumder, S., S. Mei, and D. L. Kohlstedt (2005), Water weakening of clinopyroxenite in diffusion creep, *Journal of Geophysical Research*, *110*, B07406.
- Hirth, G., and D. L. Kohlstedt (1995), Experimental constraints on the dynamics of the partially molten upper mantle 2. Deformation in the dislocation creep regime, *J. Geophys. Res.*, *100*, 15441-15449.
- Hirth, J. P., and J. Lothe (1982), *Theory of dislocations*, 2 ed., John Wiley & sons, New York.
- Holland, T. J. B., and R. Powell (1998), An internally consistent thermodynamic data set for phases of petrological interest, *Journal of Metamorphic Geology*, *16*, 309-343.
- Humphreys, F. J., P. S. Bate, and P. J. Hurly (2001), Orientation averaging of electron backscattered diffraction data, *J. Microscopy*, *201*, 50-58.
- Ingrin, J., N. Doukhan, and J. C. Doukhan (1991), High-temperature deformation of diopside single crystals. 2, TEM investigation of the induced defect microstructures, *Journal of Geophysical Research*, *96*, 14280-14297.
- Jaoul, O., and P. Raterron (1994), High-temperature deformation of diopside crystal: 3. Influence of pO₂ and SiO₂ precipitation, *Journal of Geophysical Research*, *99*, 9423-9439.
- Jin, Z. M., J. Zhang, H. W. Green II, and S. Jin (2001), Eclogite rheology: implications for subducted lithosphere, *Geology*, *29*(8), 667-670.
- Karato, S., Z. Wang, B. Liu, and K. Fujino (1995), Plastic deformation of garnets: systematics and implications for the rheology of the mantle transition zone, *Earth Planetary Science Letters*, *130*, 13-30.

- Karato, S. I. (1989), Plasticity-crystal structure systematic in dense oxides and its implications for the creep strength of the Earth's deep interior: a preliminary result, *Physics of the Earth and Planetary Interiors*, 55, 234-240.
- Karato, S. I., M. R. Riedel, and D. A. Yuen (2001), Rheological structure and deformation of subducted slabs in the mantle transition zone: implications for mantle circulation and deep earthquakes, *Physics of the Earth and Planetary Interiors* 127, 83–108.
- Kaus, B. J. P., and Y. Y. Podladchikov (2006), Initiation of localized shear zones in viscoelastoplastic rocks, *Journal of Geophysical Research*, 111(B04412).
- Kim, K. T., S. N. Vaidya, and G. C. Kennedy (1972), Effect of pressure on the temperature of the eutectic minimums in two binary systems: NaF-NaCl and CsCl-NaCl, *Journal of Geophysical Research*, 77(35), 6984-6989.
- Kirby, S., R. Engdahl, and R. Denlinger (1996), Intermediate -depth intraslab earthquakes and arc volcanism as physical expressions of crustal and uppermost mantle metamorphism in subducted slabs in *Subduction top to bottom*, edited by G. E. Bebout, et al., Am Geophys Union, Washington, DC.
- Kirby, S. H., and C. B. Raleigh (1973), Mechanisms of High-temperature solid state flow in mineral and ceramics and their bearing on the creep behavior of the mantle., *Tectonophysics*.
- Kirby, S. H., and J. M. Christie (1977), Mechanical twinning in diopside $\text{Ca}(\text{Mg,Fe})\text{Si}_2\text{O}_6$: Structural mechanism associated crystal defects, *Physics Chemistry and Mineralogy*, 1, 137-163.
- Kirby, S. H., and J. M. Christie (1977), Mechanical Twinning in Diopside $\text{Ca}(\text{Mg,Fe})\text{Si}_2\text{O}_6$: Structural mechanism associated crystal defects, *Phys. Chem. Mineral*, 1, 137-163.
- Kirby, S. H., and A. K. Kronenberg (1984), Deformation of clinopyroxenite: evidence for a transition in flow mechanisms and semibrittle behaviour, *Journal of Geophysical Research*, 89(B5), 3177-3192.
- Kirby, S. H., and A. K. Kronenberg (1984), Deformation of clinopyroxenite: evidence for a transition in flow mechanisms and semibrittle behaviour, *J. Geophys. Res*, 89(B5), 3177-3192.
- Klemme, S., J. D. BLUNDY, and B. J. WOOD (2002), Experimental constraints on major and trace element partitioning during partial melting of eclogite, *Geochimica et Cosmochimica Acta*, 66(17), 3109-3123.
- Kohlstedt, D. L., B. Evans, and S. J. Mackwell (1995), Strength of the lithosphere. Constraints imposed by laboratory experiments, *Journal of Geophysical Research* 100, 17587–17602.
- Kohlstedt, D. L. (2006), The role of water in high-temperature rock deformation, *Review in Mineralogy and Geochemistry*, 62, 377-396.
- Kolle, J., and J. Blacic (1982), Deformation of single-crystal clinopyroxenes: 1 Mechanical twinning in diopside and hedenbergite, *J Geophys Res*, 87, 4019-4034.
- Kronenberg, A. K., and G. H. Wolf (1990), Fourier transform infrared spectroscopy determinations of intragranular water content in quartz-bearing rocks: implications for hydrolytic weakening in the laboratory and within the earth, *Tectonophysics* 172, 255–271.
- Küster, M., and B. Stöckhert (1999), High differential stress and sublithostatic pore fluid pressure in the ductile regime-microstructural evidence for short-term post-seismic creep in the Sesia Zone, Western Alps, *Tectonophysics*, 303, 263–277.
- Li, L., D. Weidner, P. Raterron, J. Chen, M. Vaughan, S. Mei, and B. Durham (2006), Deformation of olivine at mantle pressure using the D-DIA, *European Journal of Mineralogy*, 18, 7-19.
- Majumder, S. H., S. Mei, and D. L. Kohlstedt (2005), Water weakening of clinopyroxenite in diffusion creep, *Journal of Geophysical Research*, 110(B07406).
- Milke, R., and W. Heinrich (2002), Diffusion-controlled growth of wollastonite rims between quartz and calcite: comparison between nature and experiment *Journal of Metamorphic Geology*, 20, 467–480.

- Müller, W. F., and G. Franz (2008), TEM-microstructures in omphacite and other minerals from eclogite near to a thrust zone; the eclogite zone - Venediger nappe area, Tauern Window, Austria, *Neues Jahrbuch für Mineralogie - Abhandlungen*, 184(3), 285-298.
- Orzol, J. (2002), Experimental deformation of jadeite, , doctoral dissertation thesis, 153 pp, Ruhr-University Bochum, Bochum.
- Orzol, J., B. Stöckhert, C. A. Treppmann, and F. Rummel (2006), Experimental deformation of synthetic wet jadeite aggregates, *Journal of Geophysical Research*, 111(B06205).
- Pacaud, L., J. Ingrin, and O. Jaoul (1999), High-temperature diffusion of oxygen in synthetic diopside measured by nuclear reaction analysis, *Mineralogical Magazine*, 63(5), 673-686.
- Paterson, M. S. (1982), The determination of hydroxyl by infrared absorption in quartz, silicate glasses and similar materials, *Bulletin of Mineralogy*, 105, 20-29.
- Pati, J. K., M. Arima, and A. K. Gupta (2000), Experimental study of the system diopside-albite-nepheline at $P(H_2O) = P(total) = 2$ and 10 Kbar and at $P(total) = 28$ Kbar, *Thw canadian mineralogist*, 38, 1177-1191.
- Philippot, P., L. M. van Roermund, and D. Mainprice (1992), Deformation processes in eclogitic rocks: evidence for the rheological delamination of the oceanic crust in deeper levels of subduction zones, *Journal of Structural Geology*, 14, 1059-1077.
- Piepenbreier, D., and B. Stöckhert (2001), Plastic flow of omphacite in eclogites at temperature below 500°C - implications for interplate coupling in subduction zones, *International Journal of Earth Sciences*, 90, 197-210.
- Poirier, J. P. (1985), *Creep of Crystals*, 260 pp., Cambridge Univ. Press, New York.
- Prior, J. P., A. P. Bolyle, F. Brenker, M. C. Cheadle, A. Day, G. Lopez, L. Peruzzo, G. J. Potts, S. Reddy, R. Spiess, N. E. Timms, P. Trimby, J. Wheeler, and L. Zetterstrom (1999), The application of electron backscatter diffraction and orientation contrast imaging in the SEM to textural problems in rocks, *American Mineralogy*, 84, 1741-1759.
- Raheim, A., and D. H. Green (1975), P,T paths of natural eclogites during metamorphism-a record of subduction, *Lithos*, 8, 317-328.
- Ranalli, G. (1995), *Rheology of the Earth*, 2 ed., Chapman and Hall.
- Rapp, R. P., N. Shimizu, M. D. Norman, and G. S. Applegate (1999), Reaction between slab-derived melts and peridotite in the mantle wedge: Experimental constraints at 3.8 GPa, *Chem. Geol.*, 160, 335-356.
- Raterron, P., and O. Jaoul (1991), High-temperature deformation of diopside single crystal; 1) Mechanical data, *Journal of Geophysical Research*, 96, 14277-14286.
- Raterron, P., and O. Jaoul (1991), High-temperature deformation of diopside single crystal; 1, Mechanical data, *Journal of Geophysical Research*, 96, 14277-14286.
- Raterron, P., N. Doukhan, O. Jaoul, and J. C. Doukhan (1994), High temperature deformation of diopside IV: Predominance of {110} glide above 1000°C, *Physics of the Earth and Planetary Interiors*, 82, 209-222.
- Reed-Hill, R. E., and R. Abbaschian (1994), *Physical Metallurgy Principles*, PWS publishing company, Boston.
- Renner, J., A. Zerbian, and B. Stöckhert (1997), Microstructures of synthetic polycrystalline coesite aggregates: The effect of pressure, temperature, and time, *Lithos*, 41, 169-184.
- Renner, J., B. Stöckhert, A. Zerbian, K. Röller, and F. Rummel (2001), An experimental study into the rheology of synthetic polycrystalline coesite aggregates, *J. Geophys. Res.*, 106, 19,411-419,429.
- Rutter, E. H. (1993), Experimental rock deformation: techniques, results and application to tectonics, *Geology Today*, 9(2), 61-65.
- Rybacki, E., J. Renner, K. Konrad, W. Harbott, F. Rummel, and B. Stöckhert (1998), A servohydraulically-controlled deformation apparatus for rock deformation under conditions of ultra-high pressure metamorphism, *Pure Appl. Geophys.*, 152, 579-606.

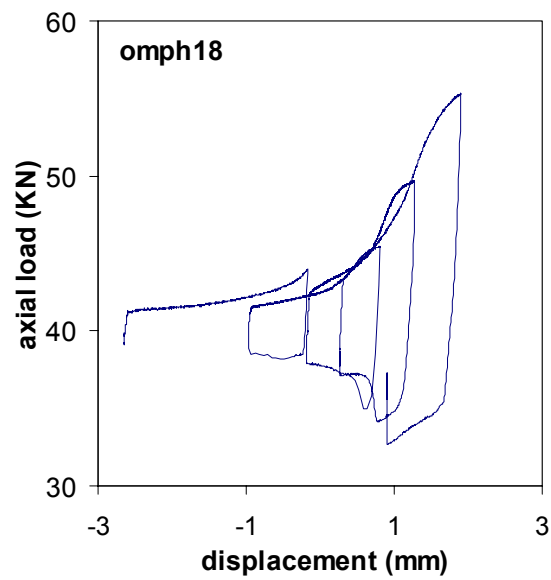
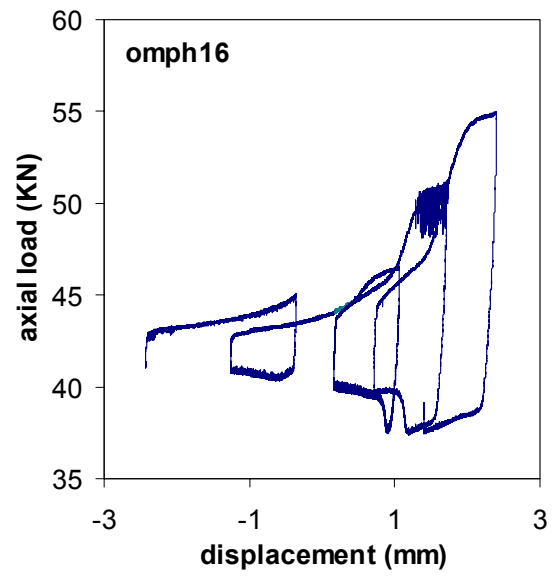
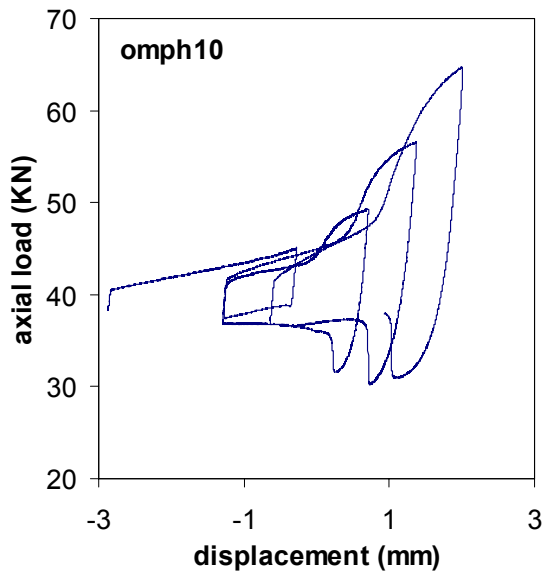
- Rybacki, E., and G. Dresen (2000), Dislocation and diffusion creep of synthetic anorthite aggregates, *J. Geophys. Res.*, *105*(11), 26017–26036.
- Ryerson, F. J., and E. B. Watson (1987), Rutile saturation in magmas: Implications for Ti-Nb-Ta depletion in island-arc basalts, *Earth Planet. Sci. Lett.*, *86*, 225-239.
- Ryerson, F. J., and K. D. McKeegan (1994), Determination of oxygen self-diffusion in akermanite, anorthite, diopside and spinel: Implications for oxygen isotopic anomalies and the thermal histories of Ca-Al-rich inclusions, *Geochimica et Cosmochimica Acta*, *58*, 3713-3734.
- Sherby, O. D., and P. M. Burke (1968), Mechanical behavior of crystalline solids at elevated temperature, *Prog. Mater. Sci.*, *13*, 325-429.
- Smith, D. C., and A. Etal (1982), Eclogites and their problems: an introduction to the first international Eclogite Conference, *Terra Cognita*, *2*, 283-295.
- Smulikowski, K. (1968), Differentiation of eclogites and its possible causes, *Lithos*, *1*, 89-101.
- Sotin, C., and J. P. Poirier (1984), Analysis of high-temperature creep experiments by generalized nonlinear inversion, *Mechanics of Materials*, *3*, 311-317.
- Stöckhert, B., and J. Renner (1998), Rheology of crustal rocks at ultrahigh pressure, in *When continents collide: Geodynamics and geochemistry of ultrahigh pressure rocks*, edited by B. R. Hacker and J. G. Liou, pp. 57-95, Kluwer, Dordrecht.
- Stöckhert, B. (2002), Stress and deformation in subduction zones: insight from the record of exhumed metamorphic rocks, *Geological Society, Special Publications*, *200*, 255-274.
- Takeuchi, S., and A. S. Argon (1976), Steady-state creep of single-phase crystalline matter at high temperature, *Journal of Materials Science*, *11*, 1542-1566.
- Taylor, G. I. (1934), The mechanisms of plastic deformation in crystals, *Proc. Roy. Soc.*, *A145*, 362–387.
- Tingle, T. N., H. W. Green, T. E. Young, and T. A. Koczynski (1993), Improvements to Griggs-type apparatus for mechanical testing at high pressures and temperatures, *Pure and appl. geophys.*, *141*, 523-543.
- Treppmann, C. A., and B. Stöckhert (2003), Quartz microstructures developed during non-steady state plastic flow at rapidly decaying stress and strain rate, *Journal of Structural Geology* *25*, 2035–2051.
- Ulrich, S., and D. Mainprice (2005), Does cation ordering in omphacite influence development of lattice-preferred orientation?, *J. Struct. Geol.*, *27*, 419-431.
- Ulrich, S., and D. Mainprice (2005), Does cation ordering in omphacite influence development of lattice-preferred orientation?, *Journal of Structural Geology*, *27*, 419-431.
- van der Klauw, S. N. G. C., T. Reinecke, and B. Stöckhert (1997), Exhumation of ultrahigh-pressure metamorphic oceanic crust from Lago di Cignana, Piemontese zone, western Alps: the structural record in metabasites, *Lithos* *41*, 79-102.
- Van Roermund, H. L. M., and J. N. Boland (1981), The dislocation substructures of naturally deformed omphacites, *Tectonophysics*, *78*, 403-418.
- Weertman, J. (1957), Steady-State Creep of Crystal, *journal of applied physics*, *28*(10), 1185-1189.
- Weertman, J. (1963), An Experimental relation defining the stress dependence of minimum creep rate in metals, *Trans. AIME*, *227*, 1475-1476.
- Weertman, J. (1968), Dislocation climb theory of steady-state creep, *Transaction of the ASM*, *61*, 681-694.
- Weertman, J. (1999), *Microstructural mechanisms in creep*, in *Mechanics and Materials: Fundamentals and Linkages*, pp.451-488, John Wiley, New York.
- Wood, B. J., and J. D. Blundy (1997), A predictive model for rare earth element partitioning between clinopyroxene and anhydrous silicate melt, *Contrib. Mineral. Petrol.*, *129*, 166–181.
- Yaxley, G. M., and D. H. Green (1998), Reactions between eclogite and peridotite: Mantle refertilisation by subduction of oceanic crust, *Schweiz. Mineral. Petrol. Mitteil.*, *78*, 143–255.

Zhang, J., H. W. Green II, and K. N. Bozhilov (2006), Rheology of omphacite at high temperature and pressure and significance of its lattice preferred orientations, *Earth and Planetary Science Letters*, 246(3-4), 432-443.

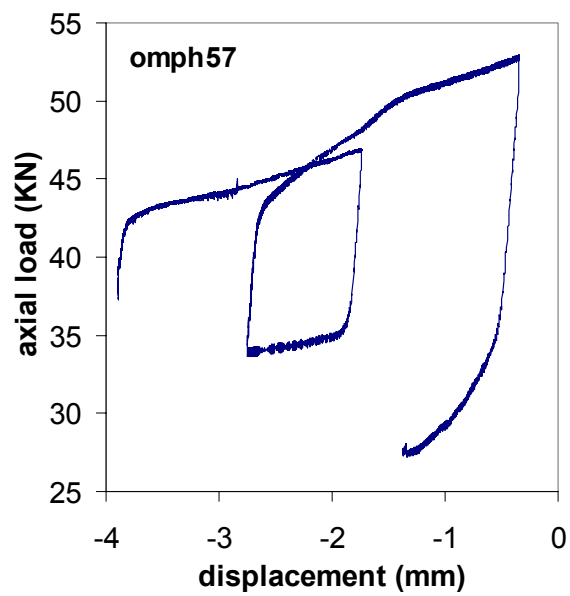
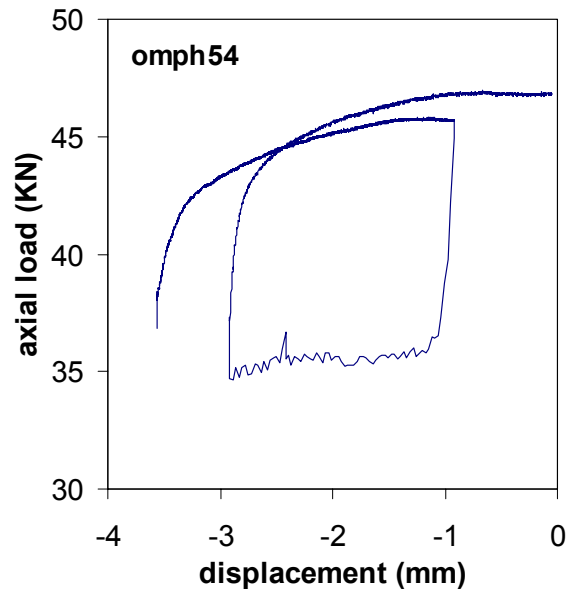
Zhao, Y. H., M. E. Zimmerman, and D. L. Kohlstedt (2007), Influence of Fe content on the creep properties of olivine, *Lunar and Planetary Science XXXVIII*.

Appendix A

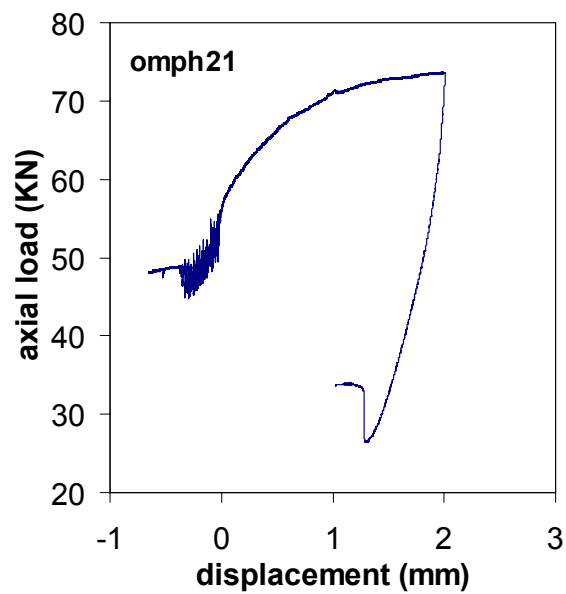
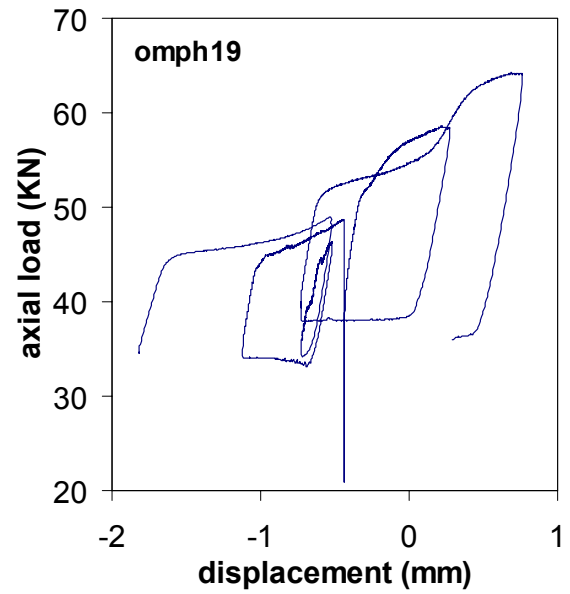
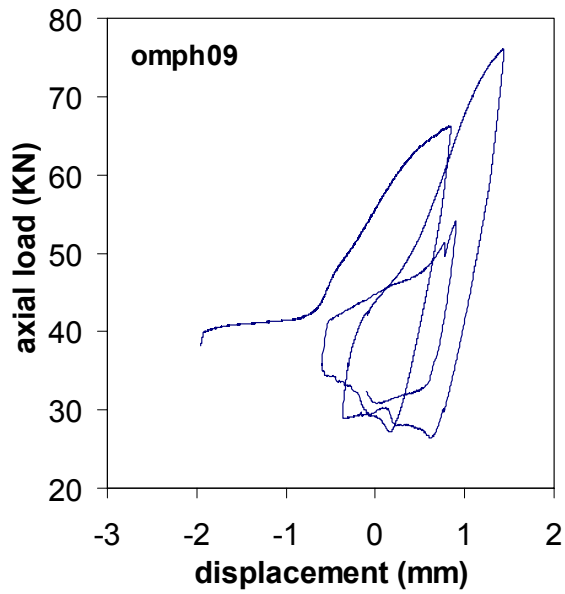
The axial load-displacement curves for deformation experiments on synthetic omphacite aggregates (see table 5 for conditions of experiments)



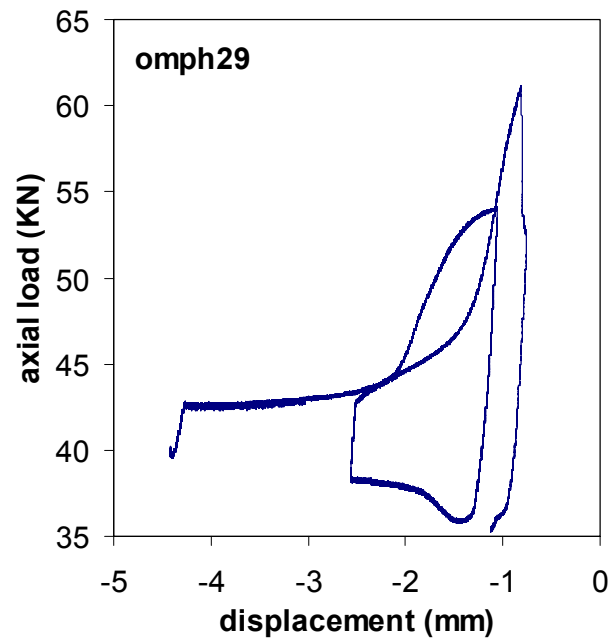
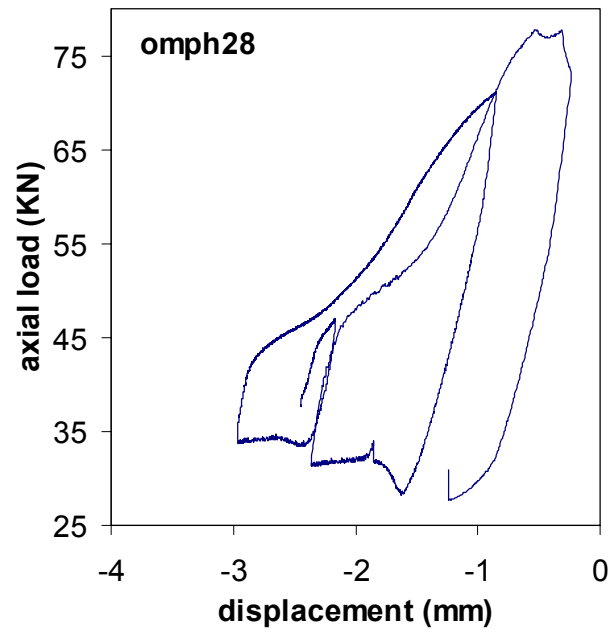
Appendix A (continue)
(see table 5 for conditions of experiments)



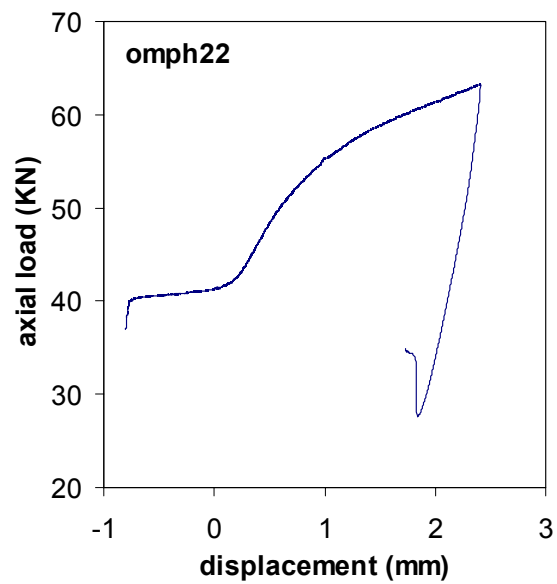
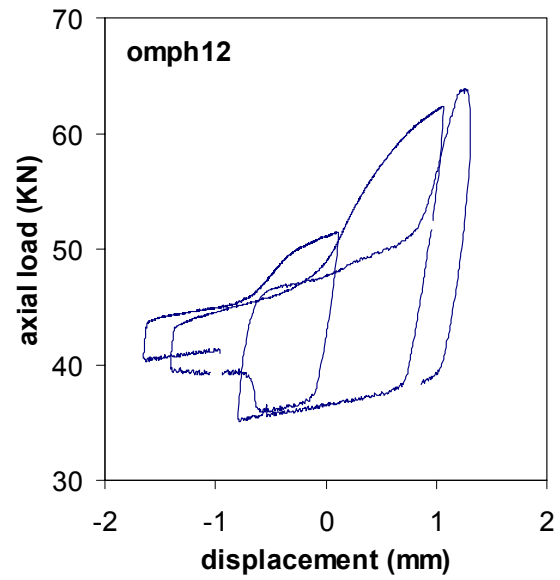
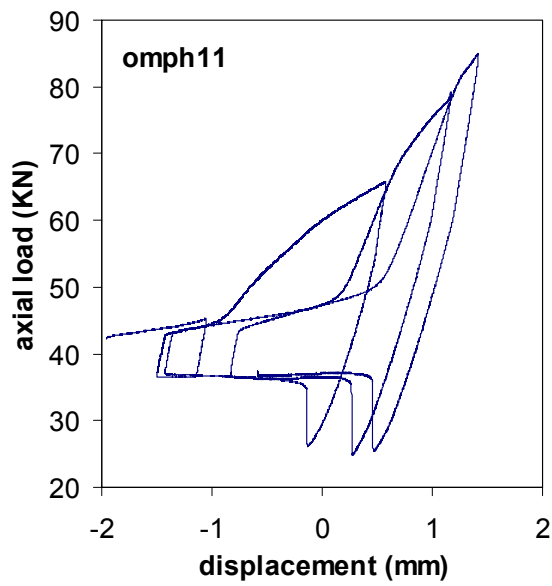
Appendix A (continue)
(see table 5 for conditions of experiments)



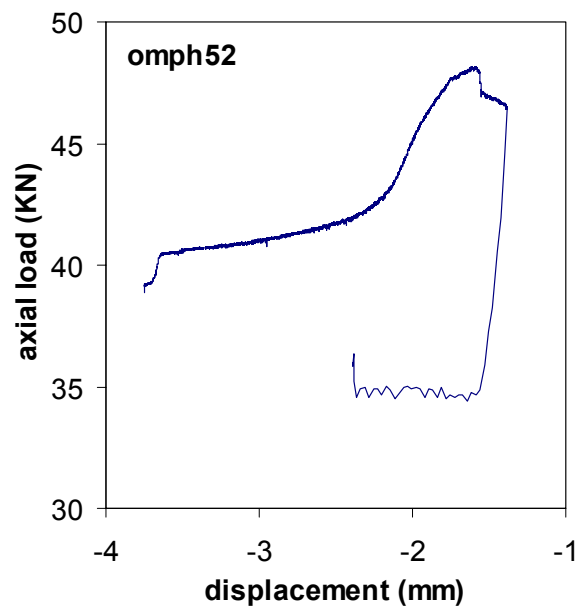
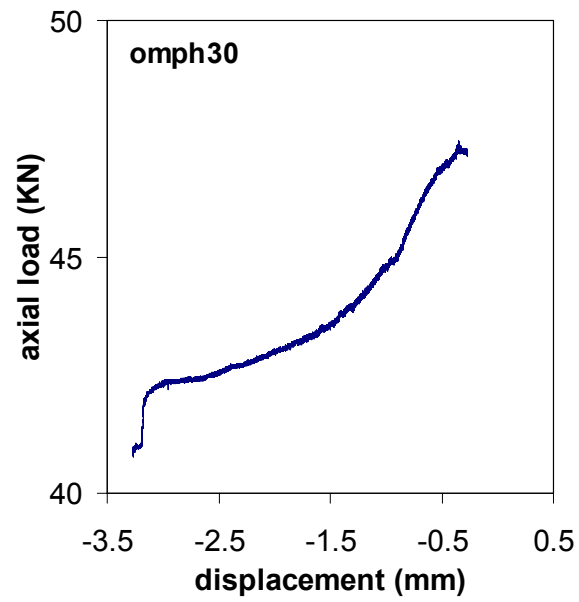
Appendix A (continue)
(see table 5 for conditions of experiments)



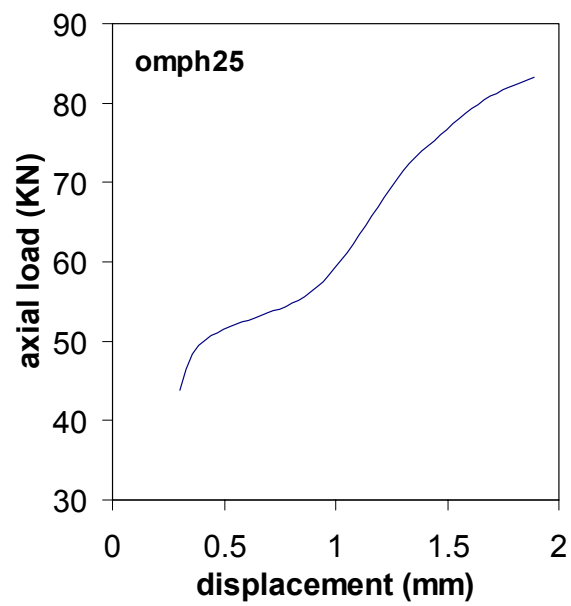
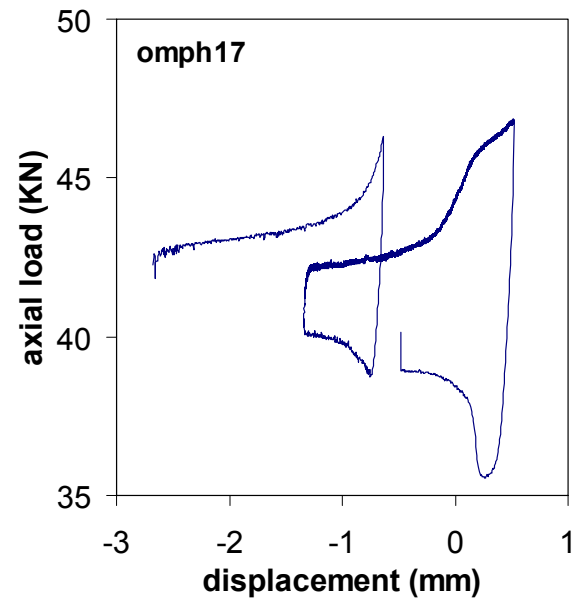
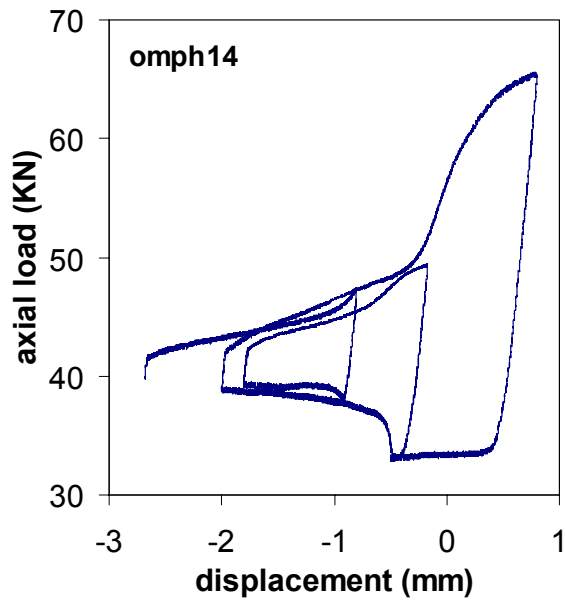
Appendix A (continue)
(see table 5 for conditions of experiments)



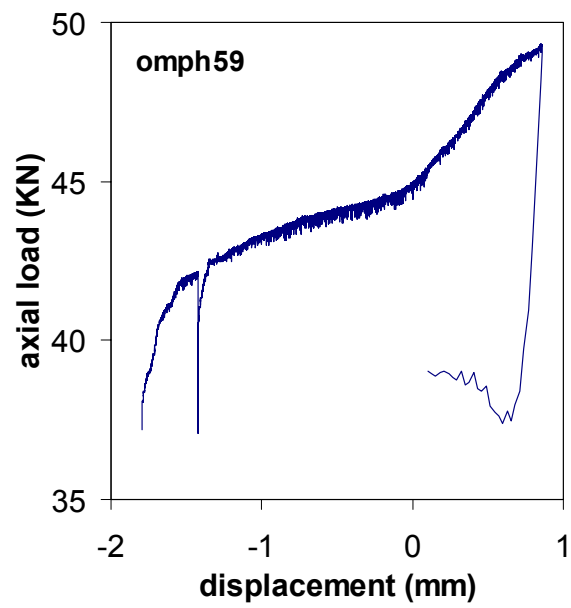
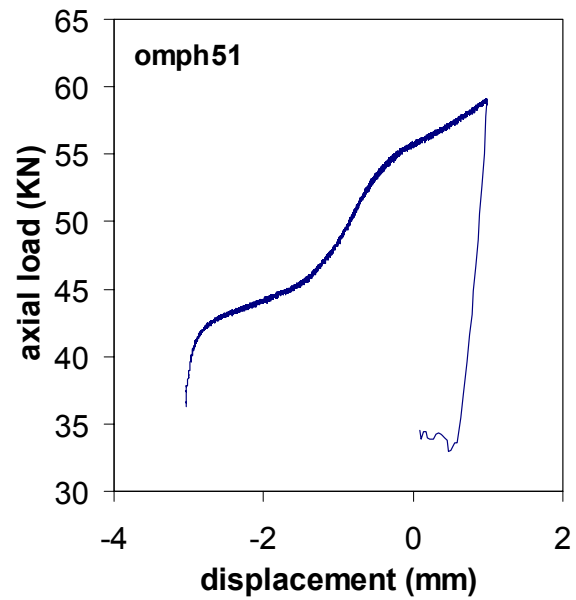
Appendix A (continue)
(see table 5 for conditions of experiments)



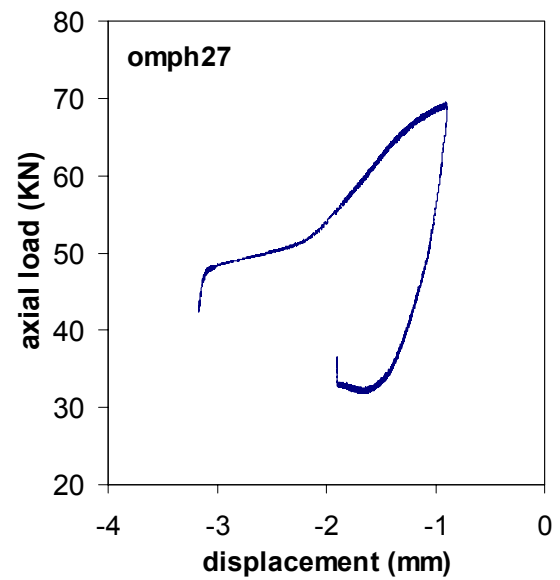
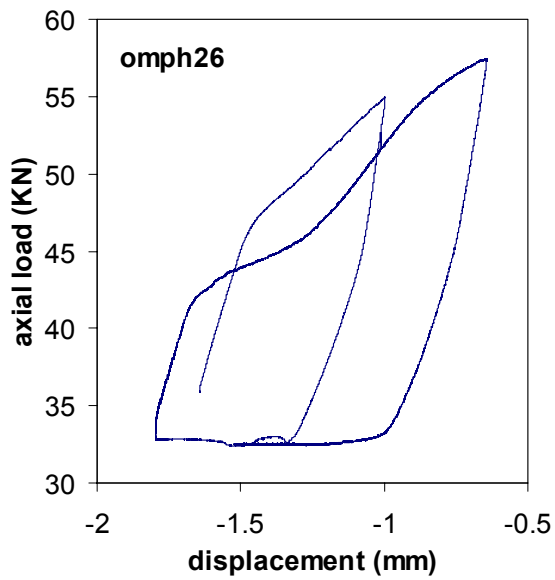
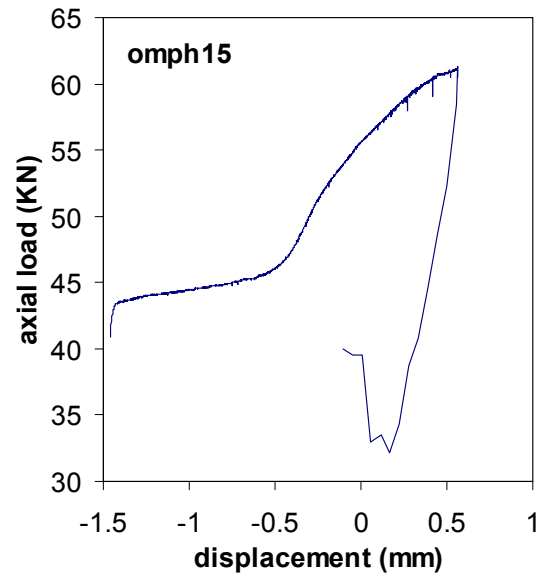
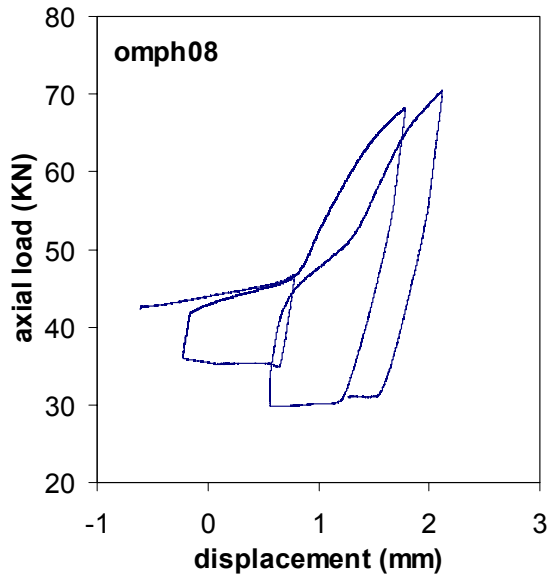
Appendix A (continue)
(see table 5 for conditions of experiments)



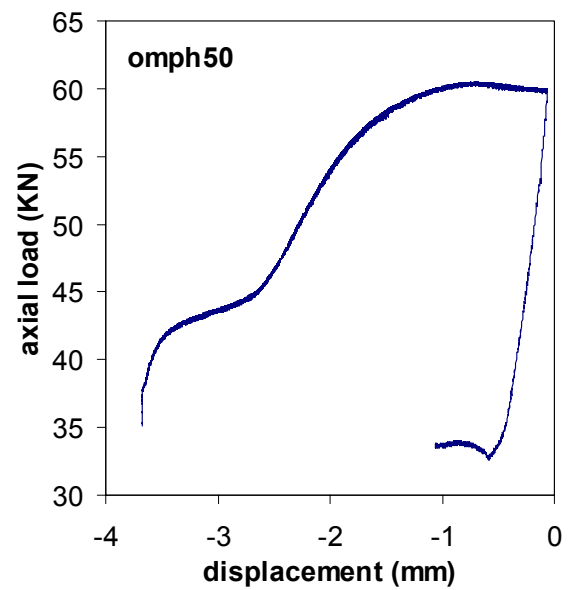
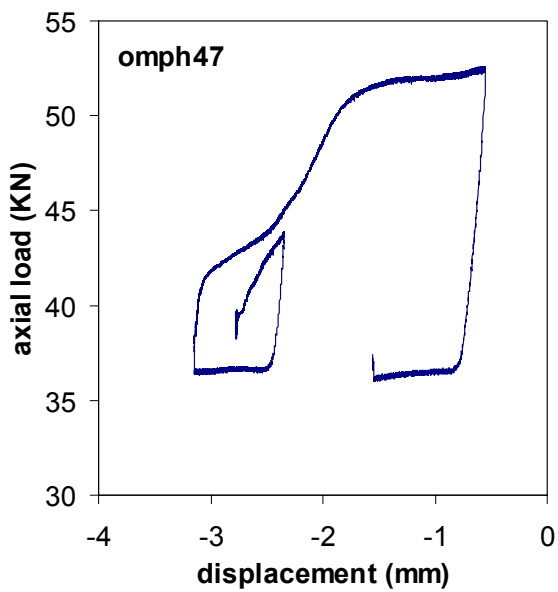
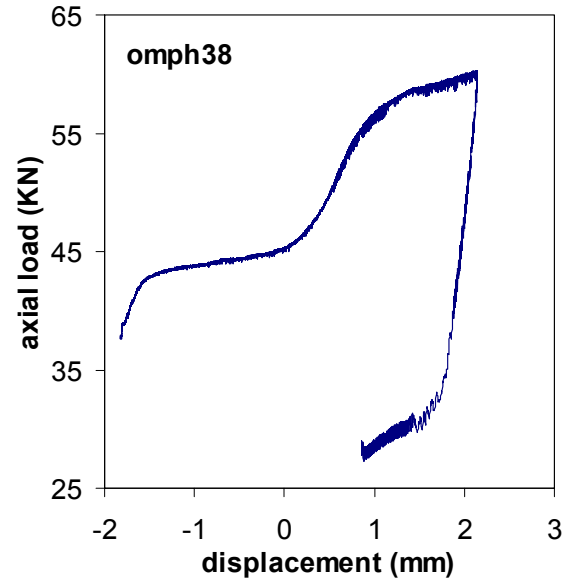
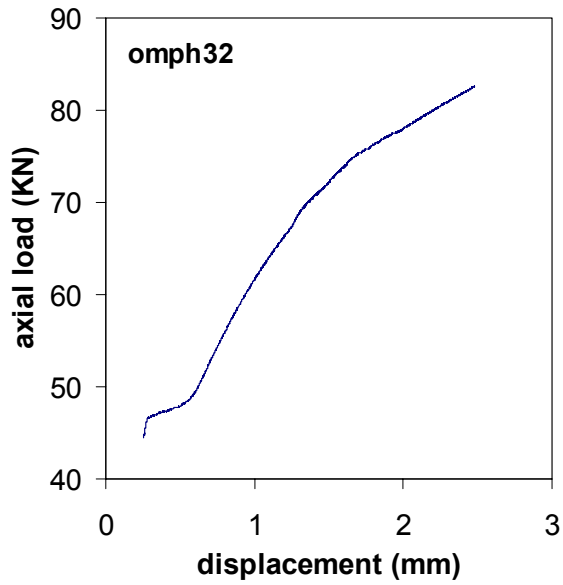
Appendix A (continue)
(see table 5 for conditions of experiments)



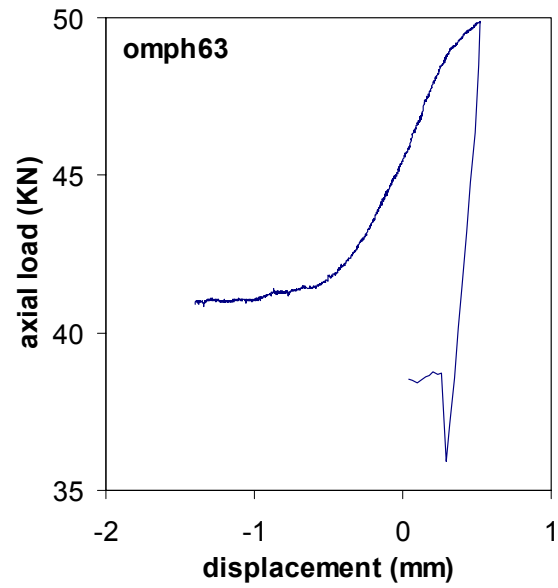
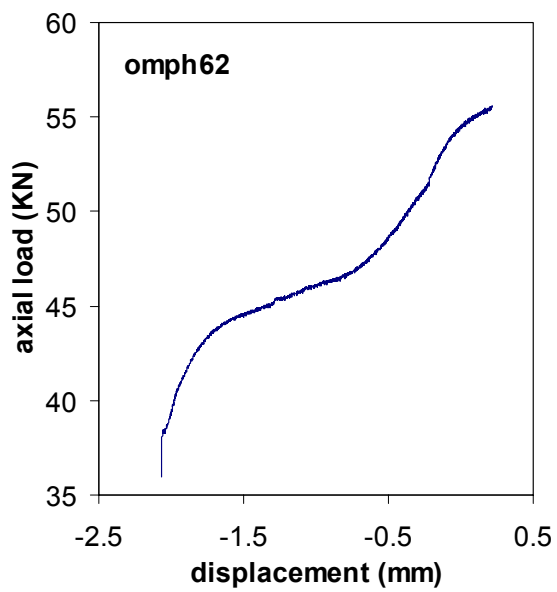
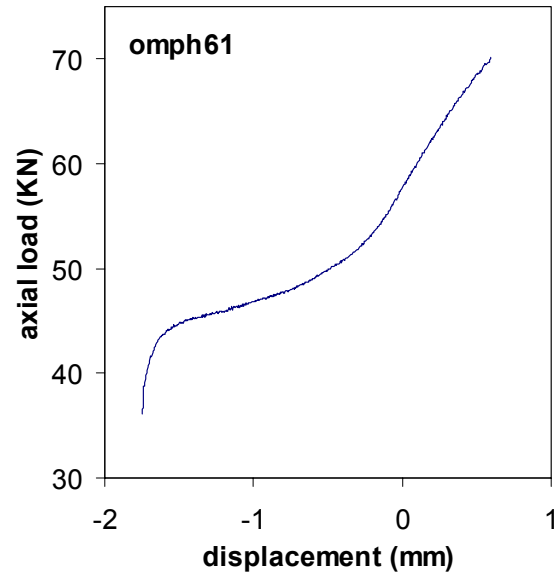
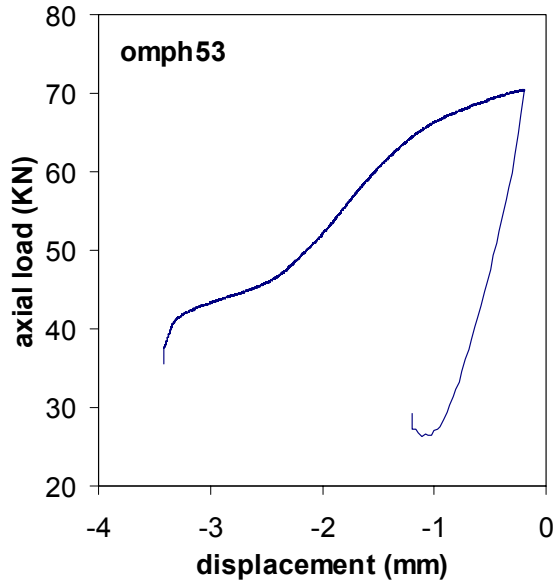
Appendix A (continue)
(see table 5 for conditions of experiments)



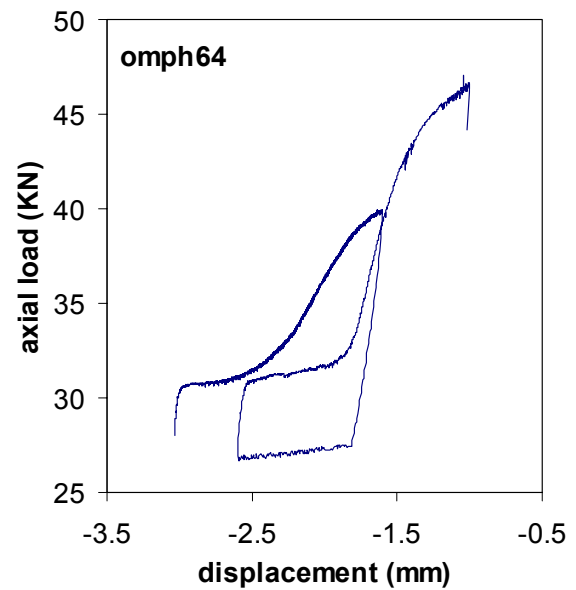
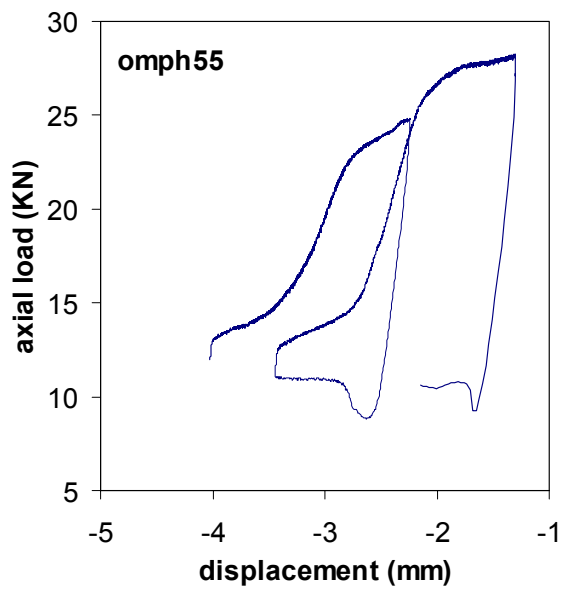
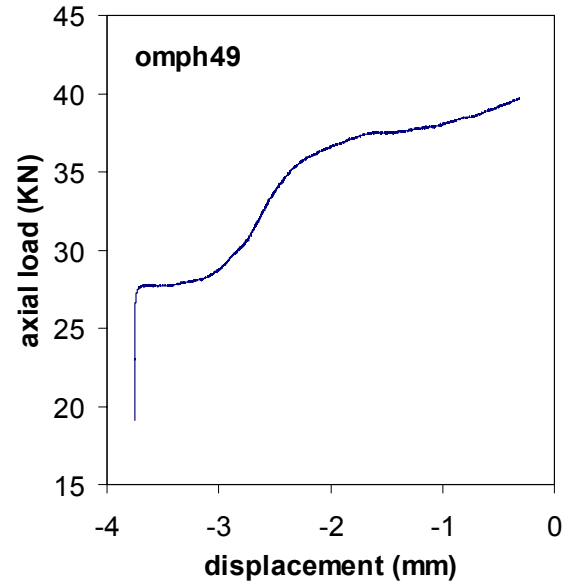
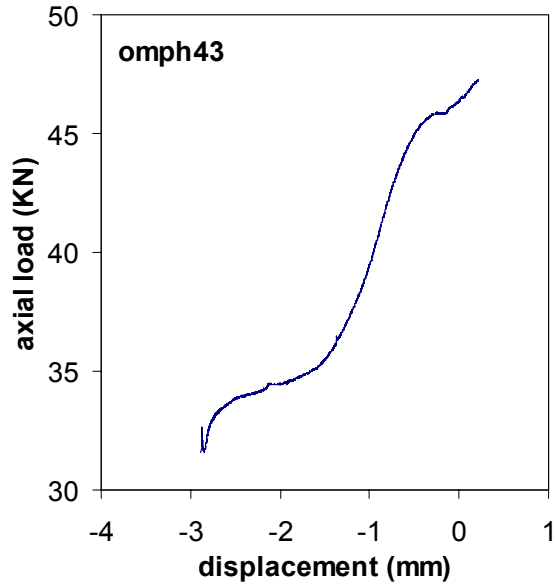
Appendix A (continue)
(see table 5 for conditions of experiments)



Appendix A (continue)
(see table 5 for conditions of experiments)

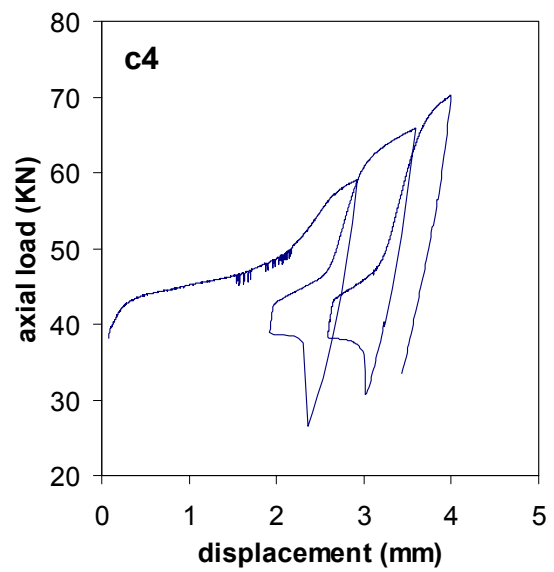
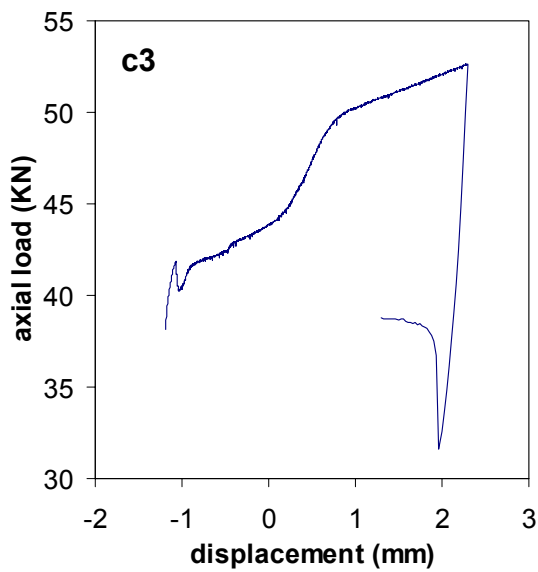
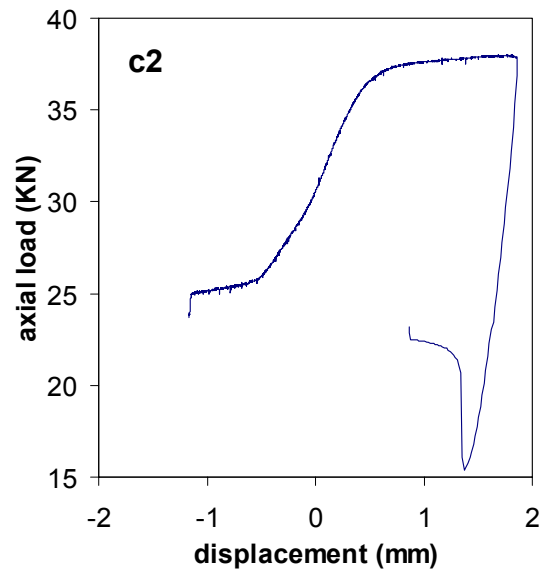
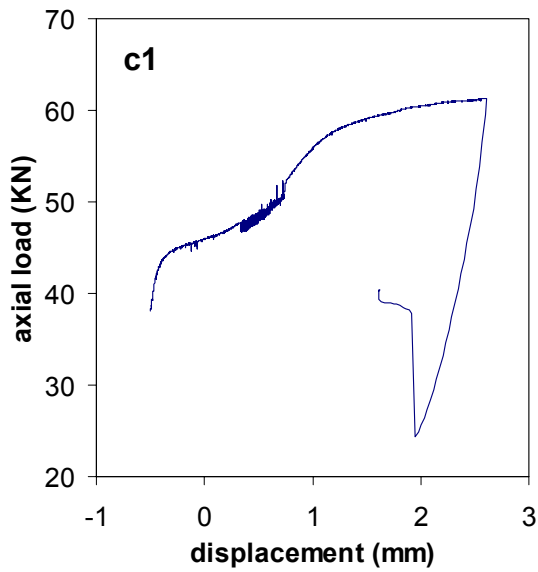


Appendix A (continue)
(see table 6 for conditions of experiments)

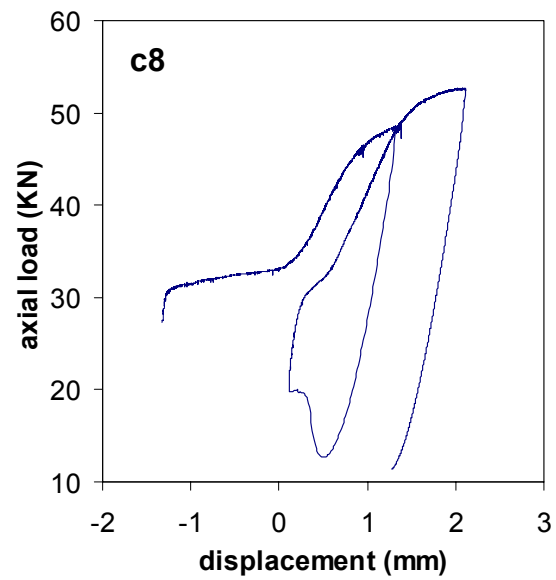
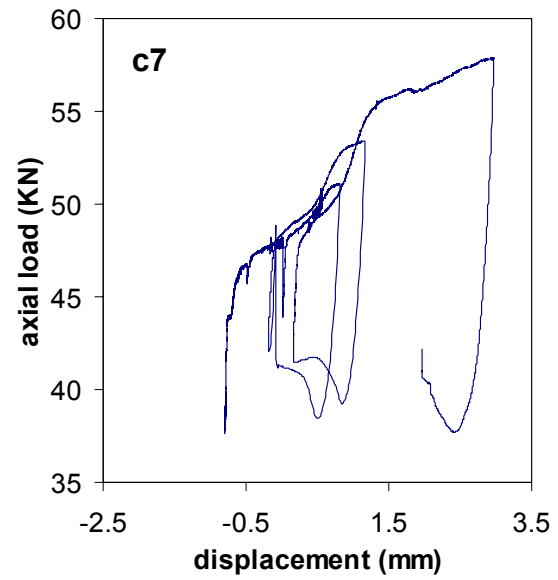
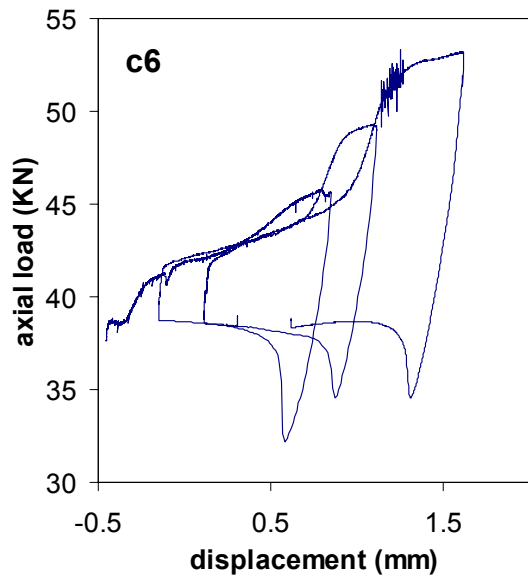


Appendix B

The axial load-displacement curves for deformation experiments on natural Sleaford Bay clinopyroxenite samples (see table 8 for conditions of experiments)



Appendix B (continue)
(see table 8 for conditions of experiments)



Zusammenfassung

Im Stabilitätsfeld von Jadeit wurden entlang der Mischkristallreihe Diopsid-Jadeit synthetische Omphazit-Aggregate mit fünf verschiedenen Zusammensetzungen aus Glaspuder kristallisiert. In einer Feststoffapparatur wurden an diesen Proben triaxiale Druckversuche bei einem Manteldruck von 2.5 GPa, Temperaturen von 900 bis 1100°C und Verformungsraten zwischen $1.1 \times 10^{-6} \text{ s}^{-1}$ und $8.5 \times 10^{-5} \text{ s}^{-1}$ durchgeführt. Anhand von vier Experimenten an Diopsid-Aggregaten bei Umgebungsdrücken $< 2.5 \text{ GPa}$ wurde darüber hinaus der Einfluss des Manteldrucks auf den Deformationsmechanismus untersucht. Durch weitere sieben Experimente an Fe-haltigen Sleaford Bay Klinopyroxenen bei Umgebungsdrücken zwischen 1.5 und 2.7 GPa, deren Ergebnisse einen Vergleich mit bereits veröffentlichten Daten ermöglichten, wurde der Einfluss Fe-Gehalts auf die Festigkeit der Proben ermittelt.

Der Wassergehalt der synthetischen Proben nimmt systematisch mit steigendem Jadeit-Anteil zu. Die Festigkeit der synthetischen Omphazit-Aggregate nimmt mit zunehmender Temperatur und geringer werdender Verformungsrate ab. Bei den realisierten experimentellen Bedingungen ist Jadeit das schwächere Endglied. Bei 900 und 1000°C sind mittlere Zusammensetzungen fester als beide Endglieder. Proben mit diopsidischen Zusammensetzungen, die bei hohen Effektivdrücken verformt werden, zeigen eine Vielzahl mechanischer (100)[001] Zwillinge, wohingegen Proben mit jadeitischen Zusammensetzungen, die bei geringen Effektivspannungen verformt werden, ausgeprägte Subkorn Grenzen und lokale Rekristallisation aufweisen. In den deformierten Proben wird eine schwach ausgeprägte kristallographisch bevorzugte Orientierung beobachtet. Die gewonnenen mechanischen Daten und die beobachtete Mikrostruktur der synthetisierten Proben weisen darauf hin, dass die Endglieder der Diopsid-Jadeit-Mischkristallreihe durch unterschiedliche Deformationsmechanismen verformt werden. Bei den untersuchten Bedingungen wird die Verformung von Diopsid-Aggregaten durch Versetzungsgleiten, die von Jadeit-Aggregaten dagegen durch Versetzungsklettern kontrolliert. Die Mikromechanische Modellierung führt zu physikalisch plausiblen Fließgesetz-Parametern. Die Abhängigkeit der Festigkeit von der Zusammensetzung folgt der Abhängigkeit der Schmelztemperatur und des Schermoduls von der Zusammensetzung. Die Festigkeit der natürlichen Klinopyroxene entspricht in etwa der Festigkeit synthetischer Diopsid-Aggregate bei geringen Temperaturen.

Die Unabhängigkeit des Deformationsverhaltens von Pyroxenit-Aggregaten vom Fe- und H-Gehalt steht im Einklang mit den genannten Schlussfolgerungen, da Deformationen, die durch Versetzungsgleiten kontrolliert werden, von der Konzentration von Fremdatomen, die wiederum die Diffusionskinetik beeinflussen, unabhängig sein sollten. Da sich die Wasserdampf-Fugazität und Hydroxyl-Löslichkeit mit dem Manteldruck ändern, müssen die Einflüsse von Druck und Wasserstoff in den Deformationsexperimenten gemeinsam betrachtet werden. Der Vergleich der mechanischen Ergebnisse für natürliche Klinopyroxene und synthetische Diopside zeigt eine Erhöhung der Festigkeit mit zunehmendem Druck und ein positives Aktivierungsvolumen bei 900°C, wohingegen oberhalb 1000°C scheinbar ein Festigkeitsabfall mit zunehmendem Druck zu verzeichnen ist. Eine Extrapolation des eingeschränkten Fließgesetzes zu geologischen Verformungsraten deutet eine erhebliche Festigkeit für Omphazit-Aggregate bei Temperaturen bis 1000°C an. Eine lang anhaltende durchgreifende Deformation von Eklogiten in Subduktionszonen durch Versetzungskriechen scheint daher unwahrscheinlich. Exhumierte Eklogite mit Omphazit-Mikrostrukturen, die auf Kristallplastische Deformation schließen lassen, haben vermutlich eine Periode hoher Belastung verbunden mit einem seismischen Ereignis erfahren.

Curriculum Vitae

Rasoul Hamidzadeh Moghadam

01 April 1967, Iran

Querenburger Höhe 293, 44801 Bochum, Germany

Tel: 0234-7090287

E-mail: rasoul.moghadam@rub.de

August 1985-September 1989: B.Sc., Mining department (exploration group), Isfahan University of Technology, Isfahan, Iran.

January 1990-Mai 1994: M.Sc., Mining department (exploration group), Amirkabir University of Technology, Tehran, Iran; Thesis on the application of RS-IP geoelectrical method for exploration of lead-zinc sulfide deposits.

August 1994-March 2004: Fieldwork and theory courses teaching for B.Sc. students, Sahand University of Technology, Tabriz, Iran.

April 2004-October 2004: Research position; Writing code with Q-Basic for mapping of geoelectrical data (not published), Delft University of Technology, The Netherlands.

February 2004-present: PhD student; Thesis on mechanical behavior of synthetic omphacite aggregates at high temperature and high pressure; Ruhr-Universität Bochum, Germany.

Acknowledgements

I wish to express my warmest thanks to my supervisor professor Dr. Jörg Renner, who has supported me in this project from its beginning to its completion.

I would like to express my thanks to professor Dr. Bernhard Stöckhert and junior professor Dr. Claudia Trepmann: professor Dr. Bernhard Stöckhert for his very useful discussions about application of experimental results and junior professor Dr. Claudia Trepmann for EBSD and TEM analysis and useful advises.

I thank Dr. Rolf Neuser for SEM, Dr. Thomas Fockenber for XRD, Dr. Klaus Röller for FTIR and Dr. Jürgen Bernhardt for EMP analyses and Dr. Jan H. ter Heege for laboratory comments.

I also thank Frank Bettenstedt for apparatus maintenance and welding of the capsules, Ralf Bleiweiß for machining of parts for the sample assemblies.

This work was carried out within the SFB 526, "Rheology of the Earth-from the upper crust into the subduction zone".